

POLITECNICO DI TORINO



Master of Science in Communications
and Computer Networks Engineering

TOWARD 25 AND 50 GBPS NEXT-GENERATION PASSIVE OPTICAL ACCESS NETWORKS

MSc Thesis

Valerio Milite

Supervisors:

Prof. Roberto Gaudino

Prof. Valter Ferrero

Academic Year 2017/2018

To my parents, my brother
and those who were with me
during this journey.

TABLE OF CONTENTS

Table of Contents	iii
Acknowledgments	v
List of acronyms.....	vi
Abstract.....	1
Chapter 1: Motivations and background.....	6
1.1 PONs Today	6
1.2 The need for High-Speed Passive Optical Networks (HS-PONs).....	7
1.2.1 Example: the fronthaul in the C-RAN architecture	8
1.3 HS-PON requirements	10
1.4 Which modulation formats	10
1.4.1 Duobinary signaling.....	11
1.4.2 Electrical Duobinary	13
1.4.3 Optical Duobinary.....	14
1.5 Conclusions	15
Chapter 2: The bandwidth-dependent penalty.....	16
2.1 The starting point for this activity.....	16
2.2 The simulation setup	17
2.2.1 Alternative receiver models.....	19
2.3 Three sets of simulation parameters.....	21
2.4 “Filter-after-noises” receiver results	23
2.4.1 Penalty of using realistic parameters	24
2.4.2 The bandwidth-dependent penalty.....	25
2.4.2.1 PAM-2 results for bandwidth-limited cases	26
2.4.2.2 PAM-4 results for bandwidth-limited cases	27
2.4.2.3 EDB results for bandwidth-limited cases	29
2.5 Results with alternative receiver models	30
2.5.1 Penalty of using realistic parameters	31
2.5.2 The bandwidth-dependent penalty.....	32
2.6 Conclusions	34
Chapter 3: Direct modulation in HS-PONs	35
3.1 The use of a directly modulated laser (DML).....	35
3.2 The frequency chirp: a theoretical background.....	36
3.3 The separated effect of transient chirp	37
3.3.1 Interplay between transient chirp and dispersion.....	37
3.3.2 Transient chirp model validation	40
3.3.3 DML and transient chirp: effect on different formats.....	45
3.4 The separated effect of adiabatic chirp	49
3.4.1 Interplay between adiabatic chirp and dispersion.....	49
3.4.2 Chirp/dispersion effect on eye diagram: simulation setup	50
3.4.2.1 Back-to-back case	52
3.4.2.2 Dispersion without chirp case.....	52
3.4.2.3 Negative dispersion case	53

3.4.2.4 Positive dispersion case	54
3.4.3 DML and adiabatic chirp: effect on different formats	55
3.5 The effect of the full chirp	58
3.5.1 Interplay between full chirp and dispersion.....	58
3.5.2 Full chirp model validation	61
3.5.3 DML and full chirp: effect on different formats	65
3.6 DML deployment in HS-PONs.....	69
3.6.1 <i>ER</i> and <i>Ptx</i> optimization	69
3.6.1.1 C-band 25Gbps HS-PON with 25G DML / 10G APD	69
3.6.1.2 C-band 25Gbps HS-PON with 10G DML / 10G APD	72
3.6.1.3 O-band 50Gbps HS-PON with 25G DML / 25G APD.....	74
3.6.1.4 DML-based HS-PON over 20km – Summary.....	77
3.6.2 Multiple distance systems: the overall feasible region.....	78
3.6.2.1 C-band 25 Gbps HS-PON with 25G DML/10G APD	78
3.7 Conclusions	83
Chapter 4: Equalization for burst-mode transmission.....	84
4.1 The need for a burst-mode equalization algorithm	84
4.2 Adaptive equalization: the LMS algorithm.....	86
4.3 Simulation setup.....	89
4.3.1 Single-ONU Single-Burst assumption.....	91
4.3.2 Relation between BER and MSE	92
4.4 Step size optimization	94
4.4.1 PAM-2 results.....	95
4.4.2 PAM-4 and EDB results	98
4.4.3 The influence of training sequence length	99
4.5 Initial coefficients optimization.....	100
4.6 Evolution of local MSE over time.....	104
4.7 Evolution of local BER over time	110
4.8 Conclusions	112
Chapter 5: Experimental results on burst-mode equalization.....	114
5.1 Experimental setup.....	114
5.2 Results	115
5.2.1 Single burst analysis.....	115
5.2.2 Multi-bursts processing.....	116
5.3 Conclusions	117
Chapter 6: Conclusions and future work.....	118
References	120

ACKNOWLEDGMENTS

I wish to sincerely thank my supervisors, professors R. Gaudino and V. Ferrero, for giving me the opportunity to work with them on the interesting topics treated in this thesis work. I would also like to express my appreciation to Pablo Torres Ferrera for his huge patience in assisting me anytime I was in trouble (quite often, I would say). It's thanks to all of them that I had an extremely instructive and gratifying experience, both from an academic and a human point of view.

In addition, I'm deeply grateful to everyone who was close to me and supported me, in any way, in this little part of my life called "Master Thesis". I'm referring to my family, my friends, my loved ones and, in particular, C. .

LIST OF ACRONYMS

ADC	Analog-to-Digital Converter
AWG	Arbitrary Waveform Generator
AGC	Automatic Gain Control
APD	Avalanche Photodiode
BBU	Baseband Unit
BER	Bit Error Rate
CO	Central Office
C-RAN	Cloud Radio Access Network
CPRI	Common Public Radio Interface
CW	Continuous Wave
CoMP	Coordinated Multi-Point
DFE	Decision Feedback Equalizer
DSP	Digital Signal Processing
DD	Direct Detection
DML	Directly Modulated Laser
DML-A	Directly Modulated Laser Adiabatic-dominated
DML-T	Directly Modulated Laser Transient-dominated
DFB	Distributed feedback
DFB	Distributed Feedback
DS	Downstream
EDB	Electrical Duobinary
EML	Electro-absorption Modulated Laser
EAM	Electro-absorption Modulator
EICIC	Enhanced Inter-Cell Interference Coordination
EFM	Ethernet in the First Mile
EPON	Ethernet Passive Optical Network
ER	Extinction Ratio
FFE	Feed Forward Equalizer
FTTH	Fiber To The Home
FTTx	Fiber To The x
FIR	Finite-duration Impulse Response
FEC	Forward Error Correction
FSAN	Full Service Access Network
G-PON	Gigabit-capable Passive Optical Network
HS-PON	High-speed Passive Optical Network
IRND	Input-referred Noise Density
IEEE	Institute of Electrical and Electronics Engineers
IM	Intensity Modulation
ITU-T	International Telecommunication Union – Telecommunications Standardization Sector
LMS	Least Mean Square
LBMRx	Linear Burst-Mode Receiver

LTE	Long Term Evolution
LPF	Low-Pass Filter
MZM	Mach Zehnder Modulator
MLSE	Maximum Likelihood Sequence Estimation
MSE	Mean Square Error
MIMO	Multiple-Input Multiple-Output
NFV	Network Functions Virtualization
NG-PON	Next-generation Passive Optical Network
NRZ	Non-Return-To-Zero
NZDSF	Non-zero Dispersion-shifted Fiber
ODN	Optical Distribution Network
ODB	Optical Duobinary
OLT	Optical Line Terminal
ONU	Optical Network Unit
PON	Passive Optical Network
PMD	Physical Medium Dependent
P2MP	Point-to-multipoint
PIN	Positive-Intrinsic-Negative
PRBS	Pseudo-random Bit Sequence
PAM	Pulse Amplitude Modulation
RAN	Radio Access Network
RTO	Real Time Oscilloscope
ROP	Received Optical Power
RX	Receiver
RRU	Remote Radio Unit
SSMF	Standard Single-mode fiber
TWDM	Time and Wavelength Division Multiplexing
TDMA	Time Division Multiple Access
TDM	Time Division Multiplexing
TIA	Trans-impedance Amplifier
TX	Transmitter
US	Upstream
VOA	Variable Optical Attenuator
V-RAN	Virtual Radio Access Network
WDM	Wavelength Division Multiplexing

ABSTRACT

The continuously increasing demand for high bitrate applications (let's think of high definition videos, virtual reality, cloud computing, support to upcoming mobile network standards...) rises the need for improving the performance of the access to the network for residential and business users. To date, the most widely deployed Fiber to The Home (FTTH) solution for fixed network access (last mile) is the passive optical network (PON), which exploits a completely passive point-to-multipoint (P2MP) architecture to connect the optical line terminal (OLT) at the central office (CO) side with the optical network units (ONUs) at user side. A single fiber leaves the OLT. Then, along the optical distribution network (ODN), passive optical splitters are placed, aiming at breaking out the optical signal onto separate fibers that run to the final users, in a tree-like point-to-multipoint structure [1].

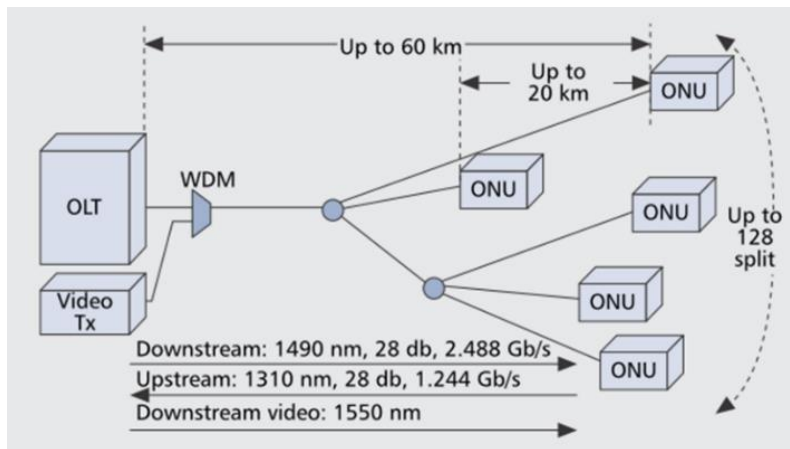


Figure 0.1. Physical architecture of a PON. In particular, the wavelength Division Multiplexing (WDM) parameters (i.e. the different wavelengths used respectively for downstream/upstream data and downstream video), along with power budget (in dB), upstream/downstream data rates, fiber lengths and splitting factors as specified by the G-PON standard are reported. Picture from [1].

Since the late 1990s, different PON standards have been discussed and proposed by the two main working groups, Full Service Access Network (FSAN) and Ethernet in the First Mile (EFM). The final versions were eventually released by the two main standardization bodies, respectively ITU-T and IEEE. This thesis work moves in the context of next-generation High-Speed PONs (HS-PON) and, in particular, it investigates the possibility to achieve higher serial bitrates, larger than the 10Gbps per wavelength of current standards, in a TDM/TDMA PON. In particular, we focus on the target of 25 Gbps and 50 Gbps both in downstream (DS) and in upstream (US), using optoelectronics originally developed for lower bitrates. Different options are

analyzed in detail, featuring high spectral efficiency modulation formats (specifically, PAM-4 and duobinary signaling, mainly in its electrical implementation) combined to bandwidth-limited transceivers, chirp-aided transmission and equalization methods (for US and DS).

The thesis Chapters are organized as follows.

The first Chapter provides an overview of the results achieved by the latest standards proposed until now and outlines the main motivations and requirements for working on next-generation PONs. An introduction to electrical/optical duobinary (EDB/ODB), promising modulation formats for application to future PONs, is given, as well.

The actual starting point of my thesis work, based on a research carried out in [2] is introduced in the second Chapter. In particular, the impact of a realistic band-limited receiver on a 25 Gbps PON system O-band performance is analyzed with a simulative approach. The study provides several useful graphs (specifically, contour plots of penalty versus the receiver filtering characteristics B_{3dB} and B_{20dB} , for different modulation formats in US and DS), which could serve as guidelines for transceiver and systems designers. Also, optimistically, graphs of that kind (together with those in [2]) could help in making choices during the standardization process of future PON systems in FSAN and/or EFM working groups.

In the third Chapter we analyze the possibility of obtaining a cost-effective rate increase in PONs using direct modulation of the laser (DML) at transmitter side. This implies dealing with the laser chirp phenomenon, which arises whenever the laser used for transmission purpose is directly modulated. A theoretical overview of this phenomenon (with particular emphasis on the separated and joint effects of its transient and adiabatic components) and of its interaction with chromatic dispersion is provided, along with the DML model implementation and validation versus experimental results found in the literature. Our simulations show that the use of a DML, besides being convenient from a cost point of view, can take advantage of the adiabatic component of the chirp (this aspect, together with its application to PONs, was very little treated in the previous literature). The latter, interacting with chromatic dispersion, can help increasing the system reach, regardless of the sign of the dispersion parameter D (which is what instead matters for the more well-studied transient chirp component). Based on simulation results, we discuss some feasible options for use in next generation PONs. In particular, we demonstrate the feasibility of 25Gbps transmission (with the help of adaptive equalization) over 20km in C-band using 25G-class DML at transmitter side and 10G-class Avalanche Photodiode (APD) at

receiver side and of 50Gbps transmission over 20 km in O-band using 25G-DML / 25G-APD, thanks to the beneficial interaction between adiabatic chirp and chromatic dispersion. It is also shown that a 25Gbps transmission over 20 km in C-band using 10G-DML / 10G-APD is not too far from being possible, especially when PAM-2 modulation is used and FFE is exploited at receiver. Contrarily, it is not possible to find points of operations able to guarantee 50Gbps transmission over 20 km in C-band using 25G-DML / 25G-APD. All of these results are briefly summarized in Table 0.1.

$R_b = 25 \text{ Gbps}$	25G DML / 10G APD (C-band)	10G DML / 10G APD (C-band)	$R_b = 50 \text{ Gbps}$	25G DML / 25G APD (O-band)	25G DML / 25G APD (C-band)
PAM-2	✓	X*	PAM-2	✓	X
EDB	✓	X	EDB	✓	X
PAM-4	✓	X	PAM-4	X	X

*Close to feasibility. Further details in Chapter 3.

Table 0.1. Summary tables of the DML-based HS-PON feasibility results for 25Gbps (on the left)/50Gbps (on the right) transmission over 20km long fiber. Different modulation formats have been analyzed. The transmission is declared as “feasible” if a region of the (ER, P_{tx}) plane exists which can guarantee a power budget $PB \geq 29dB$.

Additionally, an example of feasibility assessment is provided in the case of multiple-length systems, as typical PONs are: feasible regions contour plots (using extinction ratio ER and transmitted power P_{tx} as variables) are derived similar to the ones reported in Figure 0.2, which could be quite relevant, in view of future HS-PONs definitions.

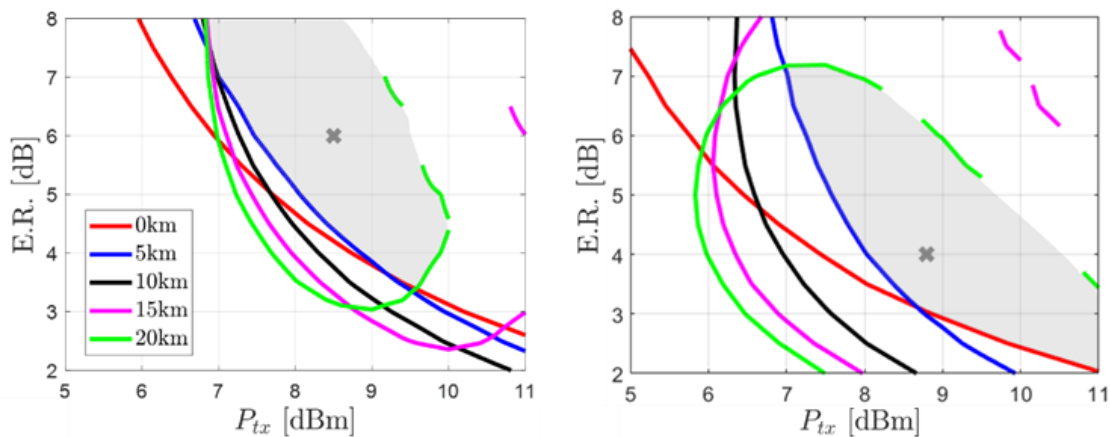


Figure 0.2. Regions of operation in the (ER, P_{tx}) plane which guarantee feasibility (i.e. $PB \geq 29dB$) of 25Gbps EDB (on the left) and PAM-2 (on the right) continuous-mode transmission in C-band (for different fiber lengths 0km-20km), using 25G-DML/10G-APD. The overall feasible regions are highlighted, along with an operational point in the middle of each.

Nevertheless, these promising simulation results need to be verified through a proper set of experiments on commercial lasers. This has not actually been possible, due to lack of a suitable bandwidth DML in the laboratory experimental inventory, but is going to be done in the near future.

The fourth Chapter specifically focuses on US, with the aim of analyzing adaptive equalization strategies specifically tailored for burst-mode transmission, based on feed-forward equalization (FFE) with Least Mean Square (LMS) algorithm. The main requirements and the optimization of the main parameters (step size μ , training sequence length N_{TM} , initial tap coefficient state) are discussed, based on simulative results. As relevant results, we demonstrate that:

- a burst-mode equalization performance analysis based on average BER (and/or average MSE) over a large payload, as it was done in some of the papers found in the literature, may lead to erroneous conclusions about the convergence rate of the equalization algorithm employed. In order to be on the safe side, carefully defined local performance metrics (fine time-resolved BER and fine-time resolved MSE) should be adopted;
- based on the latter performance metrics, it can be shown that a memory-aided equalization approach (using memory from previous bursts of the same ONU for initializing the equalizer tap coefficients) presents several advantages compared to a memory-less one (Figure 0.3). In particular, we prove that a memory-aided approach such as the described EQ-MEM can work in full-training (i.e. without any training bit) ensuring low BER since the very beginning of the payload (left plot of Figure 0.3), thus enabling high data transmission efficiency. On the contrary, a memory-less taps initialization strategy would require few thousands training bits of overhead, which would be “wasted” (right plot of Figure 0.3).

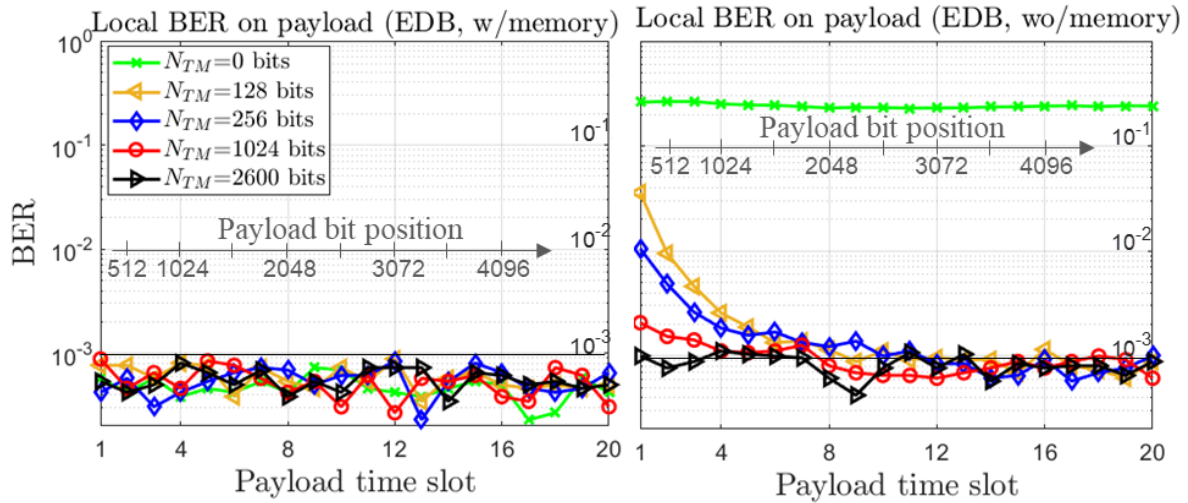


Figure 0.3. Fine time-resolved BER evaluated along the payload for EQ-MEM (on the left) and for a memory-less approach (on the right; the initial equalizer tap coefficient state is set equal to a delta with optimized middle value) for 25Gbps EDB burst-mode transmission in C-band, using 25G-DML/10G-APD.

These results have been corroborated by experiments, presented in Chapter 5 (experimentally demonstrating 25Gbps burst-mode US transmission in C-band using 10G-class APD), and included in a paper submitted in October 2018 to the main Conference of the field (OFC2019).

The last Chapter aims at summing up the overall study and drawing the conclusions and possible future developments on the topics.

Chapter 1: Motivations and background

In this Chapter we provide the main motivations for working in the area of PONs and, in particular, to the definition of next generation standards. Some hints are given about the current PON deployment (Section 1.1) and the main challenges (Section 1.2) and requirements (Section 1.3) on the way towards next-generation high-speed PONs (HS-PONs). Finally, some theoretical background is provided about duobinary encoding (Section 1.4), which, as we will see in the rest of the thesis work, represents a promising option and a good candidate for use in future standards.

1.1 PONs Today

Nowadays, the most widely deployed PON standard to provide Fiber to the x (FTTx) services to both residential users and business, is the G-PON (ITU-T G.984). The latter, standardized in 2008, is by now a mature standard and it is foreseen to be the dominating one in terms of OLT port shipments in the next few years [3]. What made the G-PON technology more appetible with respect to previous ones was its gigabit capability (indeed, its name stands for “Gigabit-capable PON”). Indeed, G.984, which anyway presents different options in terms of bitrates, is typically implemented for 2.5 Gbps downstream and 1.25 Gbps upstream.

All of the PON technologies standardized after G-PON aimed at increasing the network capacity, but always paying attention to several design criterions such as:

- the reuse of the existing infrastructure;
- the coexistence with previously developed versions;
- the necessity to keep the optoelectronic devices and transceivers as low cost as possible (especially at user side).

With these purposes, in the context of ITU-T, 10Gbps-capable PON (XG-PON) and 10Gbps-capable Symmetrical PON (XGS-PON) were standardized, respectively in 2010 and in 2016. The former allows for 10 Gbps downstream and up to 2.5 Gbps upstream, while the latter targets a symmetrical (i.e. both US and DS) 10 Gbps. The Next-Generation PON 2 (NG-PON2, G.989), standardized in 2015, instead, through a Time and

Wavelength Division Multiplexing (TWDM) approach allowing the stacking of 4 (or more) different wavelengths enables for up to 40 Gbps downstream (or more).

The timeline in Figure 1.1 reports a simple graphical overview of the evolution of PON standards over the years.

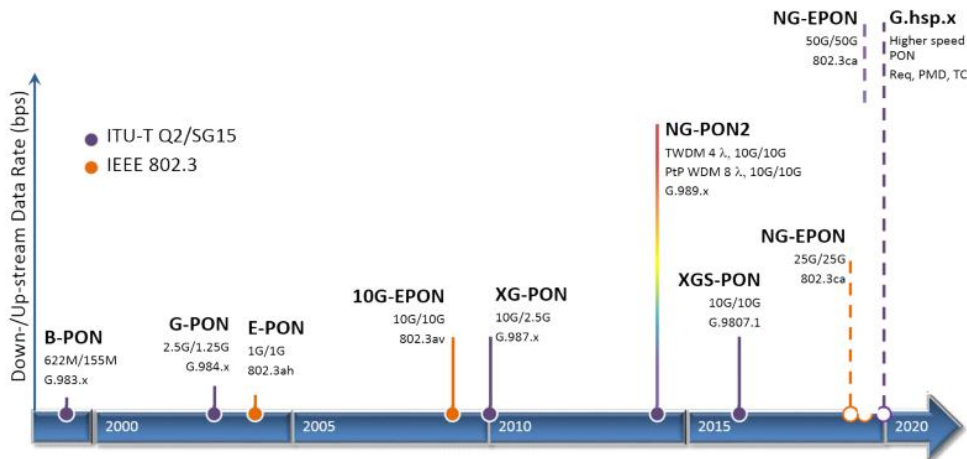


Figure 1.1. Timeline of the ITU-T and IEEE standards for PON. Picture drawn from [4].

1.2 The need for High-Speed Passive Optical Networks (HS-PONs)

Despite the most widely deployed technology today is still the G-PON one, still the standardization bodies (ITU-T, IEEE) and the FSAN/EFM working groups are currently putting much effort on the definition of the physical layer features for a next-generation high-speed PON. The current standardization timeline for 25/50/100G EPON from IEEE is reported in Figure 1.2.

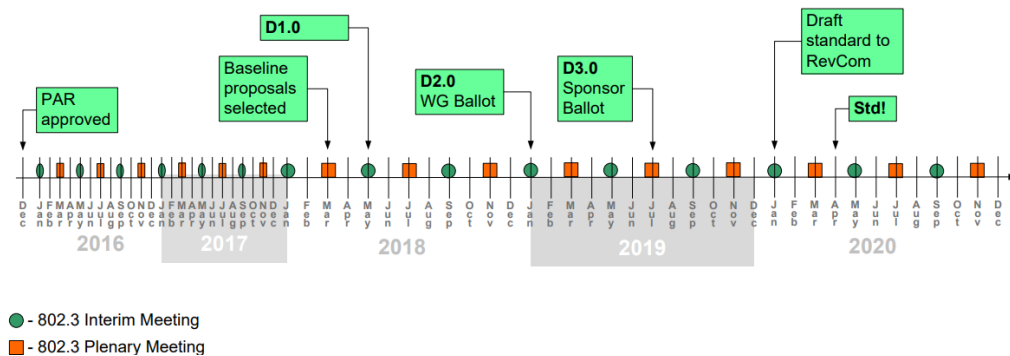


Figure 1.2. IEEE p802.3ca timeline. Image taken from [5]

In general, the target for HS-PON is an increase in the serial bitrate per single wavelength: in particular, rates under discussion are 25 Gbps (nearly close to standardization), 50 Gbps and 100 Gbps¹. This could serve both for standardizing a hypothetical future high-rate single-wavelength PON technology and as a per-wavelength upgrade of NG-PON2 [6].

The main drivers for such an effort have to be found not only in the FTTH provisioning to residential (and business) users but also in other relevant business applications, such as the enabling of the future highly performing mobile networks. Very high-speed links will be required between the base stations and central offices (HS-PON is going to represent a cost-effective solution for mobile backhauling over Ethernet [6]) and to support the mobile fronthauling paradigm in the upcoming 5G cellular standard. For instance, a recently proposed efficient implementation of the latter foresees the use of a “Mobile PON” [7]. That’s why it is foreseen that next PON technologies will probably be more and more mobile-oriented [3], corroborating the necessity for a fixed-mobile convergence.

1.2.1 Example: the fronthaul in the C-RAN architecture

In the context of next generation Radio Access Networks (RANs), the concept of C-RAN (and, as a consequence, V-RAN) is gaining more and more consensus. The advantages of this approach reside in the simplification of the network architecture (deriving from the centralization of network functions) together with a significant performance improvement (deriving from the use of more advanced multi-antenna signal processing techniques based on centralization). The main idea can be explained as follows.

¹ E.g. In the context of IEEE, the 100G EPON Task Force is currently working on the definition of a low cost solution for next-generation EPON (802.3ca) targeting 25Gbps line rate (optimized for cost) and, by means of channel bonding, also 50Gbps and 100Gbps [5].

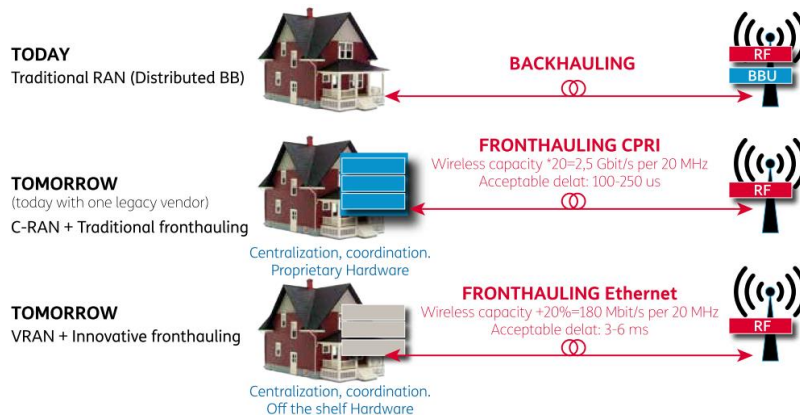


Figure 1.3. Graphical exemplification of the transition from legacy RAN to C-RAN and V-RAN approaches. Picture taken from [8].

The base station of a cellular network is composed by two main parts: the radio frequency front-end, typically called Remote Radio Unit (RRU) and the baseband part, typically called Base Band Unit (BBU). In the legacy standards, these two sections are settled in the same site, interconnected through fiber with a Common Public Radio Interface (CPRI) which provides fronthauling. BBUs are then connected to central offices (and thus to the core network) by means of the backhaul section (upper scheme of Figure 1.3). This approach is decentralized, being the BBUs spread over different base station sites. Though, some of the techniques proposed in LTE-Advance, such as Carrier Aggregation, advanced Multiple-Input Multiple-Output (MIMO) techniques, Coordinated Multi-Point (CoMP) and enhanced Inter-Cell Interference Coordination (eICIC), require the coordination among different BBUs. This can efficiently be achieved by moving all the BBUs of a given area to a single point, e.g. pooling them in a BBU-hotel inside a central office (middle scheme in Figure 1.3). This offers the advantages of performance optimization, together with a reduction in the quantity of deployed equipment and a saving of cost and power supply. The functionalities of the equipment in the antenna site are reduced to a bare minimum: the received analog waveform is just digitized through an Analog-to-Digital Converter (ADC) and the resulting samples are sent via fronthauling to the Centralized RAN (C-RAN). Nevertheless, the capacity required to the fronthaul can be much larger (e.g. ~ 2.5 Gb/s for each 20 MHz carrier in LTE using 2x2 MIMO [9]) than the actual throughput (few hundredths of Mb/s) of the mobile network: this is known as “bit-rate expansion” problem. For multi-cell and multi-frequency sites, CPRI ends up being bandwidth inefficient and thus not suitable [7, 8]. An innovative fronthauling is required (bottom scheme in Figure 1.3). Among the possible candidate options for front-hauling provisioning, we find PON. Figure 1.4 depicts the schematic of a “Mobile-PON” for C-RAN realization.

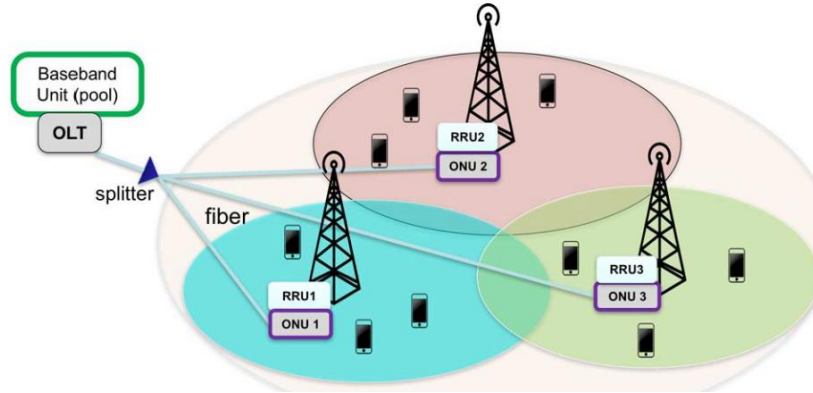


Figure 1.4. Mobile PON schematic for enabling C-RAN. Picture taken from [7].

The further step is the virtualization of the BBUs, which makes it possible to use general-purpose hardware, instead of a costly proprietary one, in a NFV fashion. This last passage marks the transition from Cloud RAN (C-RAN) to Virtual RAN (V-RAN), which will be of utmost importance in 5G standard.

1.3 HS-PON requirements

Desirable requirements for next-generation technologies are, as usual, previous infrastructure reuse, backward compatibility and low cost. In particular, the transceiver at the CO side (i.e. the OLT) is less sensitive to cost increases, being a shared resource. Instead, deploying more expensive transceiver optoelectronics at the ONUs would affect much more the overall cost. As a consequence, a wise choice would be the re-use of pre-existing optoelectronics developed for 10 Gbps technologies to achieve, with the proper modifications, the target high bitrates (e.g. 25 Gbps or even 50 Gbps). Analogously, the 25 Gbps transceivers deployed for intra-datacenter short reach communications could be re-used for 50 Gbps or, optimistically, even for 100 Gbps. Some strategies to achieve this may be found in the adoption of more bandwidth efficient modulation formats (electrical and optical duobinary formats [10], or PAM4) and/or in the use of more complex adaptive equalization algorithms in the Digital Signal Processing (DSP) section of the receiver [11]. In the following Chapters of this thesis work we will have a glance at both the options.

1.4 Which modulation formats

All the PON systems standardized so far rely on simple NRZ coding scheme and Direct Detection (DD) at the receiver side. Indeed, it can be shown that the latter is the most power efficient modulation format possible, whenever the channel bandwidth is abundant [12]. Anyway, as the transmission rates grows (e.g. beyond 10 Gbps), the channel becomes severely bandlimited due to the electrical filtering characteristics of transceivers.

High bandwidth optoelectronics is difficult to manufacture. Moreover, high bitrates induce a decrease in the chromatic dispersion tolerance of the system. This rises the need of employing advanced multi-level modulation formats featuring higher spectral efficiency and dispersion tolerance. Among the latter, the ones that yield to lower costs and lower complexity (thus IM/DD) have to be preferred for deployment in PONs. So, despite several proposals about DSP-based HS-PON using complex QAM modulations or even OFDM have been presented in the literature [13], we will mainly consider, in the following of this work, PAM-4 and duobinary (both electrical and optical) modulation formats. The choice about which modulation to use depends on considerations about the target power budget, cost and complexity. These kinds of comparisons will be performed in Chapters 2 and 3. In the rest of this Section we provide a quick overview about the duobinary modulation scheme and its implementations as electrical duobinary (EDB) and optical duobinary (ODB).

1.4.1 Duobinary signaling

In Digital Communications, Duobinary Signaling (or Correlative Coding) is a form of partial response signaling (i.e. for which the duration of the shaping pulse intentionally exceeds the symbol duration) which allows to transmit with controlled and well known inter-symbol interference (ISI) at R bps with less than $R/2$ Hz bandwidth². We should point out that this happens without contradicting the Nyquist's criterion, which assumes an uncorrelated transmitted sequence [10]. On the contrary, duobinary signaling aims at introducing intentionally a controlled amount of ISI, which can be properly removed at receiver side. The resulting transmitted sequence is a correlated signal. More in detail, the basic scheme summarizing duobinary signaling is reported in Figure 1.5. The bipolar input pulses x_k enter a simple 2-taps FIR filter (including a 1-bit delay) with equal weights. It's straightforward to verify that the resulting y_k presents two peculiar properties:

- it's a three-level signal³. E.g. if the input takes values in the set $\{-1,1\}$, due to filtering, the output will be in $\{-2,0,+2\}$;
- it's a correlated sequence. This translates into the fact that not all possible sequences of three values can occur [14]. E.g. in the above described output the only three values sequences which can occur are $\{-2,0,+2\}$ and $\{+2,0,-2\}$.

² $R/2$ Hz represents, according to Nyquist criterion for no ISI, the minimum bandwidth required for transmission without ISI. This is obtained in the case of roll-off factor $\rho = 0$, i.e. for an ideal low pass shaping filter.

³ More in general, if the input sequence was an M-levels one, the output one would be $(2M-1)$ -levels.

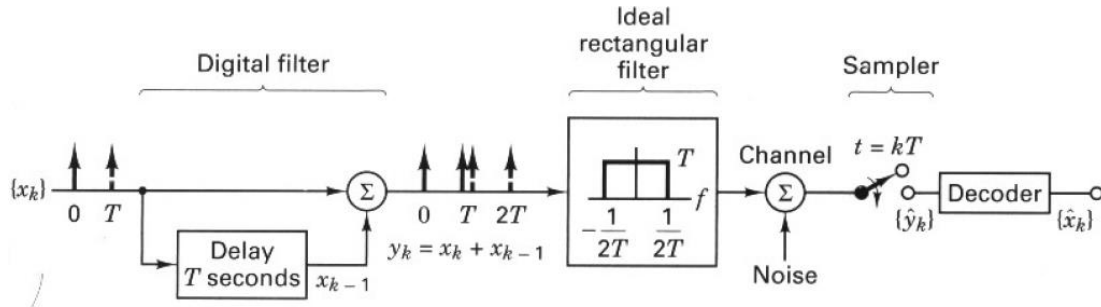


Figure 1.5. Basic scheme for a duobinary transmission system. Figure taken from [10].

The y_k sequence passes through an ideal low pass shaping filter before entering the channel. Finally, at receiver side, the duobinary decoder estimates \hat{x}_k by subtracting the previously decided \hat{x}_{k-1} from the k-th received sample \hat{y}_k . Equivalently, a simple decoding rule (translating from 3 levels to 2) can be derived, as summarized in Table 1.1.

\hat{y}_k	\hat{x}_k
+2	1
-2	-1
0	Decide for the opposite of \hat{x}_{k-1}

Table 1.1. Simplified decision rule for duobinary signaling.

The latter decision schemes are prone to error propagation, which could dramatically degrade performance. To solve this issue, a simple precoding on the binary digits (precisely, a XOR operation between present bit and the previously pre-coded one) is applied. In this case, the decoding rule is slightly changed, but still the transmitted sequence can be recovered, with the advantages of having no error propagation. The modified scheme is in Figure 1.6.

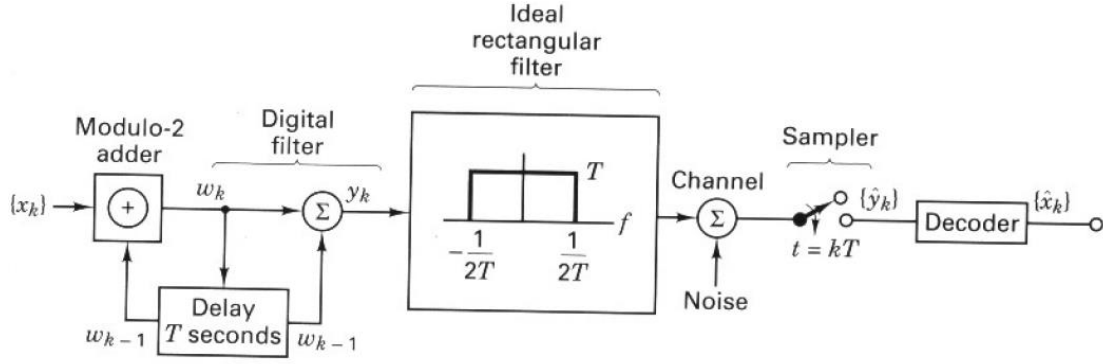


Figure 1.6. Basic scheme for a duobinary transmission system with precoding. Figure taken from [10].

It can be proven that the duobinary encoder, i.e. the cascade of the FIR filter and low pass filter, is equivalent to a cosine filter whose frequency response is [10]:

$$|H_{eq}(f)| = \begin{cases} 2T_b \cos(\pi f T_b), & |f| < \frac{1}{2T} \\ 0, & \text{otherwise} \end{cases} \quad (1.1)$$

For ease of implementation, typically a (4th or 5th order) Bessel low pass filter with proper bandwidth (\sim a quarter of the bitrate but, sometimes, larger filtering leading to incomplete duobinary conversion can compensate for band-limited transceivers [15]) is instead used. The performance of duobinary signaling may vary depending on how the encoding is implemented [15].

We should point out that, in the above described implementation, the major drawback resides in the requirement for a two-thresholds slicer at receiver, mainly due to the three-level received signal.

The technique happens to be particularly useful in optical communications for its good resilience to chromatic dispersion. In particular, in the literature, it is present in two flavors: the electrical duobinary and optical duobinary formats.

1.4.2 Electrical Duobinary

The simplest way to implement duobinary signaling into an intensity modulation with direct detection (IM/DD) system is making sure that a three-level electrical signal reaches the decision stage of the receiver. This condition, which denotes the “electrical duobinary” (EDB) format, enables the decoding process to be simply implemented

as discussed above (together with the disadvantage of a two-threshold receiver). In order to achieve this, the duobinary encoder (typically in the form of an electrical Bessel filter) can be placed either at transmitter (right before passing to the optical domain, which should anyway preserve the three levels in power) or at receiver side (right after the photodetection stage). Typically, the allocation at receiver side (receiver-encoded duobinary [16]) is preferred, so as to benefit from the performance improvements deriving from the efficient noise filtering [13]. In some cases, typically when the cascade of the transceivers and the channel is already band-limited, the filter may even be absent. An example of implementation in the downstream direction of a WDM-PON is depicted in Figure 1.7. In the latter, the choice of an external electro-absorption modulator (EAM) is arbitrary. Equivalently, different modulation schemes, such as direct modulation or Mach Zehnder, could be used. It's worth noticing that, in any case, the precoder should be put inside the transmitter, since it acts at bit level.

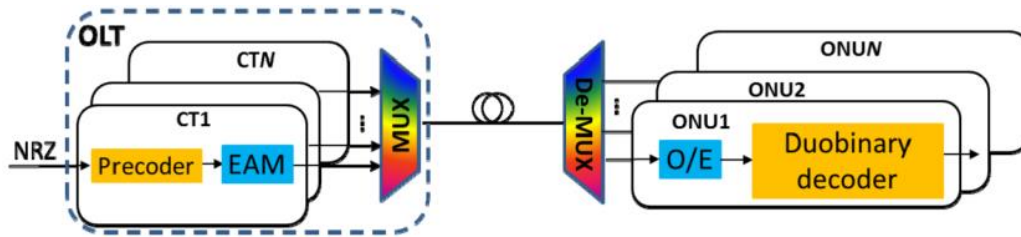


Figure 1.7. Example of system adopting the electrical duobinary scheme. Taken from [13].

1.4.3 Optical Duobinary

An alternative implementation of duobinary signaling in IM/DD systems is represented by optical duobinary [14, 17, 18]. Its use drastically simplifies the receiver architecture, at the cost of increased transmitter complexity. The use of a Mach-Zehnder modulator (MZM), which is a relatively expensive optoelectronic device, is indeed essential. The latter is biased at its point of maximum extinction (i.e. at its null point) and fed with a duobinary-encoded electrical signal with $2 \cdot V_{\pi}$ voltage swing⁴ (Figure 1.8). In this way, the highest and lowest level of the three-level signal are mapped respectively to +E and -E electric fields. The resulting signal has three levels in the optical field, which is amplitude and phase modulated, but just two levels in optical power, due to the impossibility for direct detection to recognize the field phase.

⁴ V_{π} denotes the switching voltage which leads the optical power from its maximum to its minimum.

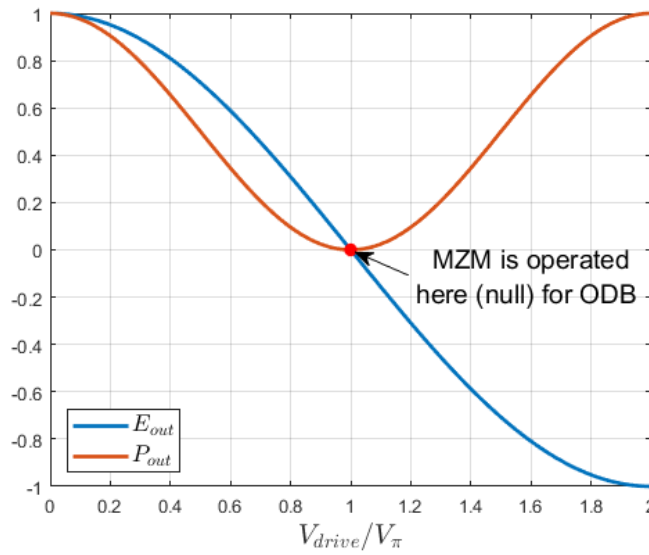


Figure 1.8. Operating point on the MZM characteristic when optical duobinary is used. The values of electrical field (E_{out}) and optical power (P_{out}) at the output of the MZM are normalized to their maximum.

A standard NRZ receiver can be used for detection, since the electrical signal at the after photodetection only has two levels.

An example of implementation in the downstream direction of a WDM-PON is depicted in Figure 1.9.

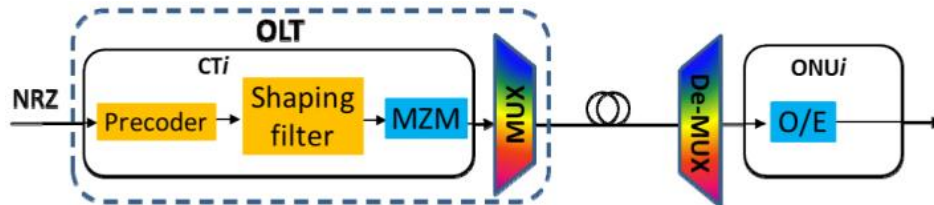


Figure 1.9. Example of system adopting the optical duobinary scheme. Taken from [13].

1.5 Conclusions

We have briefly discussed the main reasons and drivers for working in the field of HS-PONs, together with a theoretical overview of duobinary encoding. At least for now, these concepts represent most of the required background information for understanding the whole study which follows. Some other essential theoretical concepts will be provided, when needed, in the following Chapters, along with the presentation of new results carried out in the context of my thesis work.

Chapter 2: The bandwidth-dependent penalty

The main target of this Chapter is a study about the impact of an electrically bandlimited receiver on a 25Gbps PON system performance as a function of the receiver filtering characteristics. The approach is simulative and mostly based on the work presented in [2]. We firstly give a brief introduction to the problem (Section 2.1), then we present the simulation setup (Section 2.2) and the adopted system parameters (Section 2.3). Finally, we show and discuss the new results (Sections 2.4 and 2.5) and draw the overall conclusions (Section 2.6).

2.1 The starting point for this activity

In [2] the influence of the overall electrical filter shaping on 25 Gbps and 50 Gbps PON systems was considered and several useful graphs were shown describing the performance (both in back-to-back and in chromatic dispersion) for different modulation formats. The formats under discussion were PAM-2 (i.e. binary on-off keying), PAM-4 (4 levels) and the above explained (Section 1.4.1) EDB and ODB. Thanks to its simulative approach, that study had the merit of underlining an aspect which was kind of hidden in previous experimental demonstrations in the same field: in the performance analysis of a transceiver (and in its design, as well) it's not just its -3dB bandwidth that matters, but the overall filter shape. However, in order to limit the complexity, in that publication, just the -3dB and -20dB bandwidths (f_{3dB} and f_{20dB}) were taken into account. Moreover, in the above cited work, some other simplistic assumptions were made on the system:

- filtering symmetry: the transmitter and receiver were assumed to have exactly the same filtering characteristics. This is typically not true in the reality. Actually, it could also be useful to evaluate the penalty introduced in the system when only one of the transceivers (either the transmitter or the receiver) is particularly band-limited. Specifically, in this Section we will deal with the case in which the only source of bandwidth-limitations for the system the receiver;
- infinite extinction ratio (ER), which typically is not the case. Generally, the physical medium dependent (PMD) layer specifications of the PON standards suggest some minimum acceptable values [19];
- reasonable in value, but non-realistic parameters for transceivers (APD gain G , APD excess noise factor $F...$).

This first part of my thesis work focuses on the gradual relaxations of some of the latter assumptions in the case of a bitrate $R_b = 25\text{Gbps}$, with the purpose of verifying the validity of the general conclusions drawn in the above-mentioned research paper even for a more realistic simulated system.

2.2 The simulation setup

At the beginning of my activity, the simulation setup is the same as the one used in [2], i.e. the one illustrated in Figure 2.1.

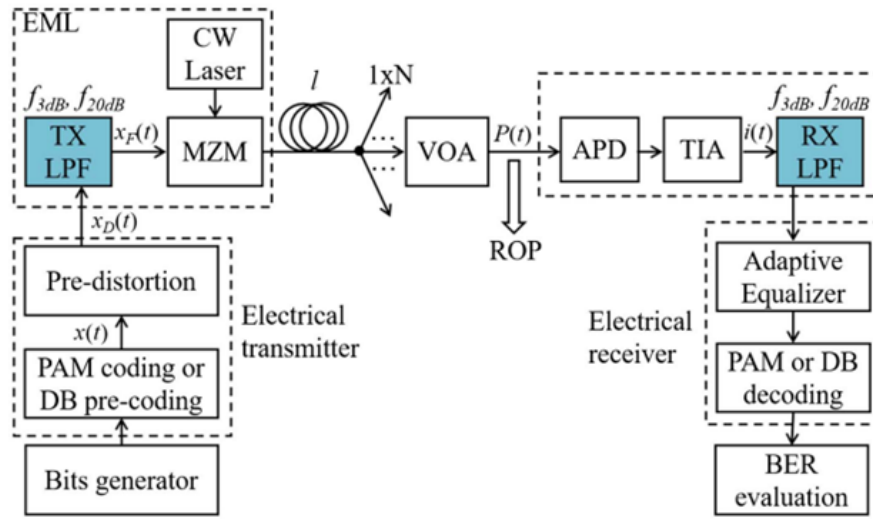


Figure 2.1. Simulation setup with external modulation. Scheme drawn from [2].

A pseudo-random bit sequence (PRBS) $2^{17} - 1$ bits long is generated, the choice of the sequence length being a trade-off between bit error rate (BER) estimation accuracy and required computational time⁵. Then, according to the chosen modulation format, a driving signal is generated by a PAM encoder (in the PAM-2 and PAM-4 cases) or by a duobinary precoder which applies a XOR-based function. A predistortion function is applied to the encoded signal in order to counteract the nonlinear transformation applied by the following MZM. The pre-distorted signal gets filtered by an electrical low-pass filter (denoted as “TX LPF” in Figure 2.1) whose aim is emulating the electrical frequency response of the transmitter.

⁵ In fact, using about 10^5 simulated bits, BER estimation is accurate down to $BER \cong 10^{-4}$.

This initial scenario only involves external modulation without chirp: a MZM is used receiving an electrical input (the driving voltage V_{drive}) and an optical one (the electrical field $E_{field,in}$ generated by the laser in continuous wave).

The optical signal is then coupled into the fiber, whose model only accounts for the chromatic dispersion phenomenon and fiber attenuation.

Photodetection at receiver side is performed through an avalanche photodetector (APD) followed by a trans-impedance amplifier (TIA), which respectively add, on top of the useful signal, a shot noise term $n_s(t)$ and a thermal one $n_T(t)$, both modeled as zero-mean Gaussian processes. In particular, the current $i(t)$ at the output of the cascade of APD and TIA can be written as [2]:

$$i(t) = G \cdot R \cdot P(t) + n_s(t) + n_T(t), \quad (2.1)$$

in which G is the APD gain (adimensional) and R is the APD responsivity expressed in A/W . The variance of the process $n_s(t)$ takes the expression [2]:

$$\sigma_s^2(t) = q \cdot G^2 \cdot F \cdot R \cdot P(t) \cdot B_{sim}, \quad (2.2)$$

in which $q = 1.6 \cdot 10^{-19} \text{ C}$ is the electron charge, F (adimensional) is the APD excess noise factor [20], $P(t)$ is the received instantaneous optical power (measured in W) at APD input and B_{sim} , in Hz , is the simulated bandwidth, computed as:

$$B_{sim} = sps \cdot R_s, \quad (2.3)$$

where sps is the number of samples per symbol and R_s is the symbol rate (i.e. the number of transmitted symbols per second).

On the other hand, the variance of the process $n_T(t)$ is given by [2]:

$$\sigma_T^2(t) = IRND^2 \cdot B_{sim}, \quad (2.4)$$

in which IRND is the Input-Referred Noise Density, measured in A/\sqrt{Hz} .

The receiver electrical frequency response is emulated through the presence of an electrical low-pass filter (denoted as “RX LPF” in Figure 2.1), which, in all of the results presented in [2], is assumed to be identical to the one at transmitter side.

In the electrical part of the receiver, adaptive equalization (20 taps FFE working at 2 samples per symbol, adopting LMS algorithm for coefficient updating [21]) is used. We will go deeper into details of equalization in Chapter 4. For now, we just assume to use it, in order to compensate as much as possible for channel induced linear distortion. After the decoding stage, the BER is measured.

It’s worth noticing that the above described scheme can be adopted both for the downstream and upstream directions of a PON system. What’s still lacking is the burst transmission feature which characterizes the upstream and will be considered in Chapter 4. Moreover, according to PON standards recommendations, the US and DS directions typically present different ER values [19].

2.2.1 Alternative receiver models

In the scheme depicted in Figure 2.1, the receiver has been modeled in such a way that the electrical filtering is applied after the noises (shot noise $n_s(t)$ due to APD and thermal one $n_T(t)$) addition. For this reason, in the following we’ll denote this modeling approach as “filter-after-noises”. The noise filtering gives a performance advantage to the simulated system albeit we cannot be sure about its physical validity. Moreover, this configuration is particularly advantageous (but not necessarily physically true!) since the receiver low-pass filter and the adaptive equalizer (which is supposed to compensate for bandwidth limitations of the full channel) are cascaded, with no noise addition in between each other. This means that, if the only bandwidth-limiting block of the system is the receiver filter of frequency response $H_{rx}(f)$, then, the equalizer could ideally compensate for it by implementing a frequency response equal to $H_{EQ}(f) \approx 1/H_{rx}(f)$. This concept is graphically exemplified in Figure 2.2.

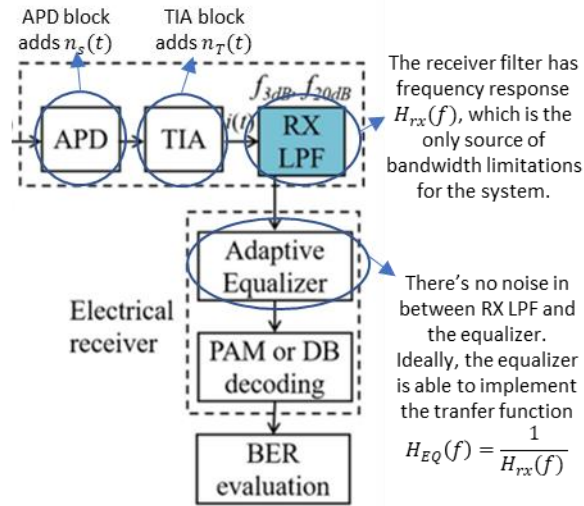


Figure 2.2. “Filter-after-noises” receiver model adopted in simulations. The text boxes explain intuitively why this particular model has to be intended as an optimistic one, in the case of a receiver-bandwidth-limited PON system.

In order to be more conservative, we proposed some different receiver models. In the “filter-between-noises” approach, the electrical filtering is applied right before the thermal noise addition (performed by the TIA block), but right after the shot noise addition (by the APD block), as illustrated in the left scheme of Figure 2.3.

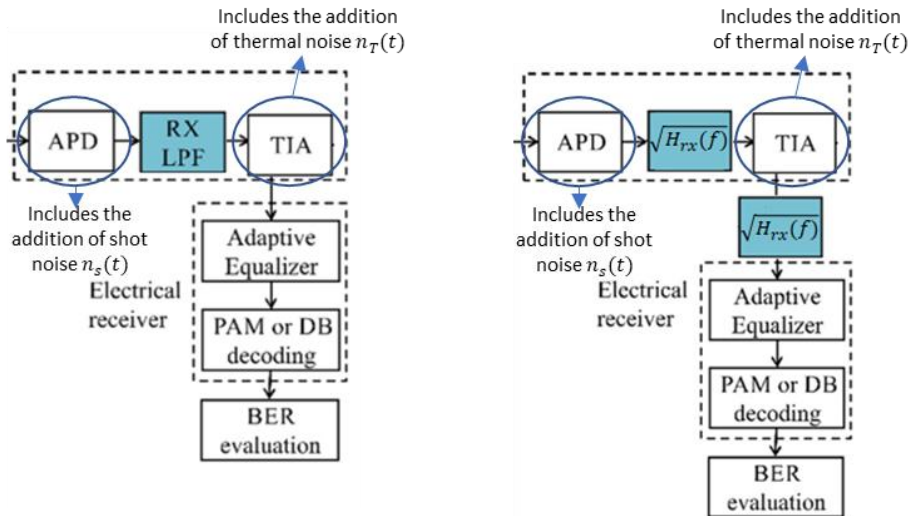


Figure 2.3. Alternative receiver models adopted in simulations: “filter-between-noises” (on the left) and “split-filter” (on the right).

On the other hand, the approach denoted as “split-filter” splits the receiver frequency response $H_{rx}(f)$ into two filters (each having frequency response equal to the square root of the original one) whose cascade gives the original one. The two “square root filters” are placed respectively right before and right after the TIA block (scheme on the right, in Figure 2.3).

2.3 Three sets of simulation parameters

In the following simulation results, three different systems, whose main parameters are reported in Table 2.1, are compared:

- the one denoted as “previous”, which uses the same parameters as in [2];
- the “realistic DS” and the “realistic US” systems whose parameters, provided to us by Telecom Italia (TIM), only differ for the ERs, which are chosen compliant with [19].

	Previous	Realistic*
G (linear units)	25	12
R [A/W]	0.8	0.85
F [dB]	10.5	6.8
ER [dB]	Infinite	8.2 (DS)
		6 (US)

*Parameters provided by Telecom Italia.

Table 2.1. Main simulation parameters adopted in simulations for the “previous” and “realistic US/DS” systems.

For all of the three systems, the transmission is at a bitrate of $R_b = 25Gbps$ over $L = 20km$ of Standard Single-Mode Fiber (SSMF) operated in O-band, i.e. for a central wavelength $\lambda \approx 1310 nm$. The electrical filters are both considered as Super Gaussian ones, thus with frequency responses that can be expressed as:

$$H(f) = \exp\left(-\frac{1}{2}\left(\frac{f}{f_0}\right)^{2n}\right), \quad (2.5)$$

in which f_0 and n (both real numbers) are free parameters. The latter can be properly tuned so as to achieve any desired combination of f_{3dB} and f_{20dB} ⁶: this is the main reason for which, in all of the simulations of this Chapter, as it also happened in [2], the filters are shaped as Super Gaussian. Moreover, in the following, we'll adopt normalized (w.r.t. the bitrate R_b) percentage representations of f_{3dB} and f_{20dB} according to the formulas:

$$B_{3dB} = \frac{f_{3dB}}{R_b} \cdot 100, \quad B_{20dB} = \frac{f_{20dB}}{R_b} \cdot 100 \quad (2.6)$$

As anticipated in Section 2.1, the constraint of filtering symmetricity between transmitter and receiver has been relaxed. In particular, we here focus on a case in which the only source of bandwidth limitations is the receiver, whose B_{3dB} and B_{20dB} have been span in some ranges of interest. As for the transmitter, its fixed filtering characteristics are chosen as:

$$B_{3dB} = 100\% ,$$

order $n = 1$ (corresponding, for a Super-Gaussian filter, to $B_{20dB} \sim 250\%$).

The ER is here defined as the ratio, expressed in dB, between the average optical power level corresponding to the highest intensity of light (P_{max}) and the average optical power level corresponding to the lowest intensity of light (P_{min}) [19]:

$$ER = 10 \log_{10} \left(\frac{P_{max}}{P_{min}} \right) \quad (2.7)$$

The latter is thus a characteristic of the transmitter and also represents one of the signal quality features affecting the receiver sensitivity and overload [19]. We choose to adopt the minimum ER values suggested by G.989.2 recommendation. Anyway, the Physical Medium Dependent (PMD) specifications allow the use of ER values lower than the suggested ones, provided that they are compensated by larger transmitted powers (within the defined limits) and that the impact on the out-of-band and out-of-channel power is taken into account [19]. The operating points for the MZM working with the two different ER values are reported in Figure 2.4 for the upstream (on the left side) and for the downstream (on the right side).

⁶ The claim holds provided that $f_{20dB} \geq f_{3dB}$.

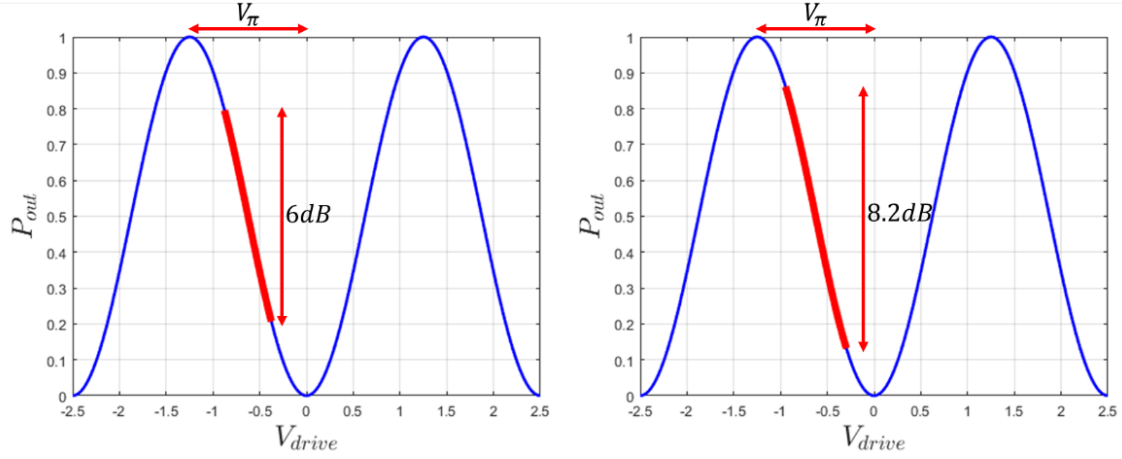


Figure 2.4. Operating points, highlighted on the MZM sinusoidal characteristic, for US (ER=6dB, on the left) and DS (ER=8.2dB, on the right) systems. The optical power at MZM output (P_{out}) is normalized to its maximum.

We finally observe that, using the above provided power-based definition of ER, the ODB format, which requires a MZM biased at null (as described in Section 1.4.3) turns out to have infinite ER⁷. For this reason, in the following of this Chapter, we'll only consider PAM-2, PAM-4 and EDB.

2.4 “Filter-after-noises” receiver results

As happened in [2], even here our main concern is the power penalty introduced into the system by the transceivers bandwidth limitations. In addition, in this slightly different scenario, we're also interested in separating, if possible, the effect of the adoption of realistic parameters from the effect of deploying a bandlimited receiver. For this reason, we decide to proceed in two steps: we firstly assume that the system is not bandwidth-limited and highlight the relative penalty between different systems. Then, we analyze the further penalty contributions introduced by a band-limited receiver. In this Section, the results are reported for the “filter-after-noises” receiver model, i.e. the same as used in [2] and depicted in Figure 2.1.

⁷ A proper definition of ER for ODB modulation should involve electrical field levels rather than optical power levels.

2.4.1 Penalty of using realistic parameters

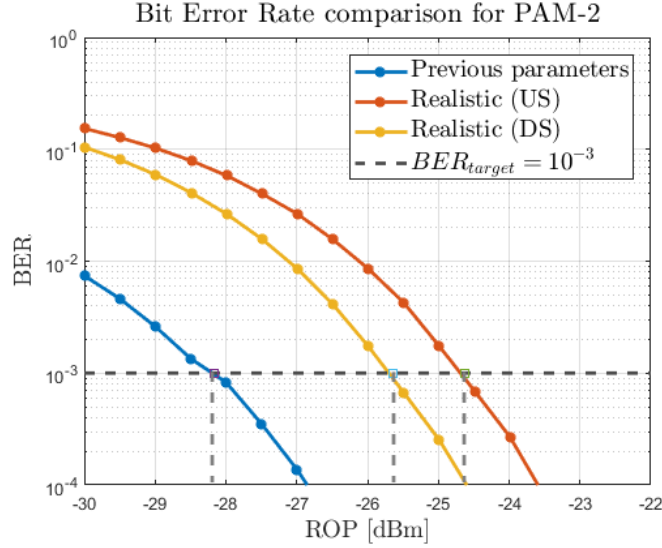


Figure 2.5. BER versus ROP curves for the three systems under analysis, with no bandwidth limitations, in case of 25Gbps PAM-2 transmission over 20 km SSMF operated in O-band. “Filter-after-noises” receiver approach is used. Main simulation parameters are as specified in Table 2.1. Adaptive equalization (20 taps FFE at 2 samples per symbols) is used at receiver side.

We can evaluate the three systems performances with no bandwidth limitations by obtaining their BER versus Received Optical Power (ROP) curves. The latter are reported in Figure 2.5 for the PAM-2 format. From Figure 2.5 the extraction of the receiver sensitivities⁸ at a target BER of 10^{-3} is straightforward and leads to the values of $S_{prev} \sim -28.2 \text{ dBm}$, $S_{real,DS} \sim -25.6 \text{ dBm}$ and $S_{real,US} \sim -24.6 \text{ dBm}$ respectively for the “previous parameters” system, the “DS realistic parameter” system and the “US realistic parameter” one. We’ll use this set of values as reference for penalty computation in most of the results of Section 2.4.2. They allow to quantify the disadvantage incurred when moving from an ideal system (“previous parameters”) to a realistic one (e.g. the DS one). For instance, whenever the sensitivities S_i are expressed in dBm, the penalty of a system 2 w.r.t. a system 1 can be computed as⁹:

$$P_{21,dB} = S_2^{dBm} - S_1^{dBm} \quad (2.8)$$

⁸ In most cases, in this work, we’ll specify the sensitivity (intended as minimum required optical power) at the BER level required at the input of the FEC encoder. We indeed assume that the system makes use of forward error correction (FEC) techniques enabling BER values of 10^{-12} or better at the FEC decoder output.

⁹ In our convention, a negative value of penalty P_{dB} actually represents an “advantage” with respect to the reference case.

We can easily verify that the realistic DS system has approximately 2.6 dB penalty w.r.t. the ideal system used in [2]. Moreover, moving to the US system requires an extra penalty of about 1 dB to be added to the loss budget (and thus to be faced by the power budget).

The same kind of analysis has been performed for PAM-4, for which the BER curves are reported Figure 2.6. The receiver sensitivities are intuitively higher than the above seen ones, due to the use of PAM-4 (the number of symbols in the constellation is doubled): for the same average received power, the distance between adjacent received symbols is reduced. The sensitivity values now become $S_{prev} \sim -23.4 \text{ dBm}$, $S_{real,DS} \sim -21 \text{ dBm}$ and $S_{real,US} \sim -19.6 \text{ dBm}$ respectively for the “previous parameters” system, the “DS realistic parameter” system and the “US realistic parameter” one.

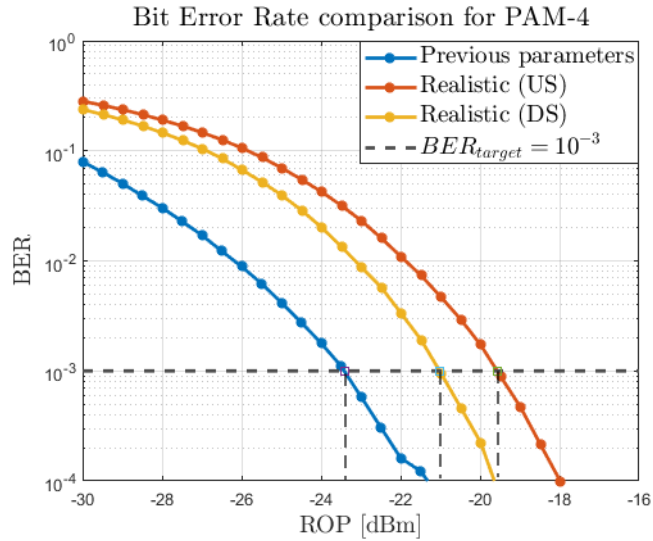


Figure 2.6. BER versus ROP curves for the three systems under analysis, with no bandwidth limitations, in case of 25Gbps PAM-4 transmission over 20 km SSMF operated in O-band. “Filter-after-noises” receiver approach is used. Main simulation parameters are as specified in Table 2.1. Adaptive equalization (20 taps FFE at 2 samples per symbols) is used at receiver side.

2.4.2 The bandwidth-dependent penalty

In order to separate the receiver bandwidth-limitation induced extra contribution to penalty, we use the above derived triad of sensitivity values in the PAM-2 case (Figure 2.5) as references for penalty computation. This means that, for every considered modulation format, we’ll compute the penalty with respect to the PAM-2 bandwidth unlimited case. We denote the set S_0 of reference sensitivities as the one which includes:

$$S_{0,prev} \sim -28.2 \text{ dBm}, S_{0,real,DS} \sim -25.6 \text{ dBm} \text{ and } S_{0,real,US} \sim -24.6 \text{ dBm}.$$

2.4.2.1 PAM-2 results for bandwidth-limited cases

The penalty contour-plots for the three systems are reported in Figure 2.7 for the PAM-2 format. On the two axis we report the values of normalized receiver -3dB bandwidth (B_{3dB}) and -20dB bandwidth (B_{20dB}). As largely stressed in [2], it turns out that, in general, the -3dB bandwidth alone is not enough for drawing conclusions about the system performance. Indeed, even for very low values of B_{3dB} , the power penalty strongly depends on the overall filter shaping and, in particular, on the filter steepness determined by the particular value of B_{20dB} . As an example, for $B_{3dB} = 10\%$ in the “realistic DS” system (middle plot in Figure 2.7), the penalty may theoretically range from 0.15dB to 5dB (if we only limit our reasoning to the bandwidth ranges used in our simulations) depending upon B_{20dB} . Obviously, the bandwidth-dependent penalty reduces as the filter bandwidth enlarges (upper-right areas of the plots in Figure 2.7).

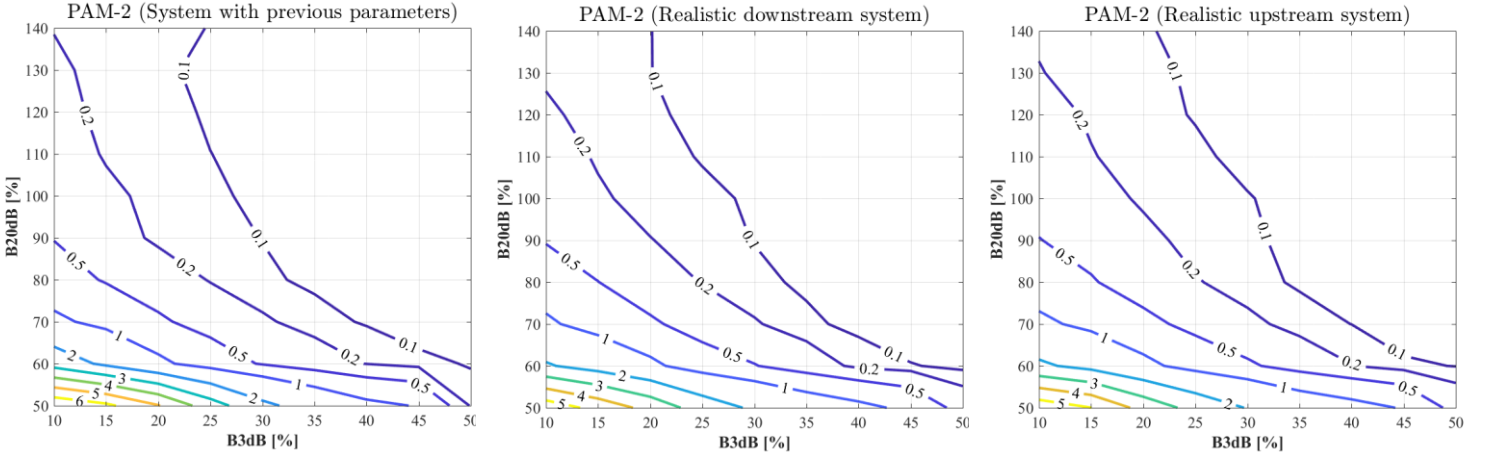


Figure 2.7. Bandwidth-dependent penalty contour-plots of “previous parameters” system (plot on the left), “realistic DS” system (in the middle) and “realistic US” system (on the right) for 25Gbps PAM-2 transmission over 20 km SSMF operated in O-band. The reference sensitivities w.r.t. which the penalties are computed are different for the 3 cases (sensitivity values of the PAM-2 bandwidth-unlimited case, denoted in the text as S_0 set). “Filter-after-noises” receiver approach is used. Main simulation parameters are as specified in Table 2.1. Adaptive equalization (20 taps FFE at 2 samples per symbols) is used at receiver side.

It’s clear that using different sensitivity references for each system allowed us to extract the bandwidth-dependent penalty. Interestingly, the latter seems to be almost the same regardless of the considered system parameters. In order to prove this last claim, we show in Figure 2.8 that the lines of the three contour plots of Figure 2.7 almost superimpose each other. This confirms, at least in this scenario, our hypothesis about the

possibility of separating the realistic-parameters-induced penalty from the bandwidth-induced one, and allows to interpret the curves reported in Figure 2.8 as quite general for any reasonable APD-based receiver.

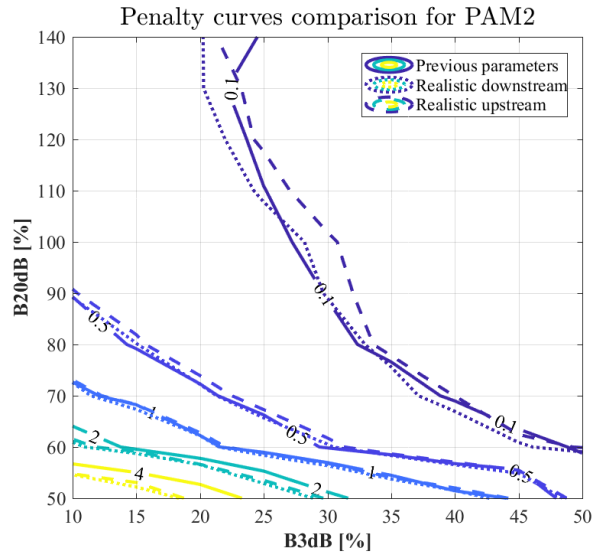


Figure 2.8. Penalty curves comparison of “previous parameters” system, “realistic downstream” system and “realistic upstream” system for 25Gbps PAM-2 transmission over 20 km SSMF operated in O-band. The reference sensitivities w.r.t. which the penalties are computed are different for the 3 cases (sensitivity values of the PAM-2 bandwidth-unlimited case, denoted in the text as S_0 set). “Filter-after-noises” receiver approach is used. Main simulation parameters are as specified in Table 2.1. Adaptive equalization (20 taps FFE at 2 samples per symbols) is used at receiver side.

2.4.2.2 PAM-4 results for bandwidth-limited cases

As for PAM-4 modulation format, the penalty contour plots referred to the PAM-2 case with no bandwidth limitations (i.e. with penalties referred to the above defined set S_0 of reference sensitivities) are reported in Figure 2.9. We notice that, despite we attempted to remove the penalty contribution due to different parameters set, still in this case the “realistic US” system (plot on the right in Figure 2.9) ends up having always higher residual (i.e. to be added on top of the S_0 sensitivities) penalties than the other 2 systems. Moreover, for any pairs (B_{3dB}, B_{20dB}) , the residual penalties for the “previous parameters” system (plot on the left in Figure 2.9) turn out to be slightly higher than the ones for the “realistic DS” one (plot in the middle of Figure 2.9). Anyway, for all of the systems, the value of the penalty presents very little variations with respect to the receiver bandwidth. This means that PAM-4 modulation format results in being more resilient to receiver bandwidth limitations than PAM-2.

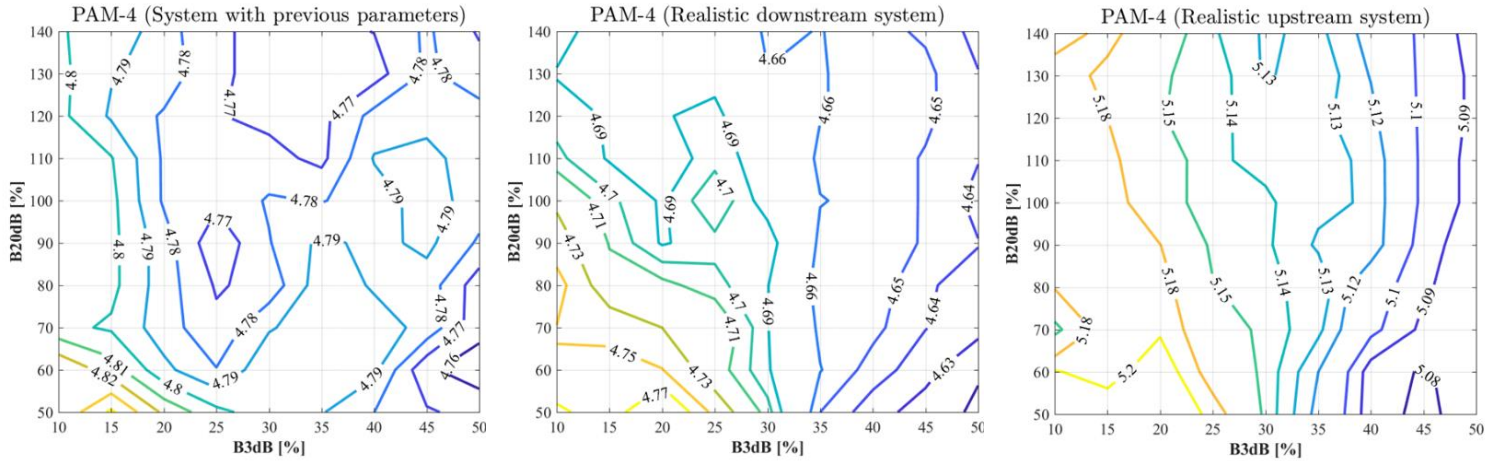


Figure 2.9. Bandwidth-dependent penalty contour-plots of “previous parameters” system (plot on the left), “realistic DS” system (in the middle) and “realistic US” system (on the right) for 25Gbps PAM-4 transmission over 20 km SSMF operated in O-band. The reference sensitivities w.r.t. which the penalties are computed are different for the 3 cases (sensitivity values of the PAM-2 bandwidth-unlimited case, denoted in the text as S_0 set). “Filter-after-noises” receiver approach is used. Main simulation parameters are as specified in Table 2.1. Adaptive equalization (20 taps FFE at 2 samples per symbols) is used at receiver side.

In Figure 2.10 also the superimposition of several penalty lines from the three systems is shown. In this case, differently than Figure 2.9, for each system the penalty is computed by taking as a reference the sensitivity set for a PAM-4 transmission with no transceivers bandwidth limitations (i.e. the set of sensitivity values shown in Figure 2.6). The absolutely negligible penalty values of Figure 2.10 confirm the major tolerance of PAM-4 to bandwidth variations.

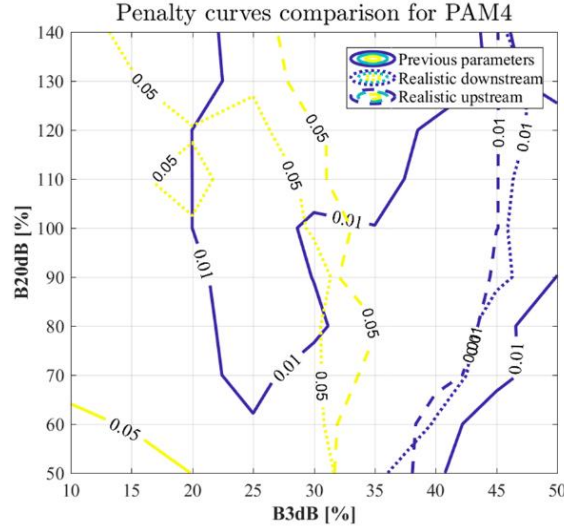


Figure 2.10. Penalty curves comparison of “previous parameters” system, “realistic downstream” system and “realistic upstream” system for 25Gbps PAM-4 transmission over 20 km SSMF operated in O-band. The reference sensitivities w.r.t. which the penalties are computed are different for the 3 cases (chosen equal to the sensitivity values of the PAM-4 case with no bandwidth limitations). “Filter-after-noises” receiver approach is used. Main simulation parameters are as specified in Table 2.1. Adaptive equalization (20 taps FFE at 2 samples per symbols) is used at receiver side.

2.4.2.3 EDB results for bandwidth-limited cases

The same kind of results as above have also been obtained for EDB modulation formats. The penalty contour plots referred to PAM-2 with no bandwidth limitations (i.e. with penalties referred to the above defined set S_0 of reference sensitivities) are reported in Figure 2.11. In this case, the “larger” (relatively) penalty values are concentrated in the region in which B_{3dB} is high: this is due to the fact that bandwidth limitations are actually somehow beneficial to EDB, since they help in the generation of the 3 levels (as previously explained in Section 1.4.2). Anyway, once again, as it happened with PAM-4, the penalty range is very little: EDB proves to be very tolerant to bandwidth limitations. This is also highlighted by Figure 2.12, which shows a pretty close agreement in the behavior of the bandwidth-dependent penalty (again, absolutely negligible) computed w.r.t. the EDB non-bandwidth-limited case.

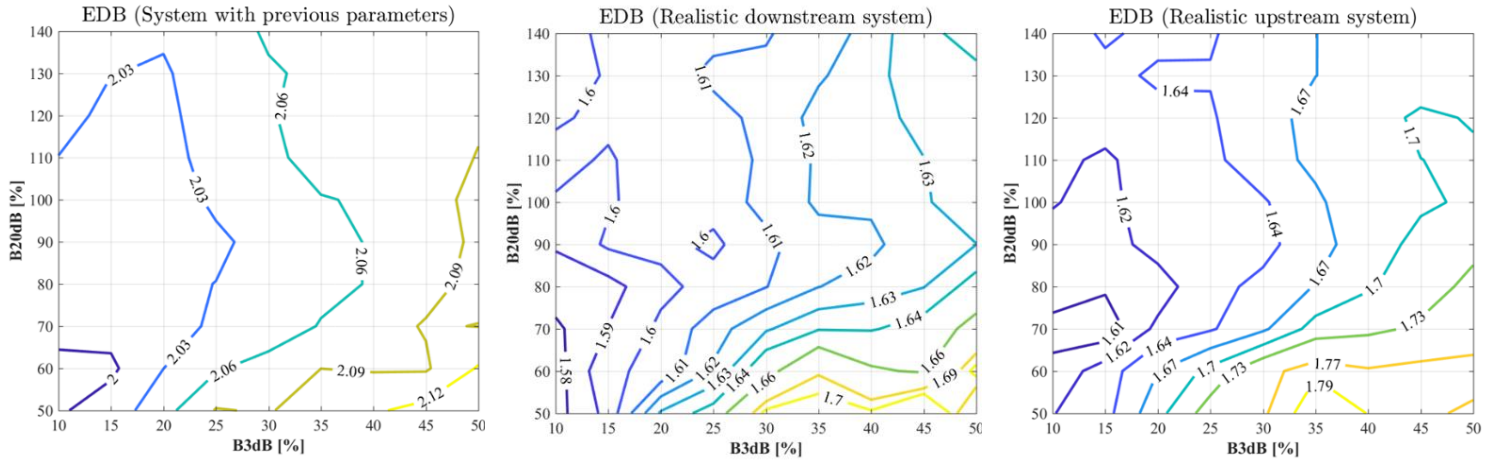


Figure 2.11. Bandwidth-dependent penalty contour-plots of “previous parameters” system (plot on the left), “realistic DS” system (in the middle) and “realistic US” system (on the right) for 25Gbps EDB transmission over 20 km SSMF operated in O-band. The reference sensitivities w.r.t. which the penalties are computed are different for the 3 cases (sensitivity values of the PAM-2 bandwidth-unlimited case, denoted in the text as S_0 set). “Filter-after-noises” receiver approach is used. Main simulation parameters are as specified in Table 2.1. Adaptive equalization (20 taps FFE at 2 samples per symbols) is used at receiver side.

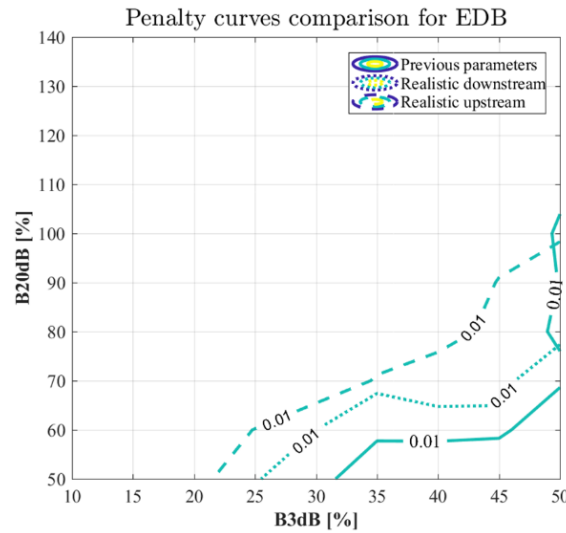


Figure 2.12. Penalty curves comparison of “previous parameters” system, “realistic downstream” system and “realistic upstream” system for 25Gbps EDB transmission over 20 km SSMF operated in O-band. The reference sensitivities w.r.t. which the penalties are computed are different for the 3 cases (chosen equal to the sensitivity values of the EDB case with no bandwidth limitations). “Filter-after-noises” receiver approach is used. Main simulation parameters are as specified in Table 2.1. Adaptive equalization (20 taps FFE at 2 samples per symbols) is used at receiver side.

2.5 Results with alternative receiver models

The same kind of analysis as described in Section 2.4 has been repeated using the alternative receiver models introduced in Section 2.2.1. The aim is to evaluate to what extent the conclusions derived above (in Section 2.4)

are bound to the particular optimistic receiver model employed and how much they would vary in a less favorable scenario. For ease of comparison, the results for the two alternative receiver setups are presented in parallel.

2.5.1 Penalty of using realistic parameters

The BER versus ROP curves for PAM-2 and PAM-4 formats in the non-bandwidth-limited case are reported for the “filter-between-noises” and the “split-filter” receiver models, respectively in Figure 2.13 and Figure 2.14. As expected, the sensitivity values at $BER = 10^{-3}$ are always higher than the ones required in the “filter-after-noises” configuration (Figure 2.5 and Figure 2.6): the higher required ROP for achieving the same BER is here due to the receiver architecture suboptimality. Anyway, these receiver-setup-induced penalties mainly involve PAM-2 and, anyway, always remain confined within less than $\sim 0.6dB$. Contrarily, the PAM-4 performance proves to be insensitive (“penalties” are in the order of $\sim 0.01dB$) to the adopted receiver model.

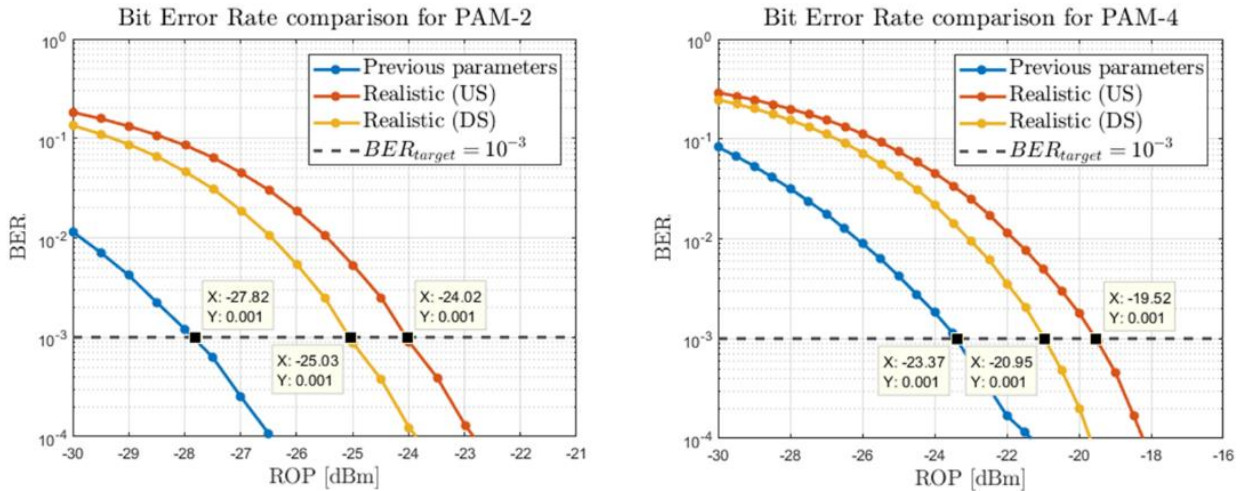


Figure 2.13. BER versus ROP curves for the three systems under analysis, with no bandwidth limitations, in case of 25Gbps PAM-2 (on the left) and PAM-4 (on the right) transmission over 20 km SSMF operated in O-band. “Filter-between-noises” receiver model is adopted. Other simulation parameters are as specified in Table 2.1. Adaptive equalization (20 taps FFE at 2 samples per symbols) is used at receiver side.

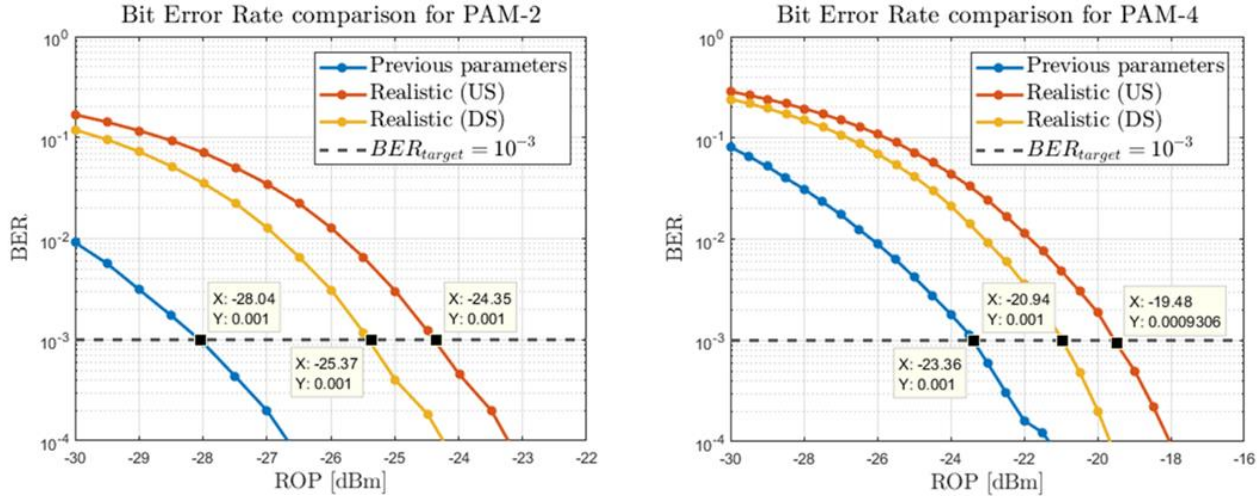


Figure 2.14. BER versus ROP curves for the three systems under analysis, with no bandwidth limitations, in case of 25Gbps PAM-2 (on the left) and PAM-4 (on the right) transmission over 20 km SSMF operated in O-band. “Split-filter” receiver model is adopted. Other simulation parameters are as specified in Table 2.1. Adaptive equalization (20 taps FFE at 2 samples per symbols) is used at receiver side.

Between the alternative receiver structures, the most limiting one is the “filter-between-noises”, mainly due to the thermal noise component which is kept unfiltered.

2.5.2 The bandwidth-dependent penalty

We now present, in a more compact way than in Section 2.4.2, the behavior of the bandwidth-dependent penalty under different receiver model hypothesis. The comparative (for different parameters sets) contour plots are reported in Figure 2.15, Figure 2.16 and Figure 2.17 respectively for PAM-2, PAM-4 and EDB. The alternative receiver structures bring a further penalty (more pronounced in the “filter-between-noises” case) to the system, which is anyway a limited one. The major changes, anyway pertain to PAM-4 and EDB formats, for which the strong resilience to bandwidth variations demonstrated in the “filter-after-noises” case slightly weakens. Indeed,

Figure 2.16 and Figure 2.17 show some more “pronounced” penalties (w.r.t. to what we have seen in Section 2.4) which are anyway below 1 dB.

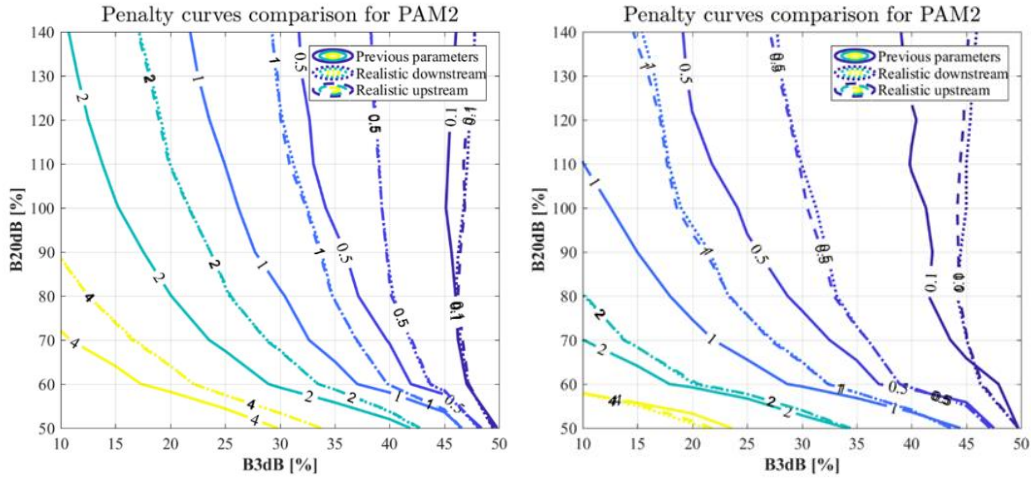


Figure 2.15. Penalty curves comparison of “previous parameters” system, “realistic downstream” system and “realistic upstream” system for 25Gbps PAM-2 transmission over 20 km SSMF operated in O-band. “Filter-between-noises” (on the left plot) and “split-filter” (on the right plot) receiver approaches are used. The reference sensitivities w.r.t. which the penalties are computed are different for the “previous parameters”, “realistic US/DS” systems (chosen equal to the sensitivity values of the PAM-2 case with no bandwidth limitations). Other simulation parameters are as specified in Table 2.1. Adaptive equalization (20 taps FFE at 2 samples per symbols) is used at receiver side.

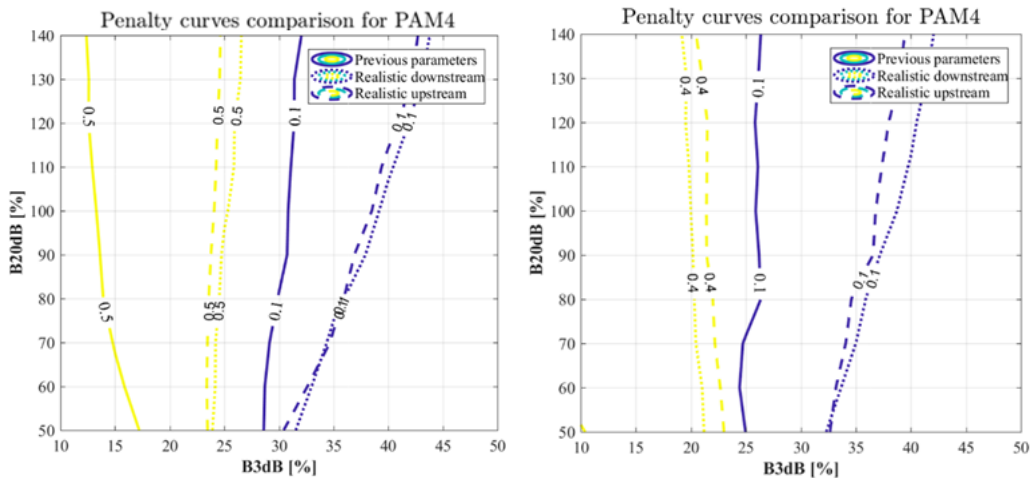


Figure 2.16. Penalty curves comparison of “previous parameters” system, “realistic downstream” system and “realistic upstream” system for 25Gbps PAM-4 transmission over 20 km SSMF operated in O-band. “Filter-between-noises” (on the left plot) and “split-filter” (on the right plot) receiver approaches are used. The reference sensitivities w.r.t. which the penalties are computed are different for the “previous parameters”, “realistic US/DS” systems (chosen equal to the sensitivity values of the PAM-4 case with no bandwidth limitations). Other simulation parameters are as specified in Table 2.1. Adaptive equalization (20 taps FFE at 2 samples per symbols) is used at receiver side.

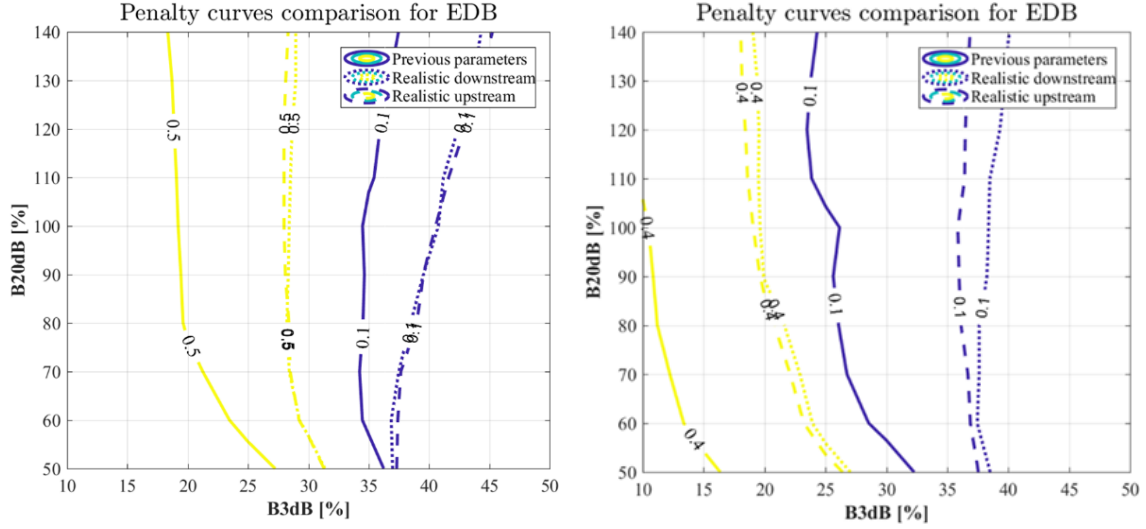


Figure 2.17. Penalty curves comparison of “previous parameters” system, “realistic downstream” system and “realistic upstream” system for 25Gbps EDB transmission over 20 km SSMF operated in O-band. “Filter-between-noises” (on the left plot) and “split-filter” (on the right plot) receiver approaches are used. The reference sensitivities w.r.t. which the penalties are computed are different for the “previous parameters”, “realistic US/DS” systems (chosen equal to the sensitivity values of the EDB case with no bandwidth limitations). Other simulation parameters are as specified in Table 2.1. Adaptive equalization (20 taps FFE at 2 samples per symbols) is used at receiver side.

Another peculiarity of these results with alternative receiver structure lies in the impossibility of separating completely the realistic parameters induced penalty from the bandwidth induced ones. In particular, in all of the plots of Figure 2.15, Figure 2.16 and Figure 2.17 we notice that the “previous parameters” lines do not coincide with the “realistic parameters US/DS” ones (which instead are always pretty close each other) and actually they often end up in being relatively far.

2.6 Conclusions

In this Chapter we have been studying the impact of a bandlimited receiver on a PON system O-band performance as a function of the receiver filtering characteristics and for different modulation formats. Moreover, as a novelty w.r.t. the work presented in [2], we also considered realistic parameters from real transceivers provided by TIM and distinguished between the upstream and downstream systems. We finally proposed three different schemes for receiver modeling. The graphs shown can serve as guidelines for transceiver and systems designers, but also, they can help the standardization process of future PON systems.

Chapter 3: Direct modulation in HS-PONs

In this Chapter the main focus is on transmission with directly modulated lasers. Firstly, the use of direct modulation in PONs is justified (Section 3.1), then some theoretical background is provided (Section 3.2) along with a detailed analysis, model development, validation and simulation results about transient chirp (Section 3.3), adiabatic chirp (Section 3.4) and their joint effect on the performance of a DML/DD system (Section 3.5). Finally, in Section 3.6 some options for cost-efficient HS-PONs based on DML are proposed, based on simulative results. Conclusions are drawn in Section 3.7.

3.1 The use of a directly modulated laser (DML)

Until now we've been focusing on systems which made use of external modulation of a laser. In particular, a Mach Zehnder modulator (which is a quite expensive optoelectronic device) was used in transmission. In alternative, still in the context of external modulation, an electro-absorption modulated laser (EML) could be used. Anyway, there are several reasons which make directly modulated lasers a more desirable alternative to external modulation. Among them we find simplicity, small size, lower cost, low driving voltage and high optical output power [22] [23], which, coincidentally, are fundamental requirements in PONs.

This can thus serve as a motivation for the study of the performance of a PON in the case in which a directly modulated laser (DML) is used. For this purpose, in this Chapter we introduce in the previously considered system a DML block (Figure 3.1).

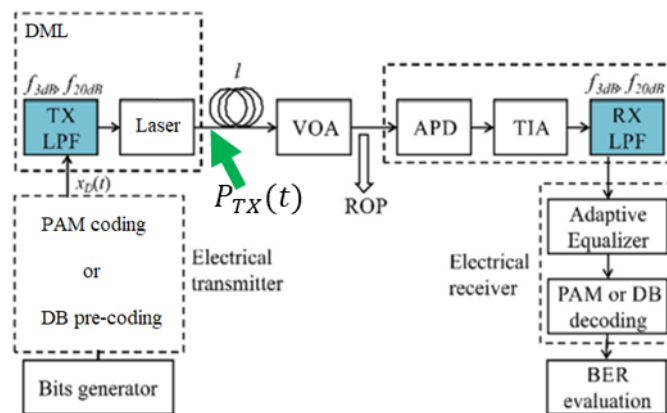


Figure 3.1. Simulated system setup including the DML block. It's worth noticing that the (average) transmitted power is defined at the output of the DML.

In the DML block, the laser is no longer operated in continuous wave (CW), as it happened in previous Chapters. Conversely, the modulating signal (a current) is applied directly to the laser input, so that the output power carries the information in the form of an amplitude modulation. In reality, this process comes together with a spurious frequency modulation, the frequency chirp, which is typically an unwanted effect. The phenomenon is even more complex: in case of dispersive fibers, the interplay between chirp and dispersion is non-trivial. In the following of this Chapter we'll analyze all of these aspects using our simulative approach. The study has, as a goal, an investigation about the best options (transmission parameters, modulation formats...) to be used in DML-based HS-PONs for enabling data rates higher than 10 Gbps per wavelength.

3.2 The frequency chirp: a theoretical background

Whenever a laser (e.g. a Distributed Feedback Laser (DFB)) is directly modulated, due to the varying current at its input, a modification in the carrier density in the semiconductor is generated, altering the refractive index. This is what gives rise to the unwanted frequency modulation which goes under the name of chirp. The effect of this phenomenon is a broadening of the spectrum of the signal, which thus may become more vulnerable to chromatic dispersion. The immediate consequences are a reduction in the dispersion-limited system reach and an increased power penalty. Anyway, under certain conditions, chirp may also happen to be beneficial in counteracting chromatic dispersion [24].

Typically, the instantaneous frequency deviation (typically simply called “chirp”) of a chirping laser, obtained by analytical resolution of the laser rate equations [22], is described by:

$$\Delta\nu(t) = \frac{\alpha}{4\pi} \left(\frac{1}{P(t)} \frac{dP(t)}{dt} + k \cdot P(t) \right) \quad (3.1)$$

where $P(t)$ is the laser output optical power. In Eq. 3.1 we distinguish two fundamental terms. The first one is the transient (or “dynamic”) chirp term, which is mainly related to the transitions (derivative of output power) between different levels (e.g. “on” and “off”) of the signal; its effect in time domain when combined with chromatic dispersion is a variation in the pulse width (broadening or compression, depending on operative conditions) [25]. From Eq. 3.1, we point out that the transient chirp term only involves the linewidth enhancement factor (or Henry’s factor) α , which is an adimensional parameter. Typical values for α (which is always positive) span in the range [2,6]. The second important chirp component is the adiabatic (or “static”) one, which is instead proportional to the output power: this means that different levels of the optical signal will

experience different frequency shifts. In time domain, in presence of chromatic dispersion, the effect is a timing shift between the different power levels of the signal [26]. The magnitude of the adiabatic chirp coefficient k (which is measured in Hz/W) is what actually determines if the laser behavior is dominated by adiabatic or transient chirp. In general, both the components exist, but, as we will see in the following, depending on the operative conditions and on laser material and design parameters, one may be prevailing above the other [25]. Moreover, we'll see that in some special cases, it may be convenient to act on transmission parameters in order to make one chirp component dominate above the other. E.g. using a bias current much higher than the threshold current would induce an adiabatic dominated behavior [27].

3.3 The separated effect of transient chirp

In the following subsections we firstly expose some theoretical concepts about the transient chirp component (Section 3.3.1), then we present some simulations results aiming both at validating our model (Section 3.3.2) and at studying more deeply the performance of a DML/DD system (Section 3.3.3) in which the only source of chirp is the transient one.

3.3.1 Interplay between transient chirp and dispersion

In the literature, the most well-known chirp component is the transient one, whose expression is:

$$\Delta\nu_{tr}(t) = \frac{\alpha}{4\pi} \left(\frac{1}{P(t)} \frac{dP(t)}{dt} \right) \quad (3.2)$$

In this case ($k=0$ in Eq. 3.1) analytical expressions to compute the broadening of chirped gaussian pulses have been found by Agrawal [24].

In order to understand what happens to a pulse affected by the combined effect of transient chirp and chromatic dispersion we refer to Figure 3.2.

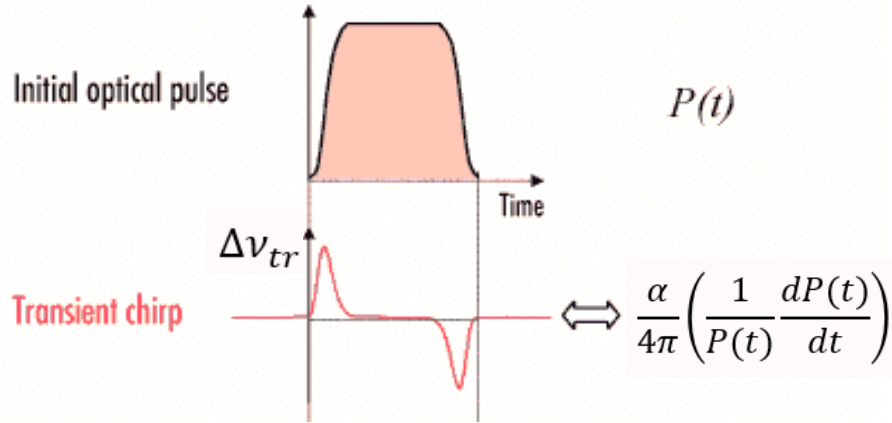


Figure 3.2. Graphical representation of the temporal evolution of the transient chirp frequency deviation $\Delta\nu_{tr}$, along with its mathematical expression. Image taken from [28].

In the case of a super-Gaussian pulse (or a general pulse), the leading edge (which has a positive derivative) and the trailing edge (which has a negative derivative), due to transient chirp (Eq. 3.2) will give rise to different chirp signs. In particular, the leading edge will have a positive frequency shift, while the trailing one will have a negative one.

As a consequence:

- in case of pulse propagation along a positive dispersion fiber ($D > 0$), e.g. a SSMF, since higher frequency components travel faster than lower frequency ones, the group delay between the leading and trailing edges is increased as D increases: this translates into a pulse broadening leading to a degradation of system performance. This implies that the distance of the system is dispersion limited;
- in case of pulse propagation along a negative dispersion fiber ($D < 0$), e.g. a non-zero dispersion-shifted fiber (NZDSF), since lower frequency components travel faster than higher frequency ones, the group delay between the leading and trailing edges initially tends to reduce leading to a pulse compression. Roughly speaking, the compression can be attributed to the combined effect of a leading edge which travels slower than expected and of a trailing edge which travels faster than expected: at the output of the fiber the two edges move toward one another. Anyway, as the modulus of the accumulated dispersion ($D \cdot L$) increases, the compression reaches a maximum, after which, a further increase in $D \cdot$

L happen to produce a pulse broadening. In this case the pulse gets “flipped” and the transient chirp/dispersion interaction is no longer beneficial.

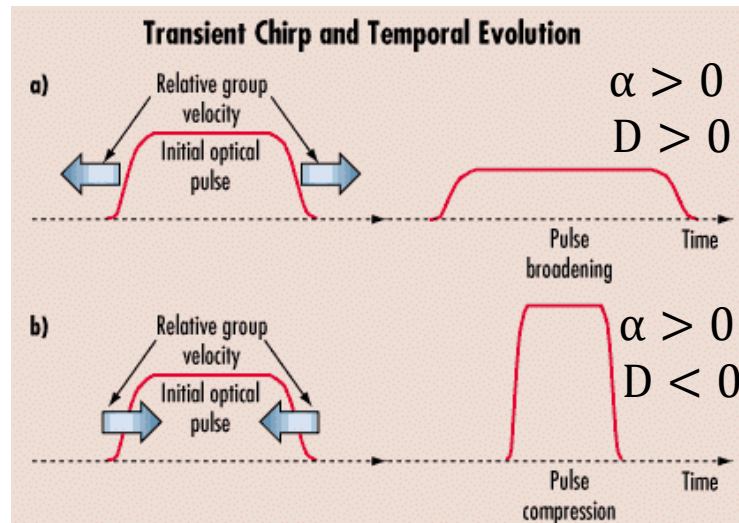


Figure 3.3. Graphical representation of the pulse distortion in transient chirp for different combinations of the α and D signs. The pulse gets broadened, leading to performance degradation, whenever α and D present the same sign. On the other hand, when α and D present different signs, the pulse gets compressed. Image taken from reference [28].

From the previous observations we may conclude that (Figure 3.3):

- if α and D have same sign, then the output pulse is broadened;
- if α and D have different sign, then it may happen that the output pulse is compressed. There is an optimum value of D (or $D \cdot L$) for which the maximum compression is reached.

So, if the only chirp component was the transient one, then, it would be convenient to operate in a condition in which the linewidth enhancement factor and the dispersion parameters have different signs. Anyway, in this work, we are interested in using a SSMF (G.652), which has a positive D for values of wavelength $\lambda > 1310 \text{ nm}$. This means that, if it was only due to transient chirp, the transmission would incur for sure a power penalty. Luckily, as we'll see in next pages, in a realistic case (which includes the adiabatic chirp component, as well) it is not always like that.

3.3.2 Transient chirp model validation

In order to prove the reliability of the model we have developed, we preventively validate it versus some of the available results in the literature. In the first place, we consider the case in which transient chirp is the only source of chirp. Our goal is to evaluate the dispersion penalty of a 25 Gbps PAM-2 system as a function of wavelength for three different modulation schemes:

- DML affected by transient chirp ($\alpha = 3.5$);
- EML affected by transient chirp of smaller entity due to a smaller value of linewidth enhancement factor $\alpha = 0.8$;
- MZM, chirp-less ($\alpha = 0$).

The main simulation parameters are summarized in the Table 3.1. Equalization at receiver side is absent. Moreover a 4th order Bessel filter with $f_{3dB} = 0.75 \cdot R_b$ is used as electrical filter at receiver. The considered wavelengths together with their values of dispersion parameter D [$ps/nm/km$] are reported in Table 3.2.

R_b	Format	TX f_{3dB}	RX f_{3dB}	ER	α
25 Gbps	PAM-2	18.75 GHz ($B_{3dB} = 75\%$)	18.75 GHz ($B_{3dB} = 75\%$)	DML: 5 dB EML: 10 dB MZM: 10 dB	DML: 3.5 EML: 0.8 MZM: 0

Table 3.1. Main parameters of the simulated system used for transient chirp model validation. In the case of extinction ratio (ER) and linewidth enhancement factor α , different modulation schemes present different values.

λ [nm]	1270	1290	1310	1330	1350	1370	1390	1410	1430	1450	1470	1490	1510	1530	1550	1570
$D(\lambda), \frac{ps}{nm \cdot km}$	-4.12	-2.11	-0.20	1.62	3.37	5.05	6.65	8.19	9.67	11.10	12.48	13.80	15.08	16.32	17.52	18.69

Table 3.2. Wavelength values considered in the simulation and their dispersion parameter values.

As the output of our simulations we obtain, for each modulation scheme (either DML, EML or MZM), a collection of curves representing BER versus ROP, each one corresponding to a different wavelength value (Figure 3.4, Figure 3.5 and Figure 3.6).

As it can be observed from the figures, as the wavelength value increases (and thus also the dispersion parameter D increases), the performance of the system gets worse. Graphically, the curves keep moving to the right as λ grows, resulting in higher required received optical power (or “sensitivity”) for achieving the target BER of 10^{-3} . In particular, there’s a maximum value of wavelength above which the system goes completely out of service (an error floor region is present and target BER cannot be achieved for reasonable values of ROP). Equivalently, one may reason in terms of accumulated dispersion ($D \cdot L$) and claim that the presence of chirp has a deleterious effect on the system reach. For instance, a transient chirp with higher value of α will increasingly limit the maximum achievable distance (wavelength) whenever the wavelength (distance) is fixed. Accordingly, for a fixed fiber length of 20 km, the three systems result in working “fine”, with a $ROP < 20dBm$, up to about 1330nm, 1430 nm and 1530 nm respectively for DML, EML and MZM (sorted for decreasing α).

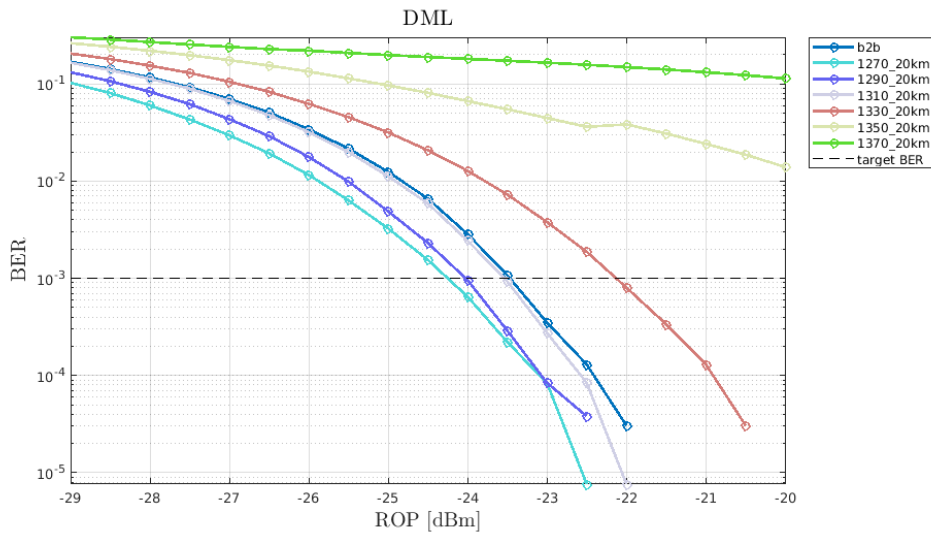


Figure 3.4. BER versus ROP curves for 25Gbps PAM-2 transmission using DML (only transient chirp) for different wavelength values over 20km of SSMF.

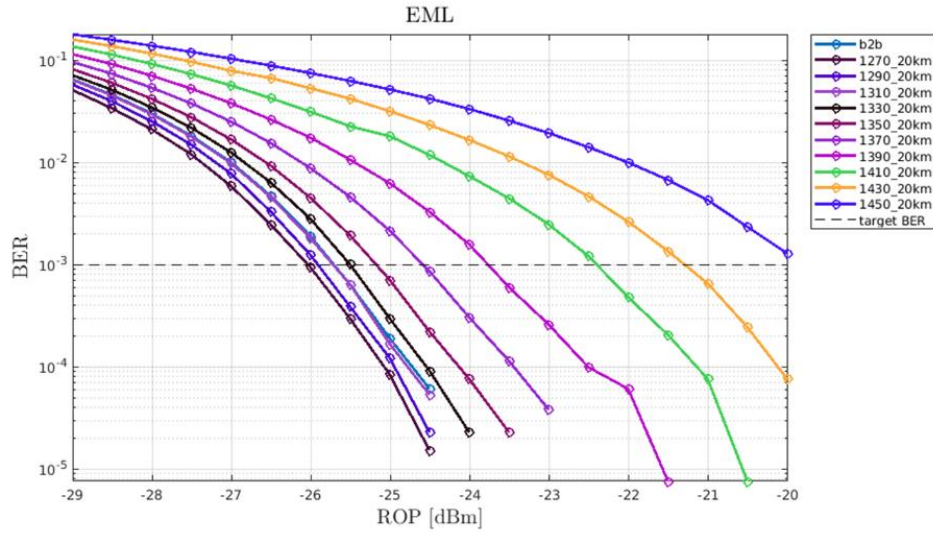


Figure 3.5. BER versus ROP curves for 25Gbps PAM-2 transmission using EML (only transient chirp) for different wavelength values over 20km of SSMF.

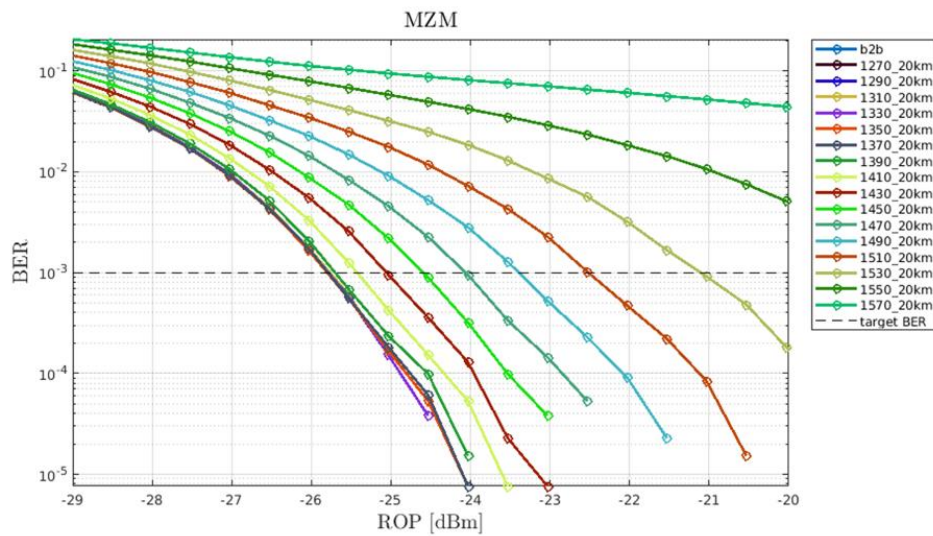


Figure 3.6. BER versus ROP curves for 25Gbps PAM-2 transmission using MZM (no chirp at all) for different wavelength values over 20km of SSMF.

The results of previous figures are summarized in the curves of Figure 3.7, which reports the penalties w.r.t. the back-to-back (“btb”, i.e. for 0 km length) sensitivity for each modulation scheme (relative penalty, each scheme has its reference). A horizontal line is traced in correspondence of the 1.5 dB penalty: this allows an easy graphical identification (interception between penalty curve and horizontal line) of the maximum wavelength values for

which the penalty is small enough and typically acceptable. The same consideration as above can be applied here. Moreover, we can further observe that:

- the crossing point for the 3 curves is, by construction, at $\lambda_{ZD} \sim 1310 \text{ nm}$, i.e. at the zero-dispersion wavelength. Indeed, at this value of wavelength the 20km system has no penalty with respect to the back-to-back sensitivity, being the accumulated dispersion $D \cdot L$ null;
- for wavelengths below $\lambda_{ZD} \sim 1310 \text{ nm}$ the chirped modulation schemes (i.e. DML and EML) present a gain. Indeed, for this wavelength range the dispersion parameter D and the linewidth enhancement factor α have different signs: the interaction between transient chirp and chromatic dispersion results in an advantage for the reasons we explained before in Section 3.3.1.

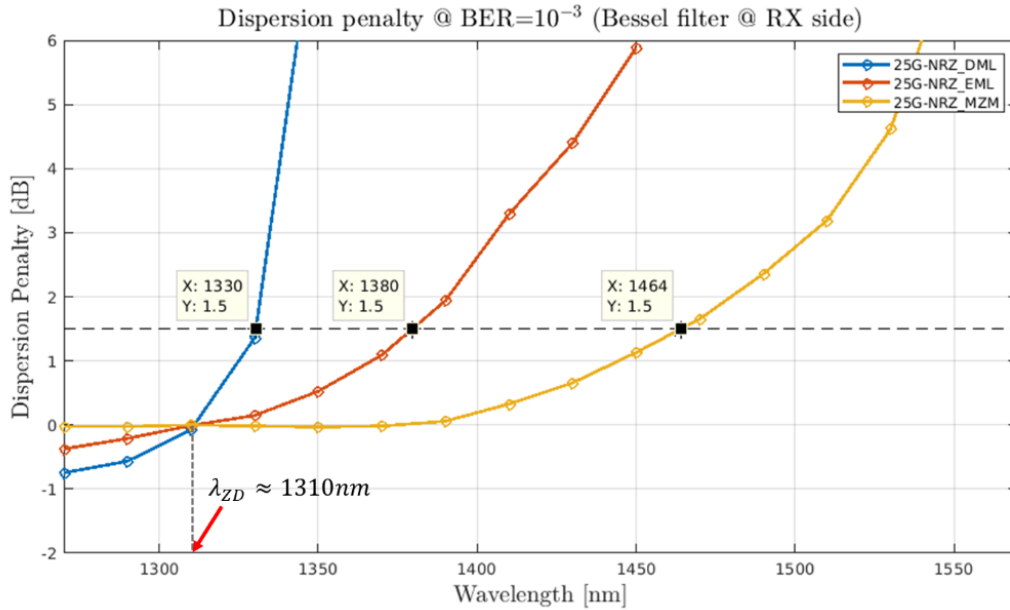


Figure 3.7. Dispersion penalty curves as a function of wavelength for 25Gbps PAM-2 transmission over 20km of SSMF. APD gain is 12. In the data tips the wavelength values for 1.5 dB penalty @BER=10⁻³ are reported for each modulation scheme. The zero-dispersion wavelength $\lambda_{ZD} \approx 1310 \text{ nm}$ is highlighted.

In Figure 3.8 the equivalent simulation results from the Huawei group is reported. Both the qualitative behaviour of the penalty curves and the wavelength values for 1.5 dB penalty show a quite close agreement of our results with the one presented by Huawei. We consider this as a validation of our DML model (at least for the transient part).

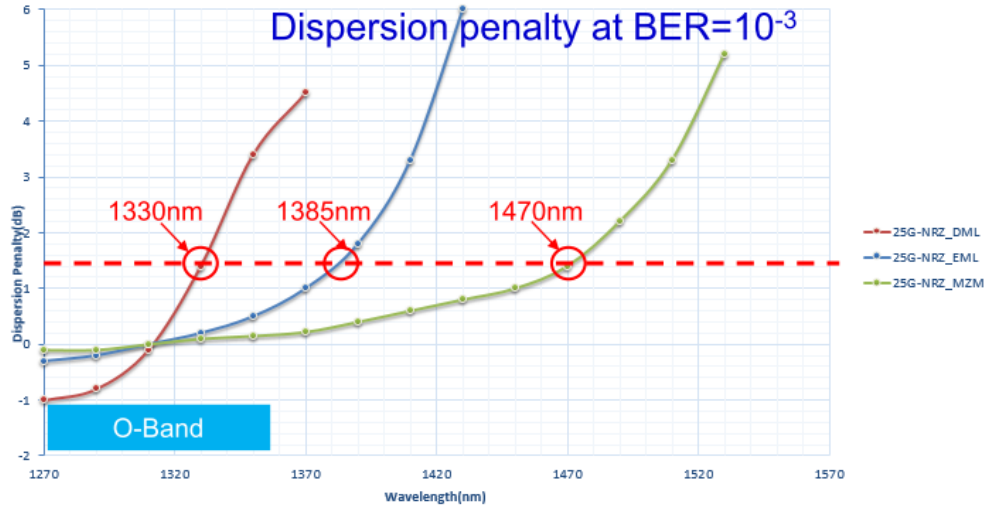


Figure 3.8. Dispersion penalty curves as a function of wavelength for 25Gbps PAM-2 transmission over 20km of fiber. Picture from Huawei group. The wavelength values for 1.5 dB penalty @BER=10⁻³ are highlighted for each modulation scheme.

An even closer agreement is shown when the APD gain (which was for us a free variable, being it not provided in Huawei publication) is set to 5 (Figure 3.9).

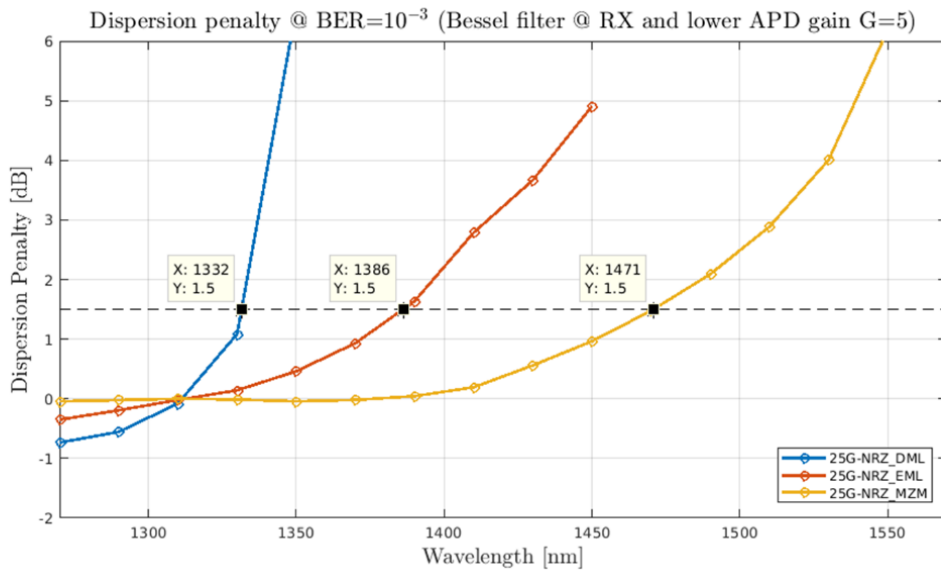


Figure 3.9. Dispersion penalty curves as a function of wavelength for 25Gbps PAM-2 transmission over 20km of fiber. APD gain is 5. In the data tips the wavelength values for 1.5 dB penalty @BER=10⁻³ are reported for each modulation scheme.

3.3.3 DML and transient chirp: effect on different formats

As a further step, we now just focus on the DML case and extend the study of the penalty versus wavelength (and thus, implicitly, versus chromatic dispersion) to other modulation formats: precisely PAM-4 and EDB. We keep fixed all of the simulation assumptions made above, except for the equalizer, which is now present in the form of a 14 taps adaptive feed forward equalizer (FFE) working at 2 samples per symbol. Again, only the transient chirp term is taken into account, so we expect the same trend as in the PAM-2 case, i.e.:

- increasing penalty values (w.r.t. back-to-back case) as wavelength (fiber length) increases, whenever the fiber length (wavelength) is fixed;
- negative penalty values for wavelengths λ such that $D(\lambda) < 0$.

This comparison helps us in understanding which is the most suitable modulation formats under our simulation hypothesis (25 Gbps transmission but with no bandwidth limitations neither at transmitter nor at receiver). Figure 3.10 reports the BER versus ROP curves for different wavelength values (fiber length being fixed to 20 km) for PAM-2.

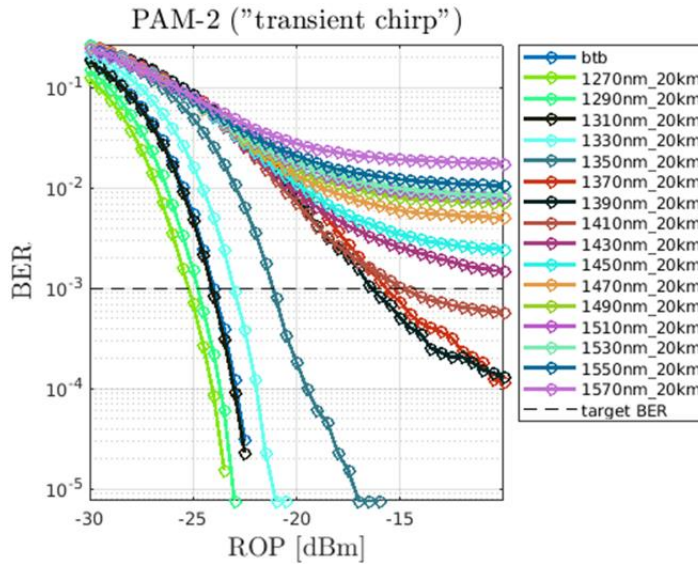


Figure 3.10. BER versus ROP curves for 25Gbps PAM-2 transmission using DML (only transient chirp) for different wavelength values over 20km of fiber. Adaptive equalization at RX is used (FFE-14).

It can be noticed that Figure 3.10 differs from Figure 3.4 mainly due to the fact that here equalization at receiver is used. The latter enables for larger values of wavelengths: as an example, when equalizer is used (Figure 3.10), the sensitivity for $BER = 10^{-3}$ at $\lambda = 1350 \text{ nm}$ is equal to $\sim -21 \text{ dBm}$. On the contrary, without equalization (Figure 3.4), at the same wavelength, a ROP strictly higher than -20 dBm would be required. The advantage of using equalization is evident from Figure 3.11, in which the penalty curves for PAM-2 with (W EQ.) and without equalization (W/O EQ.) are compared. The use of an equalizer helps in reducing the penalty (the orange curves in the plots of Figure 3.11 are always below the blue ones), thus improving the system performance at the cost of increased complexity at receiver side. In Figure 3.11 penalties are computed in two ways: either with respect to a single reference, chosen equal to the back-to-back sensitivity of the W/O EQ. case (plot on the left, in Figure 3.11), or with respect to different references for the W. EQ. and W/O EQ. cases, chosen respectively as their own back-to-back sensitivities (plot on the right, in Figure 3.11). In the latter approach, both the penalty curves (orange and blue line) cross the 0 dB line in correspondence of the zero-dispersion wavelength $\lambda_{zD} \sim 1310 \text{ nm}$.

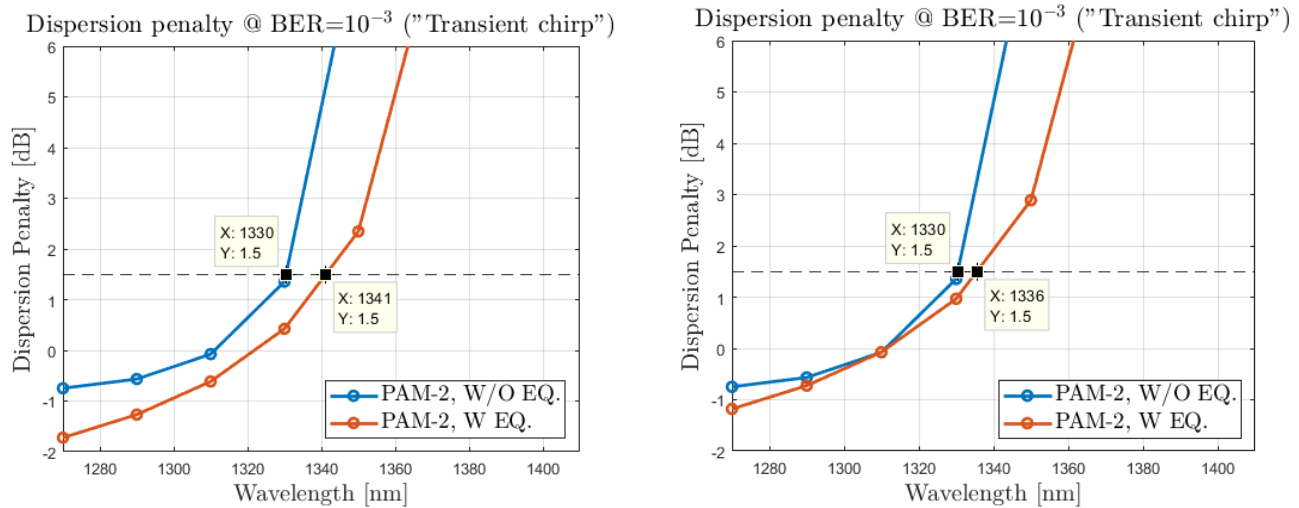


Figure 3.11. Penalty versus wavelength curves comparison for PAM-2 with (W EQ.) and without (W/O EQ.) 14 taps 2 samples/symbol FFE equalization. The penalty values can be either computed with respect to a unique reference (plot on the left; reference is the back-to-back sensitivity of the PAM-2 W/O EQ. case) or with respect to different references, chosen as the back-to-back sensitivities of W/O EQ. and W EQ. cases (on the right). Transmission is 25Gbps over 20km fiber using DML (only transient chirp); different wavelengths are considered.

The BER versus ROP curves are shown for PAM-4 and EDB respectively in Figure 3.12 and Figure 3.13. All the results of Figure 3.10, Figure 3.12 and Figure 3.13 can be finally summarized in the comparative penalty versus wavelength plots of Figure 3.14.

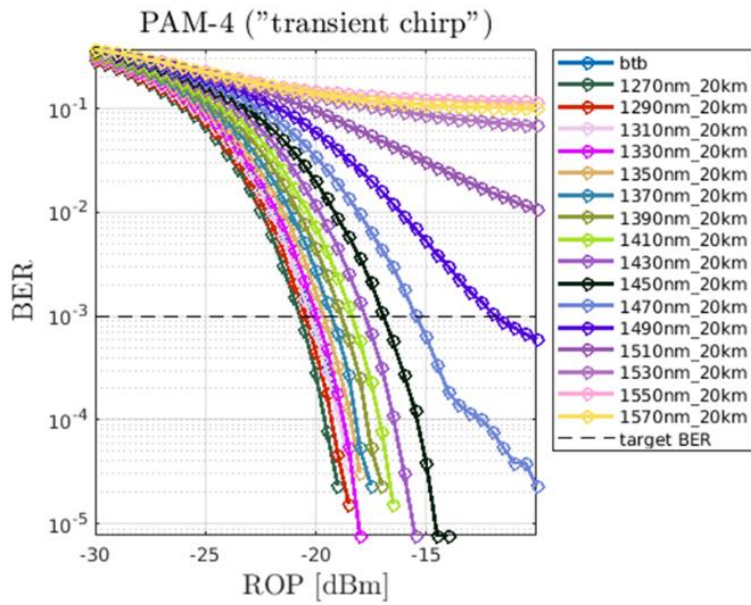


Figure 3.12. BER versus ROP curves for 25Gbps PAM-4 transmission using DML (only transient chirp) for different wavelength values over 20km of fiber. Adaptive equalization at RX is used (FFE-14).

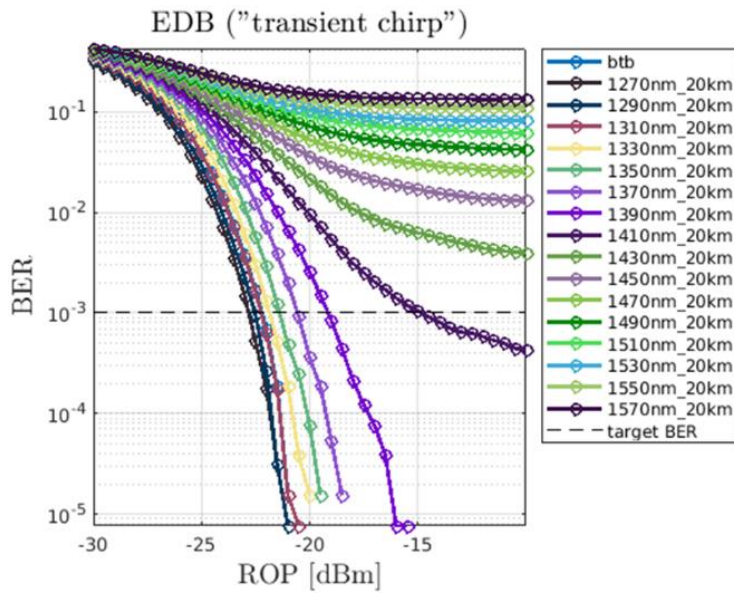


Figure 3.13. BER versus ROP curves for 25Gbps EDB transmission using DML (only transient chirp) for different wavelength values over 20km of fiber. Adaptive equalization at RX is used (FFE-14).

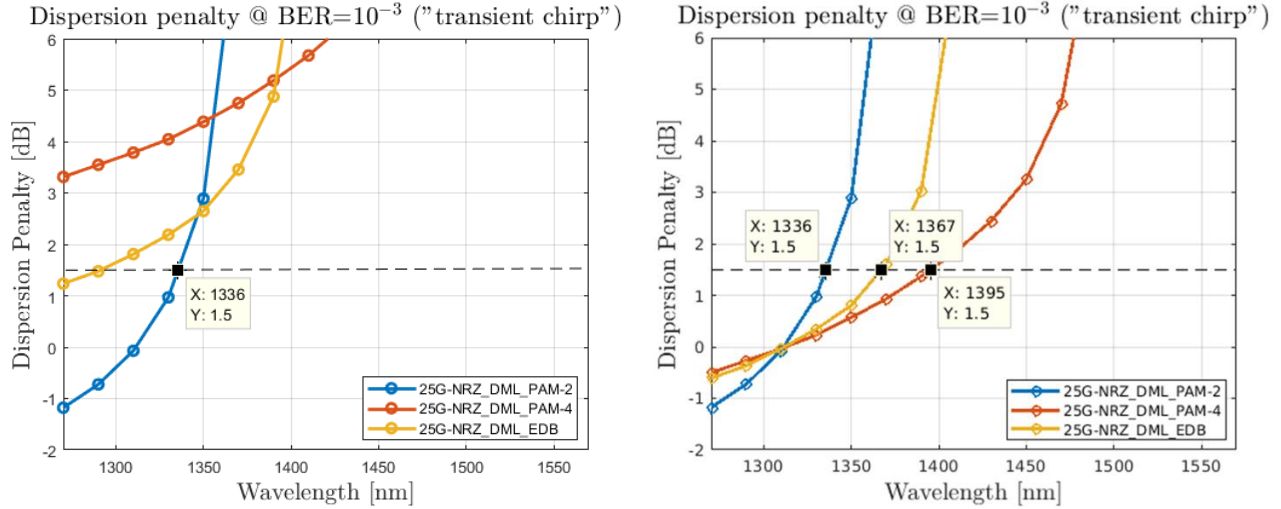


Figure 3.14. Dispersion penalty curves as a function of wavelength for 25 Gbps transmission over 20km of fiber: the penalty values for different modulation formats can be either computed with respect to a unique reference value (plot on the left; the back-to-back sensitivity of the PAM-2 case is used as reference) or with respect to different reference values, one for each format (plot on the right).

In Figure 3.14 the dispersion penalty curves for each modulation format are computed in two ways:

- with respect to a unique reference value, chosen equal to the back-to-back sensitivity of the PAM-2 case (left plot in Figure 3.14). In this case, the curves clearly show that, for wavelength values $\lambda < 1350 \text{ nm}$, the modulation format which guarantees lowest penalties is PAM-2. Nevertheless, as the wavelength increases further, the other formats, being more resilient to chromatic dispersion, perform better: EDB proves to be the best format when $1350 \text{ nm} \leq \lambda \leq 1390 \text{ nm}$, while, for $\lambda > 1390 \text{ nm}$, the best choice is PAM-4.
- by referring the penalty to different references, chosen equal to the back-to-back sensitivities of each format (right plot in Figure 3.14). In other words, the penalty contribution due to the adoption of different formats is neglected: all of the curves intersect in correspondence of the zero-dispersion wavelength $\lambda_{ZD} \approx 1310 \text{ nm}$. This kind of operation allows to highlight the tolerance of each format to chromatic dispersion. We'll always adopt this approach in the following of this Chapter. From the right plot of Figure 3.14 we understand that, for the considered system affected by transient chirp, the modulation format which enables the longest reach is PAM-4, followed by EDB and PAM-2.

We should point out that a more realistic analysis should also take into account the adiabatic chirp component, as we will do in the following.

3.4 The separated effect of adiabatic chirp

In the following subsections we firstly expose some theoretical concepts about the adiabatic chirp component (Section 3.4.1), then we present some simulation results aiming both at validating our model (Section 3.4.2) and at studying more deeply the performance of a DML/DD system (Section 3.4.3) in which the only source of chirp is the adiabatic one. We preliminarily point out that, while the transient chirp component (analyzed in Section 3.3) has been widely studied in the literature, there are relatively few works about the adiabatic chirp component and even less involving the complete chirp expression (which will be the subject of Section 3.5).

3.4.1 Interplay between adiabatic chirp and dispersion

The adiabatic chirp component turns out to have a very simple expression: the frequency deviation is just proportional to the intensity of the optical pulse at the output of the DML according to:

$$\Delta\nu_{ad}(t) = \frac{\alpha}{4\pi} k \cdot P(t) \quad (3.3)$$

This implies that, in the travelling pulse, points (on the leading and trailing edges) corresponding to the same power level will have the same frequency shift (both in sign and amplitude) and thus experience the same group velocity. Moreover, different power levels will experience different group velocities. The final effect at fiber output is a distortion of the pulse, which happens to present a certain degree of asymmetry (high intensity spikes on leading or trailing edge due to the so-called “self-steepening effect” described in [29]) depending on the actual power values and on the sign of dispersion. A properly designed feed-forward equalizer (FFE) placed at receiver side is able to partially recover from this kind of impairments, but only up to a given distortion level [27]. In the eye diagram, the adiabatic chirp also manifests a time skew effect, which is very evident in PAM-4, as shown in [26].

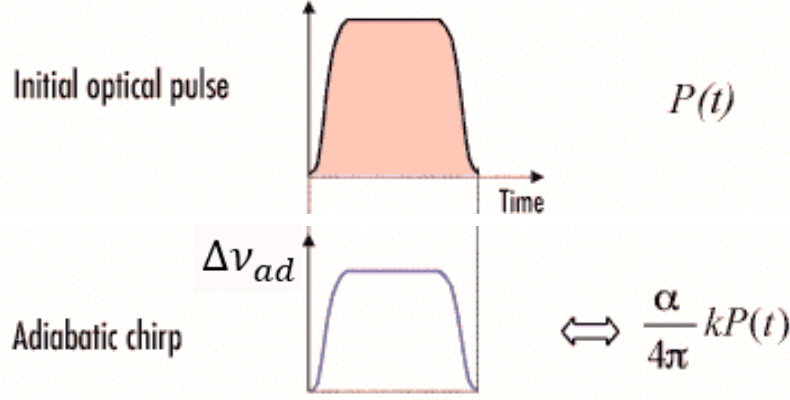


Figure 3.15. Graphical representation of the temporal evolution of the adiabatic chirp frequency deviation Δv_{ad} , along with its mathematical expression. Image taken from [28].

3.4.2 Chirp/dispersion effect on eye diagram: simulation setup

We now simulate a hypothetical system in which only the adiabatic chirp component is present. This approach will help us in understanding more deeply how the interaction between the adiabatic chirp and chromatic dispersion distort the received eye diagram: the so-called “skew” effect. We try to visualize the latter in the case of a PAM-4 transmitted signal, i.e. a signal presenting 4 different power levels which will thus give rise to 4 different optical frequencies:

$$v_i = v_0 + v_{ad}(P_i), \quad 1 \leq i \leq 4 \quad (3.4)$$

where the index i denotes the i -th level, v_0 is the original (chirp-less) central frequency and $v_{ad}(P_i)$ is the adiabatic term of the instantaneous frequency deviation associated to the power level P_i according to Eq. 3.3. The main simulation parameters and a scheme of the system setup are provided respectively in Table 3.3 and Figure 3.16.

R_b	Format	$P_{DML,out}$	ER	L	TX f_{3dB}	RX f_{3dB}	APD gain	R	α
25 Gbps	PAM-2	5 dBm	20 dB	20 km	25 GHz ($B_{3dB} = 100\%$)	25 GHz ($B_{3dB} = 100\%$)	12	0.85 A/W	3.5

Table 3.3. Main simulation parameters used for the adiabatic chirp model validation.

It's worth noticing that relatively high values for ER (20 dB) and output power from DML (5 dBm) have been chosen intentionally in order to enhance the effect of adiabatic chirp. Indeed, we've seen that this kind of chirp is proportional to power and, moreover, a higher extinction ratio (which emphasizes the separation between the levels of the signal) leads to a higher differential frequency deviation between levels. Moreover, very large filters have been used so as to minimize the linear distortion that bandwidth limitation could introduce (which was matter of interest in Chapter 2): we are only interested in the pulse distortion introduced by the chirp/dispersion interplay.

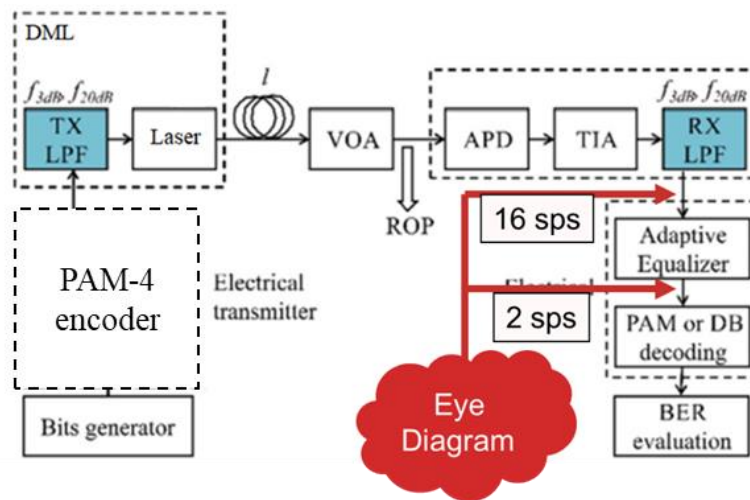


Figure 3.16. Block scheme of the simulated system used for studying the adiabatic-chirp-induced time skew effect. The point at which the eye diagram is measured are shown, along with the information about the number of samples per symbol used.

The eye diagram is measured at receiver side both before and after the adaptive equalizer for several different chirp and dispersion parameters.

3.4.2.1 Back-to-back case

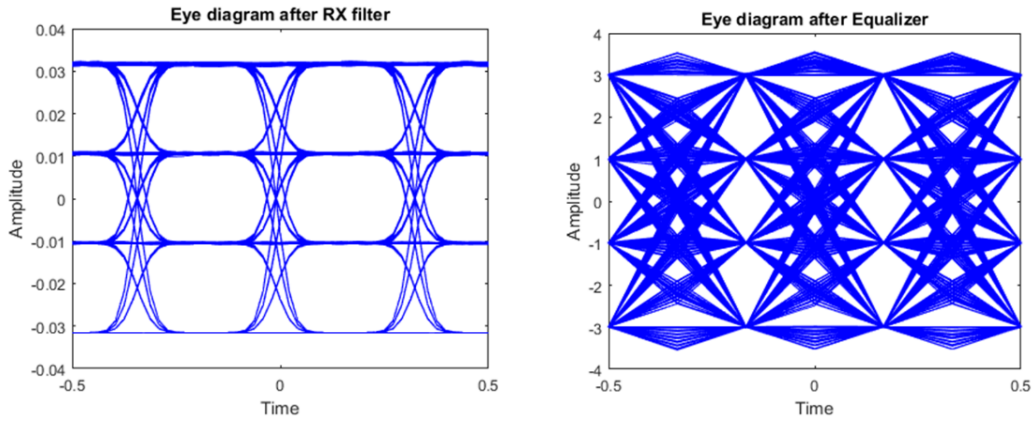


Figure 3.17. Received eye diagrams before and after equalization in the back-to-back case for a 25 Gbps PAM-4 transmission @ 1270 nm ($D = -5$ ps/nm/km).

Just as a reference, we firstly consider the simplest scenario in which dispersion is absent ($L = 0$ km, so that accumulated dispersion $D \cdot L$ is null, too). We get very clean eye diagrams, due to the high received power and practically absent filter distortion, both before and after equalization (plots in Figure 3.17). We can use them for comparison in the following of our analysis. It's worth to point out that the value of the chirp parameters k and α is irrelevant in this case.

3.4.2.2 Dispersion without chirp case

We proceed by gradually introducing new sources of impairments. In particular, we here introduce chromatic dispersion by considering, as transmissive medium, a 20 km long SSMF operated at $\lambda = 1270$ nm ($D = -5$ ps/nm/km). The chirp is switched off ($\alpha = 0$, $k = 0$) in our model. What results from the eye diagram before equalization is just a slight distortion caused by chromatic dispersion (plots in Figure 3.18).

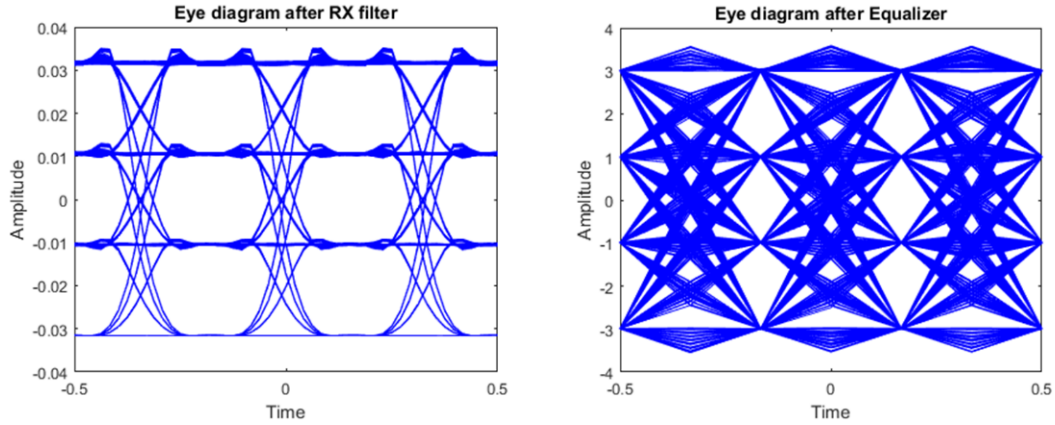


Figure 3.18. Received eye diagrams before and after equalization in absence of chirp (but in dispersion) for a 25 Gbps PAM-4 transmission @ 1270 nm ($D=-5$ ps/nm/km) over 20km of SSMF.

3.4.2.3 Negative dispersion case

We finally include in the simulation the adiabatic chirp according to the above developed model. The transmissive media is still a 20 km long SSMF operated at $\lambda = 1270$ nm ($D = -5$ ps/nm/km) but now the adiabatic chirp is enabled. In particular, $\alpha = 3.5$ and $k = 28.7 \cdot 10^{12}$. These values, that will be also used in the following pages, have been extracted from the literature (reference [30]) and represent realistic values for commercial DFB lasers.

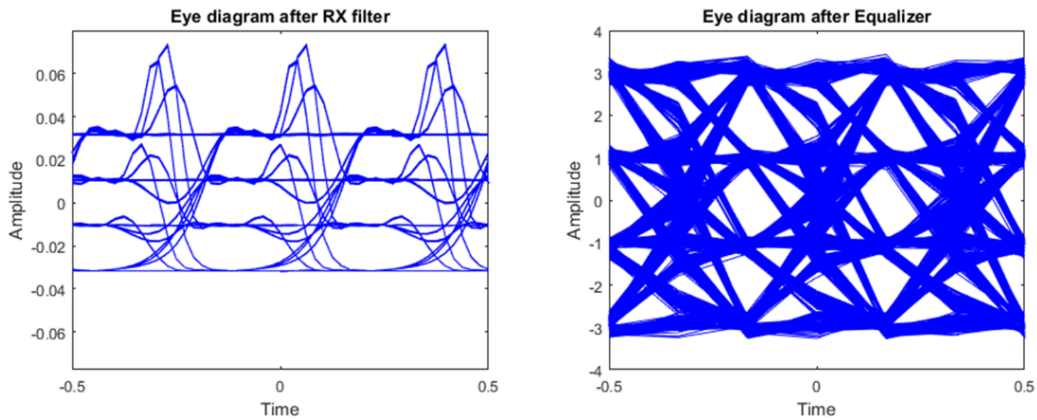


Figure 3.19. Received eye diagrams before and after equalization in presence of chirp ($\alpha = 3.5$, $k = 28.7 \cdot 10^{12}$) and negative dispersion for a 25 Gbps PAM-4 transmission @ 1270 nm ($D=-5$ ps/nm/km) over 20km of SSMF.

What emerges from the eye diagram before equalization (Figure 3.19 on the left) is the typical asymmetric pulse distortion that we described in 3.4.1. High intensity spikes are clearly visible on the trailing edges and an evident

skew toward the right is present. The reason for the latter can be found in the negative dispersion parameter sign. Indeed, in this framework, the lower frequency components (i.e. the higher wavelength ones) travel faster along the fiber than higher frequency ones (i.e. the lower wavelength ones), according to the well-known formula for differential group delay:

$$\Delta\tau_g = D \cdot l \cdot \Delta\lambda < 0, \quad @ \lambda = 1270 \text{ nm} \quad (3.5)$$

For this reason, the lower levels, being located at lower frequencies due to adiabatic chirp (Eq. 3.3), arrive earlier than upper levels. The entity of the skew is quite high, and the equalizer can only partially compensate for it (Figure 3.19 on the right).

3.4.2.4 Positive dispersion case

Ultimately, we investigate what happens when the sign of dispersion changes. With this purpose in mind we repeat the simulation seen in 3.4.2.3 but changing the operative wavelength to $\lambda = 1370 \text{ nm}$, such that $D = 5 \text{ ps/nm/km}$. Intuitively, before equalization (Figure 3.20 on the left) the high intensity spikes (self-steepening effect) are now on the leading edges and the direction of the skewing effect is changed. Indeed, in this framework, being $\Delta\tau_g > 0$, the higher frequency components (i.e. the lower wavelength ones) travel faster than lower frequency ones (i.e. the higher wavelength ones), resulting in an early arrival for the upper levels w.r.t. lower ones (eye diagram is tilted toward the left) Again, equalization partially compensates for the impairment (Figure 3.20 on the right).

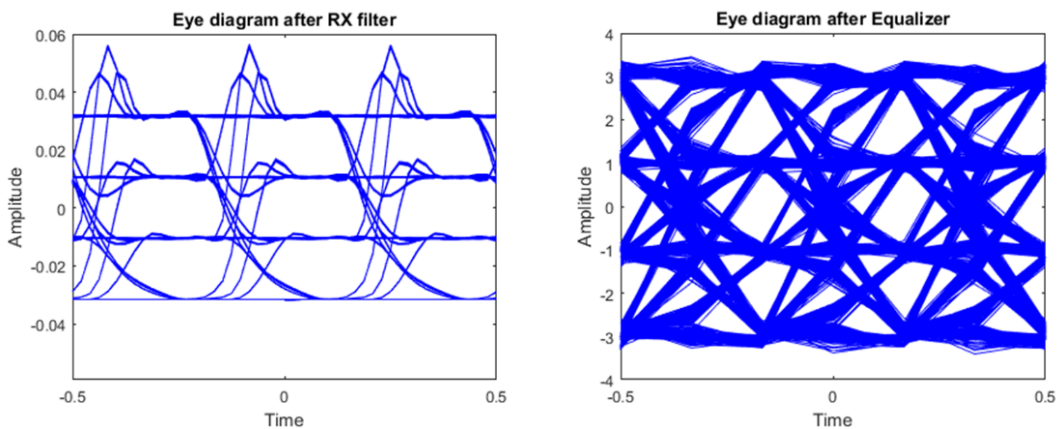


Figure 3.20. Received eye diagrams before and after equalization in presence of chirp ($\alpha = 3.5$, $k = 28.7 \cdot 10^{12}$) and positive dispersion for a 25 Gbps PAM-4 transmission @ 1370 nm ($D=5 \text{ ps/nm/km}$) over 20km of SSMF.

3.4.3 DML and adiabatic chirp: effect on different formats

We now resume our study of the penalty versus wavelength for different modulation formats (PAM-2, PAM-4 and EDB). We fix the same scenario as Section 3.3.3 (25 Gbps transmission but with no bandwidth limitations neither at transmitter nor at receiver, utilizing 14-taps FFE) but now we assume that the only contribution to chirp is the adiabatic one. Nevertheless, we should point out that, due to the power dependency of the adiabatic chirp term, the performance strongly depends on the average power P_{tx} at the output of the DML. For this reason, we analyze the system for three different values of output power: respectively 7 dBm, 9 dBm and 11 dBm¹⁰. Moreover, we repeat the simulations twice, for two different values of adiabatic chirp coefficient k (see Table 3.4), so as to consider both a DML-A and a DML-T. We denote the two cases respectively as “adiabatic-1” (higher k) and “adiabatic-2” (lower k).

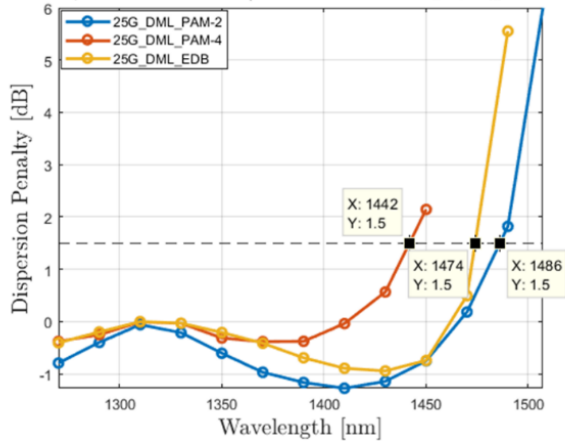
«Adiabatic-1» case (DML-A)	«Adiabatic-2» case (DML-T)
$k = k_1 = 28.7 \cdot 10^{12} \text{ Hz/W}$ $\alpha = 3.5$	$k = k_2 = 1.5 \cdot 10^{12} \text{ Hz/W}$ $\alpha = 3.5$

Table 3.4. Chirp parameters (linewidth enhancement factor α and adiabatic chirp coefficient k) adopted in the adiabatic-chirp-only simulations. The values of k are drawn from the literature [25, 30] for the DML-A and DML-T cases.

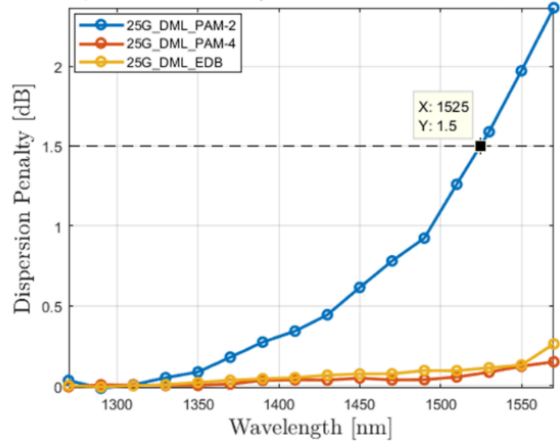
Differently from 3.3.3, we here omit for simplicity the BER versus ROP curves. Instead, we directly report the plots of penalty versus wavelength, in which the performances of the three modulation formats can be easily compared for the three different values of P_{tx} (plots in Figure 3.21).

¹⁰ These three values of output power from DML have been chosen in agreement with the values provided by the NG-PON2 standard, which assumes higher power at the transmitter compared to previous standards.

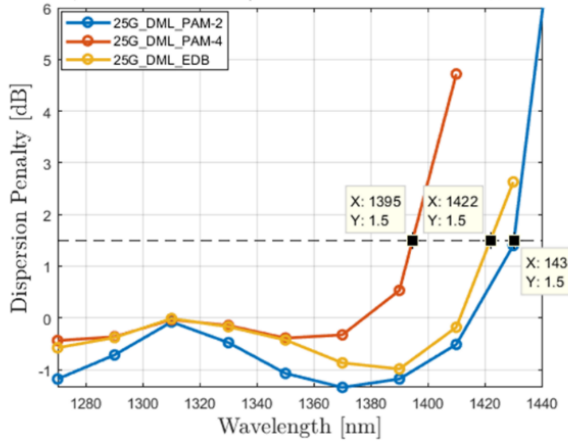
Penalty @ BER= 10^{-3} ("Adiabatic-1 chirp", $P_{tx}=7\text{dBm}$)



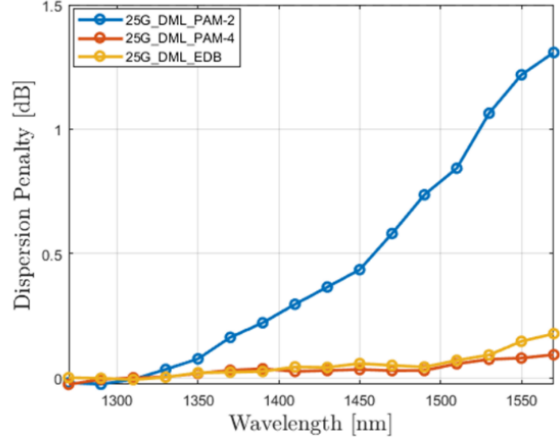
Penalty @ BER= 10^{-3} ("Adiabatic-2 chirp", $P_{tx}=7\text{dBm}$)



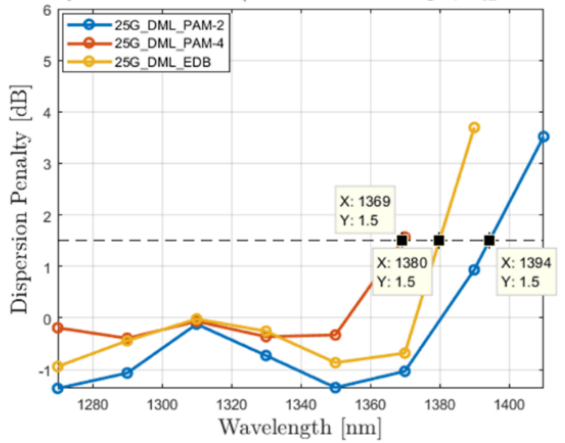
Penalty @ BER= 10^{-3} ("Adiabatic-1 chirp", $P_{tx}=9\text{dBm}$)



Penalty @ BER= 10^{-3} ("Adiabatic-2 chirp", $P_{tx}=9\text{dBm}$)



Penalty @ BER= 10^{-3} ("Adiabatic-1 chirp", $P_{tx}=11\text{dBm}$)



Penalty @ BER= 10^{-3} ("Adiabatic-2 chirp", $P_{tx}=11\text{dBm}$)

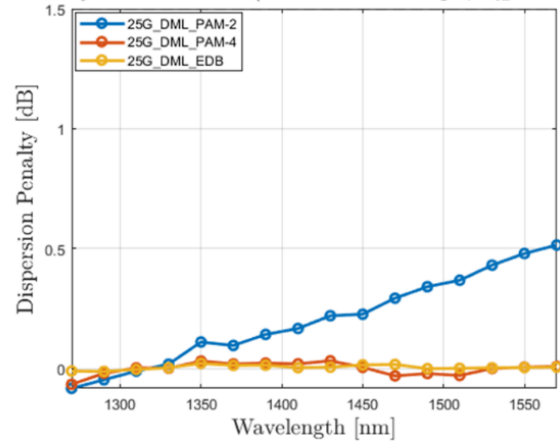


Figure 3.21. Plots of dispersion penalty curves as a function of wavelength for 25 Gbps transmission over 20 km of fiber. Only the adiabatic chirp term is taken into account, with two different values of adiabatic chirp coefficient k : one for DML-A (denoted as "Adiabatic-1 chirp", in the left column), the other for DML-T ("Adiabatic-2 chirp", in the right column). To highlight the power dependence of adiabatic chirp, three values of output power from DML are considered (7 dBm, 9 dBm and 11 dBm).

Depending upon the type of DML used (whether transient or adiabatic dominated), the impact of the adiabatic chirp term on the performance may be extremely different. We can qualitatively describe the two different behaviors as follows.

For the DML-A, i.e. for higher adiabatic chirp (plots on the left in Figure 3.21):

- for a fixed P_{tx} and for any of the modulation formats, the power penalty w.r.t. the back-to-back case does not exhibit a monotonic behavior versus wavelength (and thus versus accumulated dispersion), as it was for the “transient chirp only” case. Instead, it presents a local maximum, then it goes down to a local minimum and finally it starts increasing. For certain ranges of wavelength, we can surprisingly notice an advantage w.r.t. the back-to-back case. The reason, historically (and erroneously) attributed to the already cited self-steepening effect, will be explained in detail in 3.5.1;
- as the output power from DML increases, the dispersion tolerance of the system decreases: in other words, for any modulation format, the reference penalty value of 1.5 dB is reached at smaller wavelength values. This also means that the higher is P_{tx} , the smaller is the system reach;
- for any of the considered values for P_{tx} , the modulation format allowing for the highest wavelengths (or, analogously, the longest distances) is PAM-2, followed by EDB and finally PAM-4.

On the other hand, for the DML-T, i.e. for lower adiabatic chirp (plots on the right in Figure 3.21):

- for a fixed P_{tx} and for any of the modulation formats, the power penalty w.r.t. the back-to-back case exhibits a monotonically increasing behavior versus wavelength (and thus versus accumulated dispersion), as it was for the “transient chirp only” case. Nevertheless, the performances of the systems using PAM-4 and EDB seem to be very tolerant to accumulated dispersion: the penalty is negligible even in C-band. Contrarily, the PAM-2 performs significantly worse (but still much better than in the DML-A case);
- as the output power from DML increases, the dispersion tolerance of the system surprisingly improves: for any modulation format, the reference penalty value of 1.5 dB is reached at higher wavelength values. This also means that the higher is P_{tx} , the longer is the system reach. This is again connected to the non-trivial interplay between adiabatic chirp and dispersion.

- for any of the considered values for P_{tx} , the modulation format allowing for the highest wavelengths (or, analogously, the longest distances) is PAM-4, almost equal merit with EDB, finally followed by PAM-2. Though, we should take into account that these penalties are computed with respect to different references for the three modulation formats. For this reason, we should be careful when claiming the superiority of a format over another.

The analysis is interesting, but still incomplete, since we're still considering just one of the chirp contributions. We'll further extend our analysis in Section 3.5.

3.5 The effect of the full chirp

In the following Sections we firstly review a frequency domain interpretation of the chirp/dispersion interaction (Section 3.5.1), then we present some simulations results aiming both at validating our model (Section 3.5.2) and at studying more deeply the performance of a realistic DML/DD system (Section 3.5.3).

3.5.1 Interplay between full chirp and dispersion

As explained above, the separated effects of the two main chirp components on non-dispersion compensated transmission have been studied in the literature and can be easily understood in time domain. What's less intuitive is how the simultaneous presence of both chirps can influence the performance of an optical transmission system.

An exhaustive answer to this question is given in [27, 31] and involves a small signal frequency domain analysis of the DML/DD system. Whenever DML is used together with a dispersive fiber, it is shown in [27, 31] that the frequency response of the latter takes the expression:

$$H_F(\omega) = \sqrt{1 + \alpha^2} \cos(\theta + \tan^{-1} \alpha) + j \frac{\alpha \kappa P_0}{\omega} \sin \theta, \quad (3.6)$$

$$\text{in which } \theta = D\lambda^2\omega^2L/(4\pi c),$$

where P_0 is the output power from DML, ω is the angular frequency of the modulated signal, c is the speed of light in vacuum and L is the fiber length. The real part of $H_F(\omega)$ accounts for the transient chirp (indeed it includes the linewidth enhancement factor α), while the imaginary one derives from the adiabatic chirp (indeed it includes the factor $\alpha \cdot \kappa \cdot P_0$). It's clear that the shape of the amplitude transfer function depends on the

particular value of distance L under analysis (and thus on accumulated dispersion $D \cdot L$). Figure 3.22 illustrates the module of $H_F(f)$ for several values of distance in the case in which $\alpha = 3.5$, $k = 13 \cdot 10^{12} \text{Hz/W}$, $P_0 = 7 \text{dBm}$ and $\lambda = 1550 \text{ nm}$ ($D = 17 \frac{\text{ps}}{\text{nm} \cdot \text{km}}$).

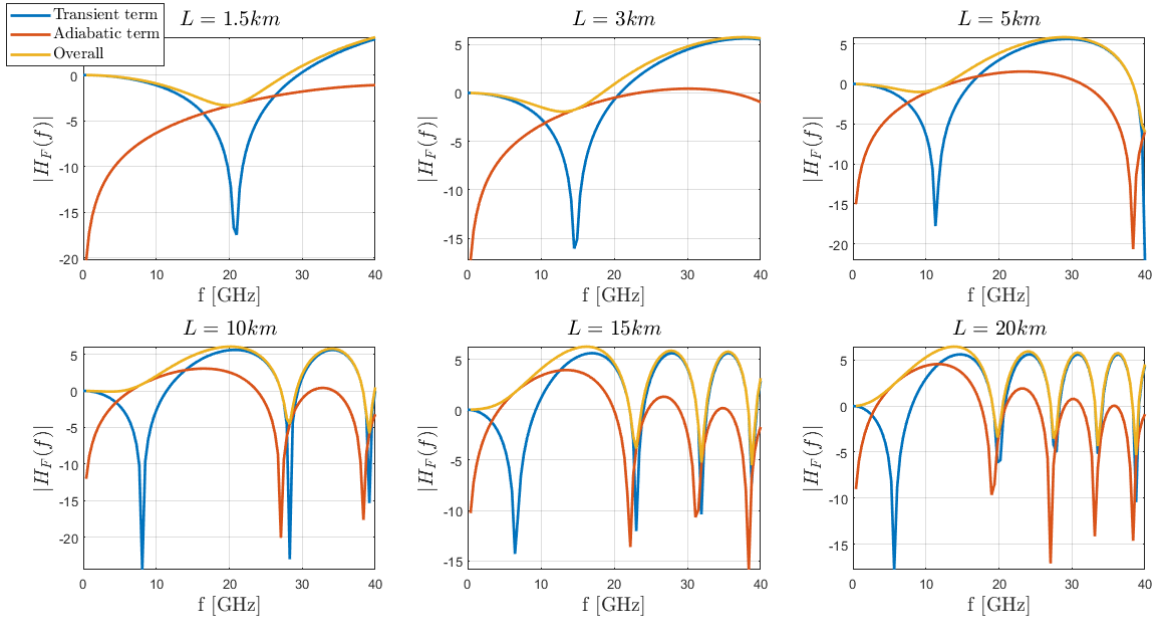


Figure 3.22. Amplitude transfer function of the dispersive fiber in a DML/DD system ($\alpha = 3.5$, $k = 13 \cdot 10^{12} \text{Hz/W}$), according to the theoretical formula. The effect of transient and adiabatic chirp are also shown separately.

For each considered distance, the figure also reports separately the transient and adiabatic chirp components of Eq. 3.6. In particular, it can be noticed that, for small distances, the transient chirp term tends to force the fiber to behave like a low-pass filter (e.g. for $L=1.5 \text{ km}$ a notch at 21 GHz is visible). Simultaneously, the adiabatic chirp term adopts a high-pass filter behavior, whose effect on the overall fiber transfer function is a compensation (a flattening of the frequency response) for the notch introduced by transient chirp. Anyway, as fiber length increases, both the adiabatic and the transient terms introduce new frequency dips at higher frequencies, which, being located approximately at the same positions, remain uncompensated. Moreover, the notches tend to move to lower and lower frequencies (and thus, sooner or later, irredeemably enter the useful bandwidth of the system) as the distance increases. Consequently, the system performance change accordingly: whenever increasing the distance results in a higher available bandwidth, we should expect an improvement in the sensitivity, i.e. less required received optical power for achieving a target BER. This happens, in Figure 3.22,

when passing from 3km to 5km fiber length. On the other hand, whenever increasing the distance results in a lower available bandwidth, we should expect a worsening in the sensitivity. This happens, in Figure 3.22, when passing from 5 km to any longer distance. This peculiar behavior of sensitivity versus dispersion will be highlighted by simulations in the following pages.

The module of $H_F(f)$ for different fiber length values is also reported for a transient-dominated laser (DML-T) in Figure 3.23. Basically, all of the parameters of Figure 3.22 are kept fixed except for the adiabatic chirp coefficient, which is now set to $k = 1.5 \cdot 10^{12} \text{ Hz/W}$.

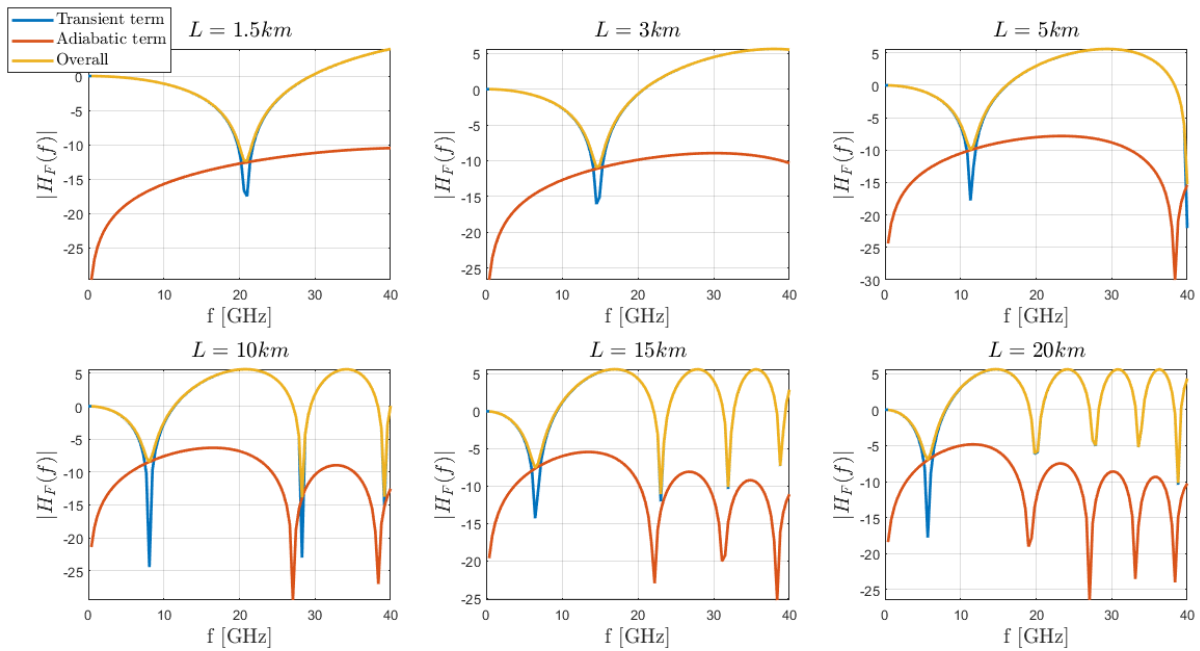


Figure 3.23. Amplitude transfer function of the dispersive fiber in a DML-T/DD system ($\alpha = 3.5$, $k = 1.5 \cdot 10^{12} \text{ Hz/W}$), according to the theoretical formula. The effect of transient and adiabatic chirp are also shown separately.

The position of the notches remains the same, despite the change in the adiabatic chirp coefficient. Anyway, for a DML-T, the adiabatic component of the frequency response is not able to effectively compensate the first notch introduced by transient chirp. Consequently, the DML-T/DD system will be strongly bandlimited by the transient chirp. A way to solve this bandwidth issue, is operating a DML-T with high output power P_0 , so as to increase the product $k \cdot P_0$ and drive the DML behavior from transient to adiabatic (Eq. 3.1).

Eventually, in adiabatic conditions, as pointed out in [27], the available bandwidth of the dispersive fiber can be roughly identified with the first notch frequency of the adiabatic term (i.e. the second notch of the transient term), whose approximated expression is [27]:

$$B_F \approx f_{notch,1,ad} \approx \sqrt{\frac{c}{D\lambda^2 L}} \quad (3.7)$$

which is, in a first approximation, independent on the laser chirp parameters α and k . Of course, the overall (small signal electrical-to-electrical) frequency response of the DML/DD system will be determined by the limited bandwidths of DML and receiver photodetector.

3.5.2 Full chirp model validation

As a final step in the validation phase of our model, we now consider the case in which both chirp components are present. With this purpose in mind, we take as a reference the experimental results reported in [31] and utilize our simulative approach in order to replicate them. The goal is to compute the sensitivity (defined at $BER = 10^{-3}$) versus ROP for different fiber lengths (and thus different accumulated dispersion values). The focus is on 28 Gbps¹¹ transmissions using PAM-4 and EDB formats in a DML/DD system affected by chirp and with bandwidth limitations only at receiver side (PIN photodetector). The main simulation parameters, most of which have been extracted from the reference paper, are reported in Table 3.5.

R_b	28 Gbps	ER [dB]	For PAM4 : 2.2 For EDB : 1.5
λ [nm]	1549	L [km]	{0, 5, 10, 20, 30, 40, 50}
D [ps/nm/km]	17.5	R [A/W]	0.8
α	3.2	G (gain of pin)	1
k [Hz/W]	$13 \cdot 10^{12}$ (DML-A)	F [dB]	10.5
$f_{3dB,DML}$ [GHz]	24.2	$f_{3dB,pin}$ [GHz]	7.5
$f_{20dB,DML}$ [GHz]	38	$f_{20dB,pin}$ [GHz]	14
$P_{tx,DML}$ [dBm]	7.4		

Table 3.5. Main parameters for the DML/DD simulated system (full chirp expression is used), drawn from [31]

¹¹ This value of bitrate, used to replicate the results of [30], has to be intended as a raw bitrate finalized to a 25 Gbps net bitrate. It takes into account all the possible transmission overheads.

We should preliminarily point out that our simulation setup presents several small differences with respect to the experiment:

- the actual measured shapes of the electrical frequency responses of DML and PIN receiver (reported in the reference paper) have been emulated in our simulations using Super Gaussian filters with the same filtering characteristics (f_{3dB} and f_{20dB}) as the measured ones have been used.
- a slightly different equalizer has been used: a 20-tap FFE, against the better-performing but more complex 17-tap FFE + 7-tap DFE deployed in the experiment. Because of that, we should probably expect, in our simulation, worse sensitivity values (i.e. higher required power for target BER) than the experimental ones.
- the IRND parameter was not provided in the reference text, so we properly chose it “empirically”, so as to fit the value of sensitivity at $BER = 10^{-3}$ with the experimental one, in the case of PAM-4 modulation format.

All of these points are possible causes of discrepancies in our results. The latter are reported in Figure 3.24 and Figure 3.25, together with the reference experimental curves, for the PAM-4 format, as well as for EDB.

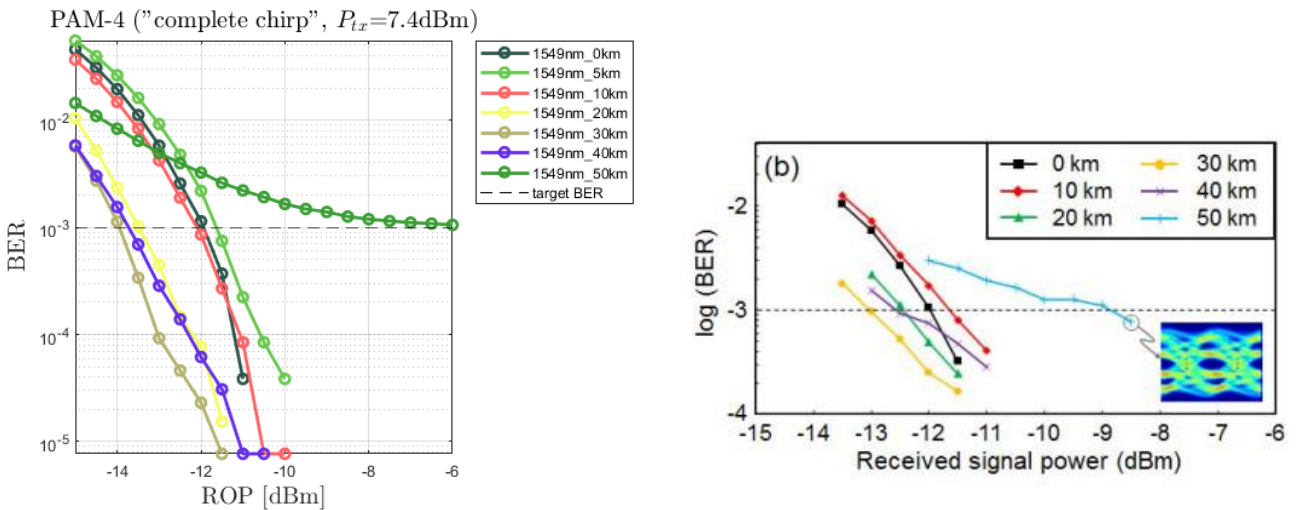


Figure 3.24. Simulated (on the left) and experimental (on the right, from reference [31]) BER versus ROP curves for different fiber lengths in the case of PAM-4 transmission. The main simulation parameters are in Table 3.5.

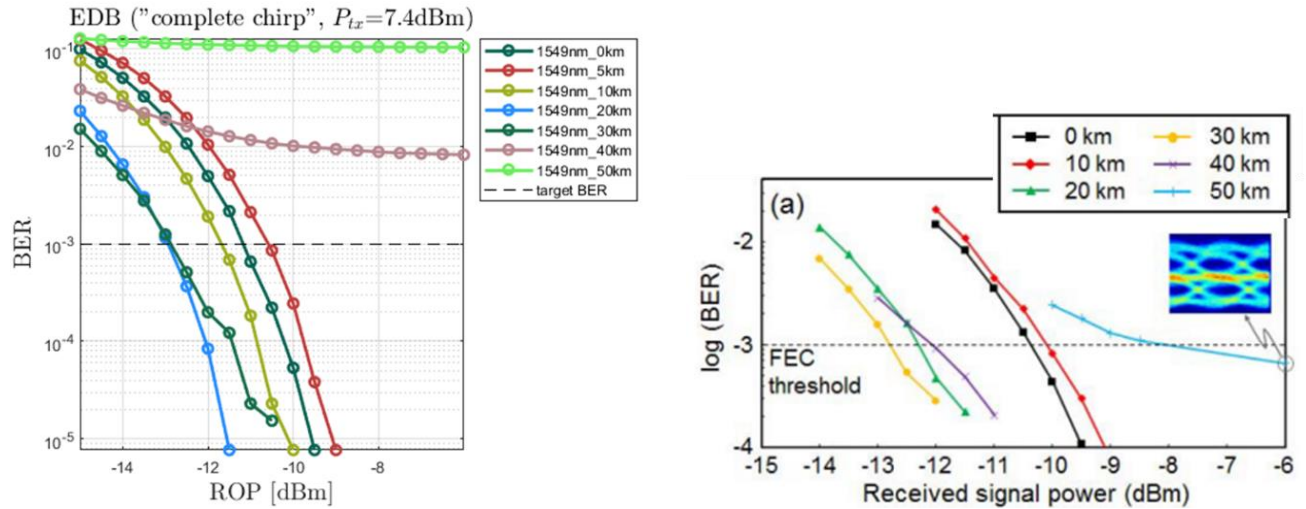


Figure 3.25. Simulated (on the left) and experimental (on the right, from reference [31]) BER versus ROP curves for different fiber lengths in the case of EDB transmission. The main simulation parameters are in Table 3.5.

Regardless of which of the two modulation formats we consider, it's straightforward to remark some important agreements between simulation and experimental results:

- the qualitative trend according to which performance decrease (BER curves moving toward the right as fiber length grows) up to a given distance, then suddenly increase (BER curves moving to the left) and finally decrease again is preserved. This is due to the interplay between chirp and chromatic dispersion, that we're now able to explain by recalling the theoretical analysis presented in Section 3.5.1. In few words, the back-to-back performance is only limited by the bandwidths of the transceivers. The initial performance worsening, instead, is caused by transient chirp, which, operating like a low-pass filter, introduces a frequency notch in the dispersive fiber transfer function. Then, as the distance increases further, the adiabatic chirp component comes into play, compensating for the first transient frequency notch (the frequency response gets flattened) and also boosting the frequency response for higher frequencies. This latter effect, compensating for the bandwidth limitations of transceivers, enables sensitivity values which are better than the back-to-back ones. As distance grows further, performance degrades again, due to the successive chirp-induced frequency notches limiting the bandwidth of the DML/DD system, leading to the out of service (error floor);
- best performance is at a distance around 30 km;

- PAM-4 slightly outperforms EDB. This can be attributed to the higher extinction ratio used for the former (2.2 dB compared to 1.5 dB).

Mainly due to the above described differences between the simulation and experimental setups, also some disagreements can be observed:

- the local maximum in the sensitivity is at different values of length: 5 km and 10 km respectively for simulation and experiment;
- the penalty values for high distances are much higher in the simulated results than in the experimental ones. This is strongly related to the different equalization methods.

The comparison between PAM-4 and EDB in this scenario is better summarized in the plots of Figure 3.26, in which, for each value of distance, the power penalty w.r.t. the back-to-back case is reported.

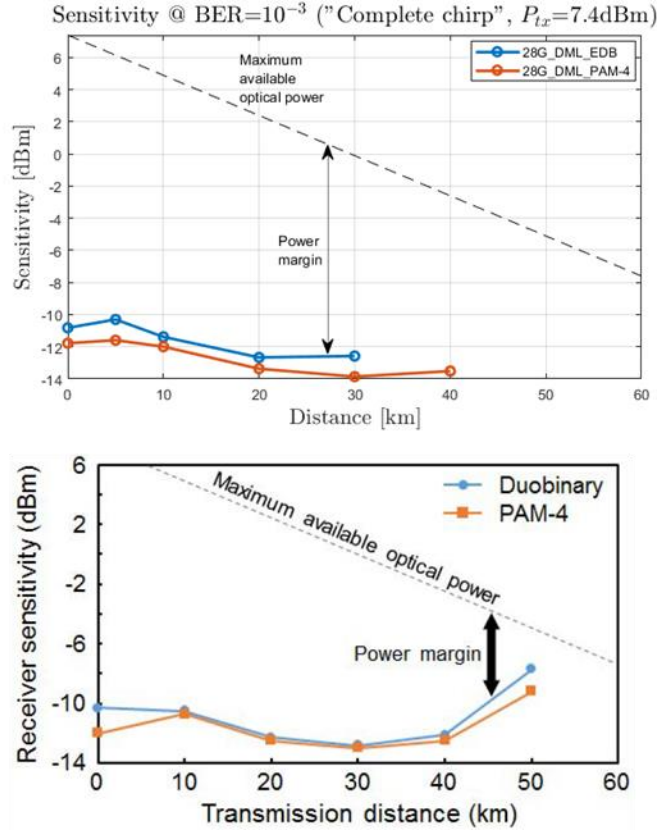


Figure 3.26. Plots of power penalty (w.r.t. back-to-back sensitivity) versus distance for PAM-4 and EDB. The simulated results (upper plot) presents agreements as well as disagreements (explained in detail in the text) with the experimental ones from reference [31] (lower plot). The main simulation parameters are in Table 3.5.

3.5.3 DML and full chirp: effect on different formats

We now get back to our study of the penalty versus wavelength for different modulation formats (PAM-2, PAM-4 and EDB). We fix the same scenario as Section 3.4.3 (25 Gbps transmission but with no bandwidth limitations neither at transmitter nor at receiver, utilizing 14-taps FFE) but now we include the full chirp expression. All of the considerations about adiabatic chirp made in Section 3.4.3 still hold.

Once again, we report the plots of penalty versus wavelength, for three different values of P_{tx} and two kinds of DMLs (Figure 3.27). The laser chirp parameters corresponding to the two systems labeled as “Complete-model 1” and “Complete-model 2” are reported in Table 3.6.

«Complete-model 1» case (DML-A)	«Complete-model 2» case (DML-T)
$k = k_1 = 28.7 \cdot 10^{12}$ Hz/W $\alpha = 3.5$	$k = k_2 = 1.5 \cdot 10^{12}$ Hz/W $\alpha = 3.5$

Table 3.6. Chirp parameters adopted in the complete-model chirp simulations. The values of k are drawn from the literature [25, 30] for the DML-A and DML-T cases.

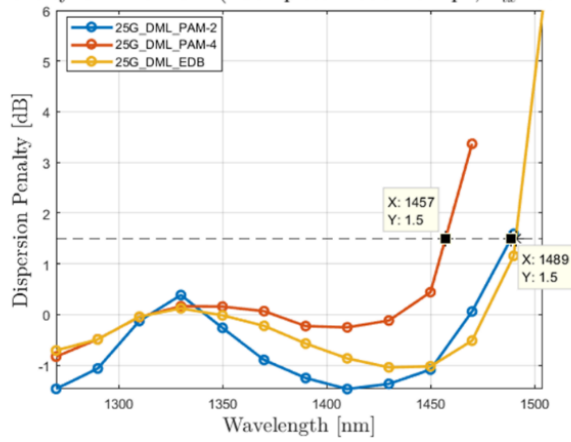
The results are easily justified based on the results of Sections 3.3.3, 3.4.3 and the theoretical notions introduced in Section 3.5.1.

For the DML-A (plots on the left in Figure 3.27), it happens that, due to the large k value, the transient chirp contribution to total chirp becomes negligible w.r.t. the adiabatic one, which dominates. For this reason, the plots follow very closely the same non-monotonical behavior as the one observed for DML-A in Section 3.4.3. Moreover, again, as the output power from DML increases, the dispersion tolerance of the system decreases. The modulation format allowing for the highest wavelengths (or, analogously, the longest distances) is PAM-2, followed by EDB and finally PAM-4.

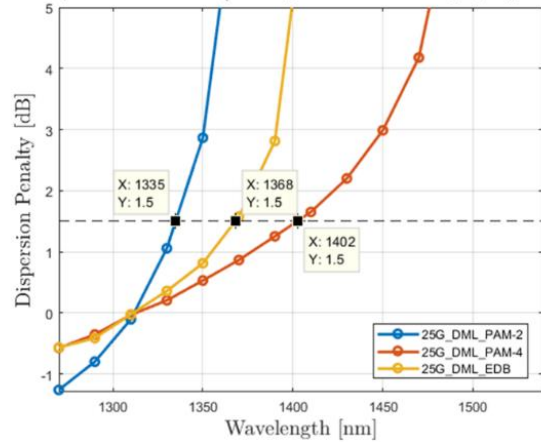
For the DML-T (plots on the right in Figure 3.27), instead, the behavior is quite peculiar. For 7 dBm output power from DML, it's clear that the dominant contribution to total chirp is the transient one. Indeed, the corresponding plot (upper-right corner of Figure 3.27) is very similar to the one observed for the “only-transient” case in 3.3.3. Anyway, the presence of the adiabatic chirp component introduces a power dependency in the system performance. As P_{tx} increases to 9 dB and then to 11 dBm, the behavior of the system turns gradually from transient to adiabatic: a local maximum and a local minimum in the penalty versus wavelength plot appear. This happens despite of the relatively small value of k : indeed, what actually matters is the product $k \cdot P_{tx}$. Moreover, as the output power from DML increases, it happens that the dispersion tolerance of the system improves: due to the presence of the local minimum in penalty, some new ranges of wavelength become feasible (i.e. transmission becomes possible, with an acceptable limited penalty). This result is particularly interesting, since it opens to the possibility, even in the case of DML-T, of exploiting C-band by simply tuning properly the power and, as we'll see in Section 3.6, the extinction ratio. It's also worth to notice that, a larger than usual penalty in C-band could potentially be accepted thanks to the reduced fiber attenuation, which saves some dBs in the loss budget. Finally, we remark that, for DML-T, the choice of the most suitable modulation

format depends on the particular wavelength window we wish to operate in. As an example, the best option for C-band is PAM-2, provided that the output power from DML is high enough (e.g. 11 dBm).

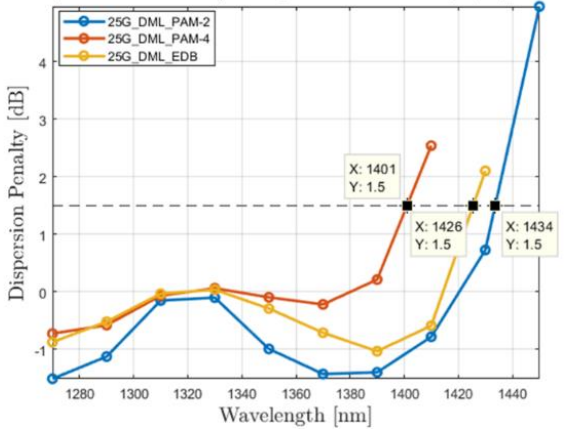
Penalty @ BER= 10^{-3} ("Complete-model1 chirp", $P_{Tx}=7\text{dBm}$)



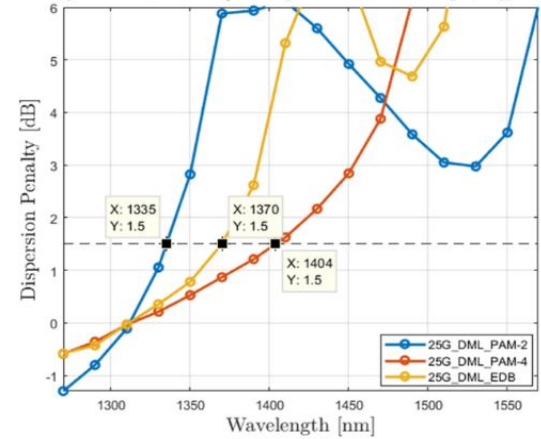
Penalty @ BER= 10^{-3} ("Complete-model2 chirp", $P_{Tx}=7\text{dBm}$)



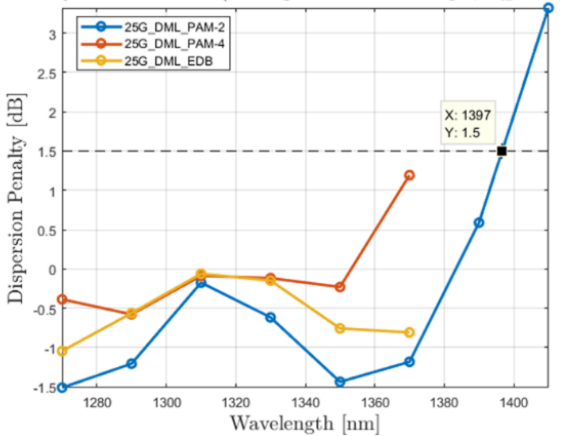
Penalty @ BER= 10^{-3} ("Complete-model1 chirp", $P_{Tx}=9\text{dBm}$)



Penalty @ BER= 10^{-3} ("Complete-model2 chirp", $P_{Tx}=9\text{dBm}$)



Penalty @ BER= 10^{-3} ("Complete-model1 chirp", $P_{Tx}=11\text{dBm}$)



Penalty @ BER= 10^{-3} ("Complete-model2 chirp", $P_{Tx}=11\text{dBm}$)

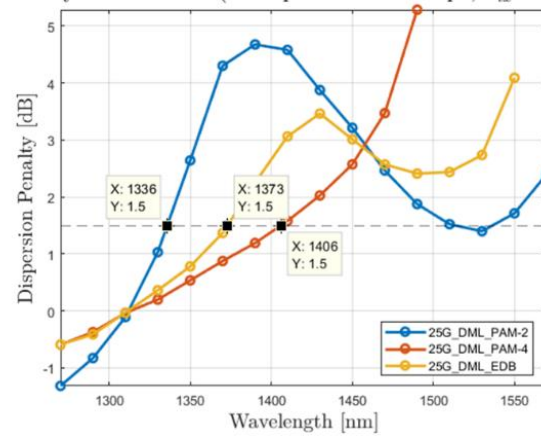


Figure 3.27. Plots of dispersion penalty curves as a function of wavelength for 25 Gbps transmission over 20 km of fiber. The full chirp is taken into account, with two different values of adiabatic chirp coefficient k : one for DML-A (denoted as "Complete-model 1 chirp", in the left column), the other for DML-T ("Complete-model 2 chirp", in the right column). To highlight the power dependence of adiabatic chirp, three values of output power from DML are considered (7 dBm, 9 dBm and 11 dBm).

3.6 DML deployment in HS-PONs

We can now take advantage of the simulation environment developed and validated in previous Sections to investigate the feasibility of DML-based HS-PONs working at more than 10 Gbps per wavelength.

3.6.1 ER and P_{tx} optimization

As emerged up to now, the DML/DD system performance turns out to have a strong dependence on two transmission parameters: ER and P_{tx} . At this point we wonder if a pair (P_{tx}, ER) exists for which the penalty due to the chirp/dispersion interplay is particularly low. The task can be accomplished by computing the receiver sensitivity for different combinations of ER and P_{tx} in meaningful ranges and eventually tracing contour plots. For this purpose, we run further simulations after choosing a reasonable set of parameters (based both on values found in [31], [32], [33] and on values provided by TIM) summarized in Table 3.7. The IRND is set to $32 \cdot 10^{-12}$ pA/ $\sqrt{\text{Hz}}$.

R_b	25 Gbps, 50 Gbps	ER [dB]	1: 0.5: 8	
λ [nm]	1270nm, 1325nm, 1550 nm	L [km]	20	
D [ps/nm/km]	17	R [A/W]	0.85	
α	3.2	G (gain of APD)	12	
k [Hz/W]	$13 \cdot 10^{12}$	F [dB]	6.8	
$f_{3\text{dB,DML}}$ [GHz]	25G-class: 24.2 10G-class: 9	$f_{3\text{dB,APD}}$ [GHz]	10G-class: 7.5	25G-class: 18
$f_{20\text{dB,DML}}$ [GHz]	25G-class: 38 10G-class: 14.1	$f_{20\text{dB,APD}}$ [GHz]	10G-class: 14	25G-class: 28
$P_{\text{tx,DML}}$ [dBm]	5: 0.5: 11			

Table 3.7. Main simulation parameters for the investigation about 25Gbps/50Gbps DML-based HSPON.

We consider the feasibility of a cost-effective rate increase to 25 Gbps or 50 Gbps involving, when reasonable, the reuse of mature (and obviously cheaper) 10G-class optoelectronics. Different system architectures are analyzed in the following Subsections along with different modulation formats.

3.6.1.1 C-band 25Gbps HS-PON with 25G DML / 10G APD

As a first option we take into consideration an asymmetrical system in which a 25G DML is used in transmission, combined to a 10G APD-based receiver. We should point out that, from a cost point of view, a 25G DML is still a reasonable choice, being, for instance, cheaper than a MZM with same bandwidth. Moreover, while it's true that we could leverage high volume 25 Gbps lasers for low cost transmitter optics (typically DMLs coming

from data centers applications), nonetheless low cost 25G APDs would not be available, since the receivers for data center applications are usually based on PIN. It is thus very likely that in the near-medium term, 25Gbps cost-effective transmissions will make use of 10G APDs [6].

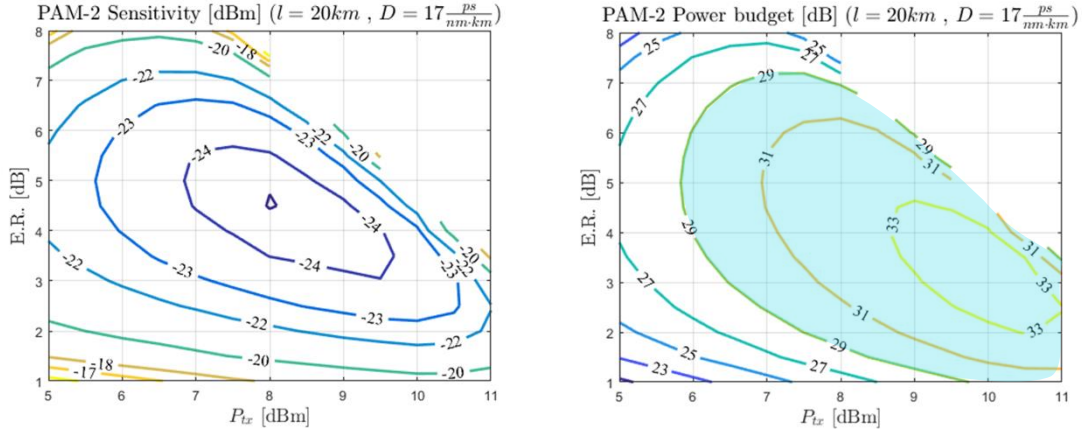


Figure 3.28. Sensitivity @ $BER = 10^{-3}$ (on the left) and power budget (on the right) contour plots for 20 km PAM-2 DML/DD 25Gbps transmission in C-band using 25G-DML/10G-APD. The feasible region for 29 dB power budget is also highlighted on the right plot. The main simulation parameters are in Table 3.7.

Results for PAM-2 transmission are reported both in terms of sensitivity (@ $BER = 10^{-3}$) and available power budget in the contour plots of Figure 3.28. By looking at sensitivity (left plot in Figure 3.28) we observe that an optimum in terms of P_{tx} and ER exists. The latter approximately lies in the proximity of the point $(P_{tx}, ER) = (8 \text{ dBm}, 4.5 \text{ dB})$. Though, what actually matters from a feasibility point of view is the available optical power budget (right plot in Figure 3.28). We assume to be interested in having at least 29 dB¹² power budget, which can serve to tolerate an up to 29 dB optical path loss (OPL) inside the ODN. For a fixed length system, we define the feasible region for a given fiber length as the area of the (P_{tx}, ER) plane in which the available power budget is greater or equal than our target one. For instance, in the right plot of Figure 3.28, the area highlighted in light blue represents the feasible region for a 20 km long fiber. The area is quite large: this remarks the feasibility of this system, with pretty good tolerance to slight variations of ER and P_{tx} .

The same kind of results are also reported for the cases of EDB and PAM-4 respectively in Figure 3.29 and Figure 3.30.

¹² This power budget value is denoted, in ITU standards, as class N1 [41] and, in IEEE ones, as class PR(X)30 [39].

The left plot of Figure 3.29 points out that EDB transmission presents an optimum sensitivity in the neighborhood of $(P_{tx}, ER) = (8 \text{ dBm}, 7.5 \text{ dB})$. On the other hand, the power budget plot on the right side shows that even in this case, a feasible region exists, though smaller. Moreover, the latter offers less flexibility in terms of P_{tx} w.r.t. what happened with PAM-2 transmission.

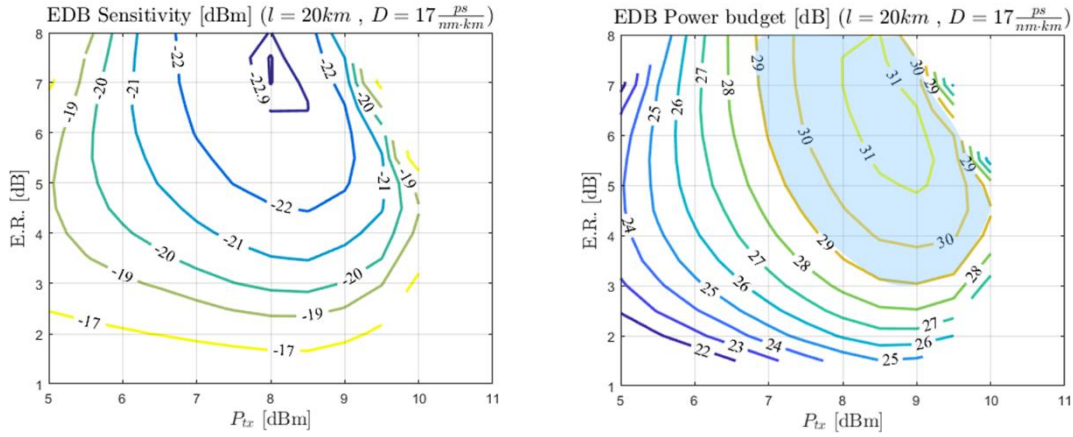


Figure 3.29. Sensitivity @ $BER = 10^{-3}$ (on the left) and power budget (on the right) contour plots for 20 km EDB DML/DD 25Gbps transmission in C-band using 25G-DML/10G-APD. The feasible region for 29 dB power budget is also highlighted on the right plot. The main simulation parameters are in Table 3.7.

Finally, when adopting the same system for PAM-4 transmission (Figure 3.30), the optimum in sensitivity moves to $(P_{tx}, ER) = (8 \text{ dBm}, 5 \text{ dB})$, while the feasible region drastically reduces in size. Transmission is still feasible, but the requirements on transmission parameters are stricter. It's worth to observe that, in general, the optimum sensitivity point does not necessarily fall inside the feasible region: indeed, this is the case for PAM-4. The feasible region includes points close to $(P_{tx}, ER) = (10 \text{ dBm}, 3.5 \text{ dB})$.

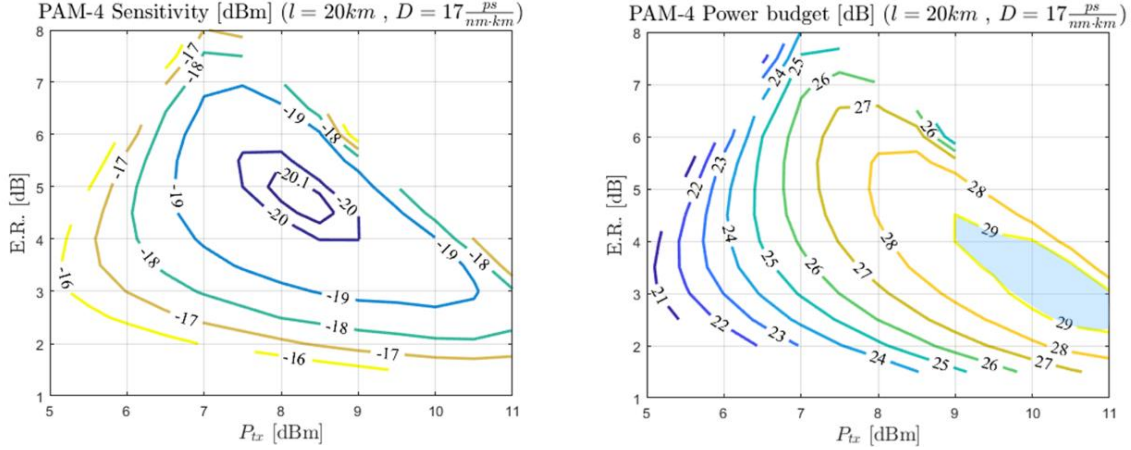


Figure 3.30. Sensitivity @ $BER = 10^{-3}$ (on the left) and power budget (on the right) contour plots for 20 km PAM-4 DML/DD 25Gbps transmission in C-band using 25G-DML/10G-APD. The feasible region for 29 dB power budget is also highlighted on the right plot. The main simulation parameters are in Table 3.7.

3.6.1.2 C-band 25Gbps HS-PON with 10G DML / 10G APD

We now relax further the requirements on the transmitter by investigating the possibility of deploying a 10G-class DML combined to a 10G-class APD.

The results for the PAM-2, EDB and PAM-4 transmission in C-band are reported respectively in Figure 3.31, Figure 3.32 and Figure 3.33. The latter show that each modulation format presents its optimum sensitivity value, which is achieved for some given pairs (P_{tx} , ER). Nevertheless, none of the considered modulation formats is able to ensure the feasibility of the system: 29 dB power budget cannot be attained. Anyway, PAM-2 goes very close to the target, allowing for up to about 28 dB power budget. Feasibility could probably be achieved by slightly improving the system parameters, e.g. by using a less noisy receiver.

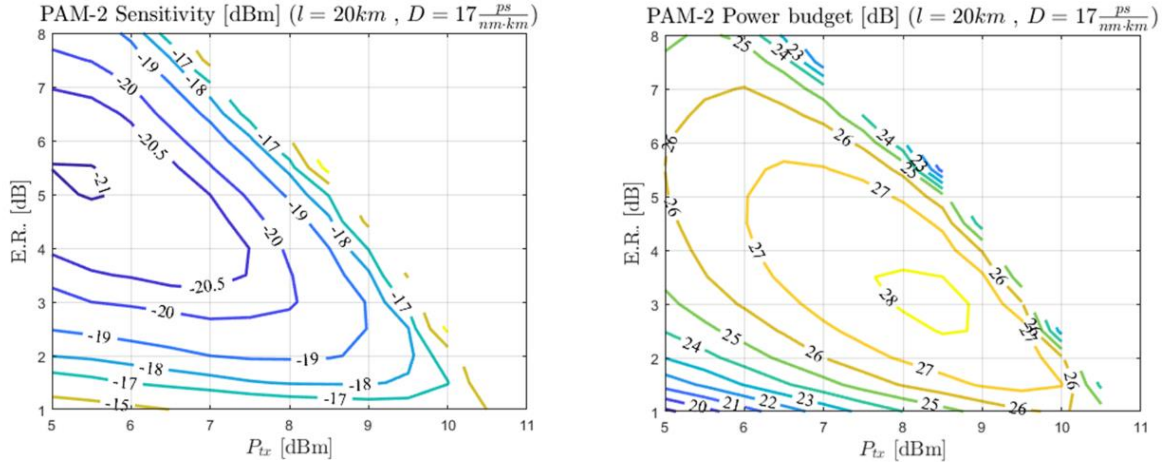


Figure 3.31. Sensitivity @ $BER = 10^{-3}$ (on the left) and power budget (on the right) contour plots for 20 km PAM-2 DML/DD (10G-DML + 10G-APD) 25 Gbps transmission in C-band. The main simulation parameters are in Table 3.7.

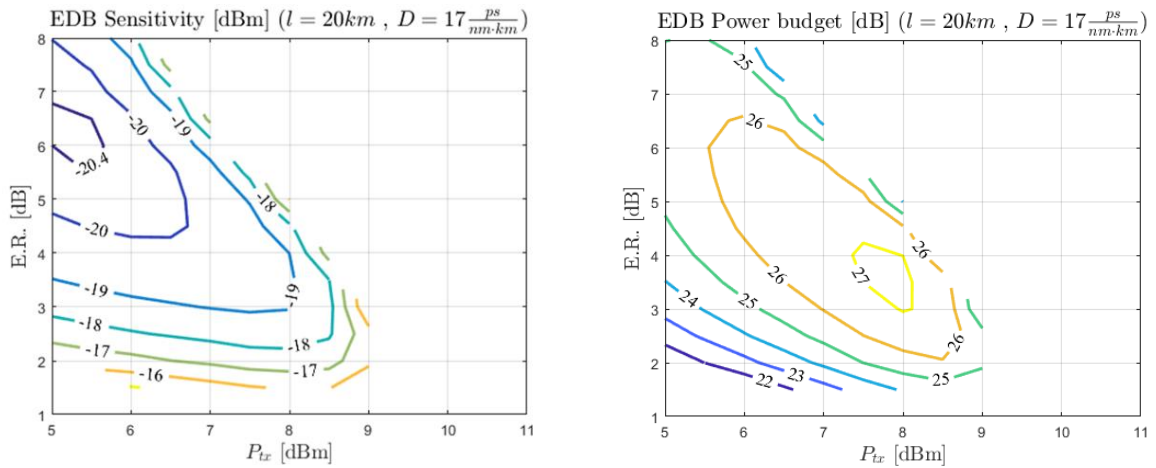


Figure 3.32. Sensitivity @ $BER = 10^{-3}$ (on the left) and power budget (on the right) contour plots for 20 km EDB DML/DD (10G-DML + 10G-APD) 25 Gbps transmission in C-band. The main simulation parameters are in Table 3.7.

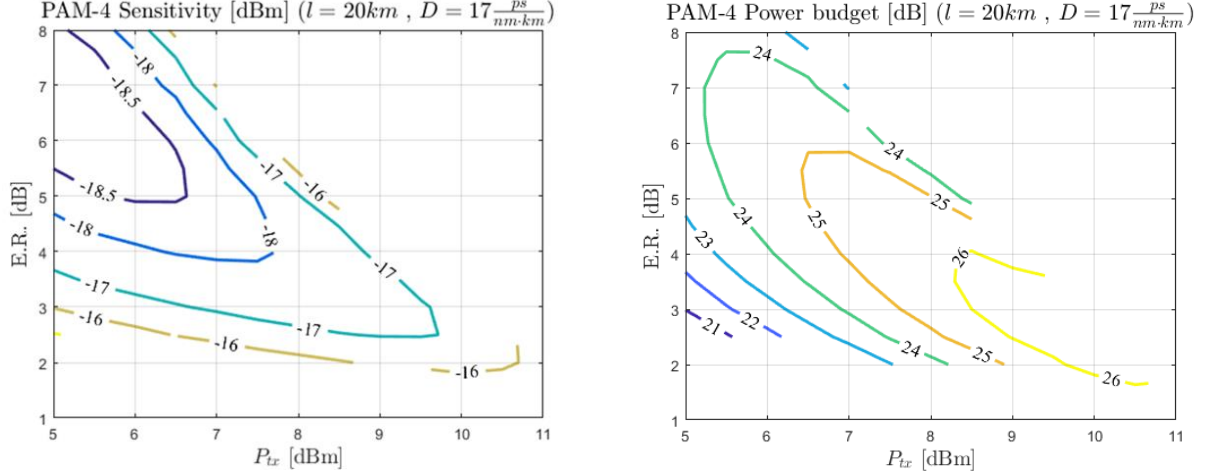


Figure 3.33. Sensitivity @ $BER = 10^{-3}$ (on the left) and power budget (on the right) contour plots for 20 km PAM-4 DML/DD (10G-DML + 10G-APD) 25 Gbps transmission in C-band. The main simulation parameters are in Table 3.7.

3.6.1.3 O-band 50Gbps HS-PON with 25G DML / 25G APD

Another interesting scenario to be analyzed is 50Gbps transmission using 25G DML and APD. In this case, having verified that C-band operation is not feasible for any of the modulation formats, we choose to perform our simulations in O-band. Precisely, we consider two wavelengths ($\lambda = 1270 \text{ nm}$ and $\lambda = 1325 \text{ nm}$) with two different dispersion signs (respectively $D = -5 \frac{\text{ps}}{\text{nm}\cdot\text{km}}$ and $D = 2.5 \frac{\text{ps}}{\text{nm}\cdot\text{km}}$). In general, by changing the wavelength, the optimum sensitivity changes (and so the corresponding ER and P_{tx} do) and the feasible region (if it exists) moves. In particular, it happens that:

- PAM-2 transmission (Figure 3.34 and Figure 3.35) and EDB transmission (Figure 3.36 and Figure 3.37) are feasible for both wavelength values, though at 1270 nm their feasible regions results much larger than at 1325 nm. Between the two modulation formats, anyway, the most suitable is PAM-2, which allows more flexibility;
- PAM-4 transmission (Figure 3.38 and Figure 3.39), instead, happens to be feasible only at 1270 nm and with a very narrow feasible region. The adoption of this modulation format is thus inappropriate.

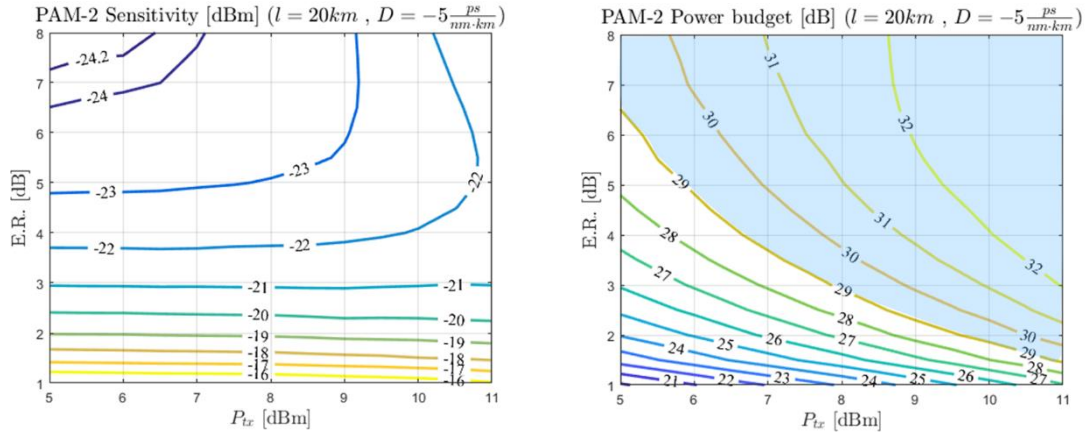


Figure 3.34. Sensitivity @ $BER = 10^{-3}$ (on the left) and power budget (on the right) contour plots for 20 km PAM-2 DML/DD (25G-DML + 25G-APD) 50 Gbps transmission in O-band (negative D). The feasible region for 29 dB power budget is also highlighted on the right plot. The main simulation parameters are in Table 3.7.

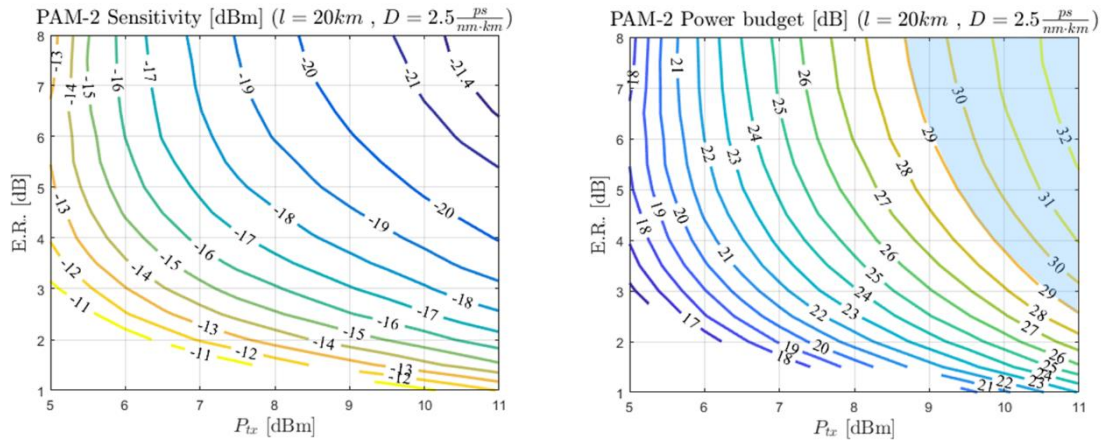


Figure 3.35. Sensitivity @ $BER = 10^{-3}$ (on the left) and power budget (on the right) contour plots for 20 km PAM-2 DML/DD (25G-DML + 25G-APD) 50 Gbps transmission in O-band (positive D). The feasible region for 29 dB power budget is also highlighted on the right plot. The main simulation parameters are in Table 3.7.

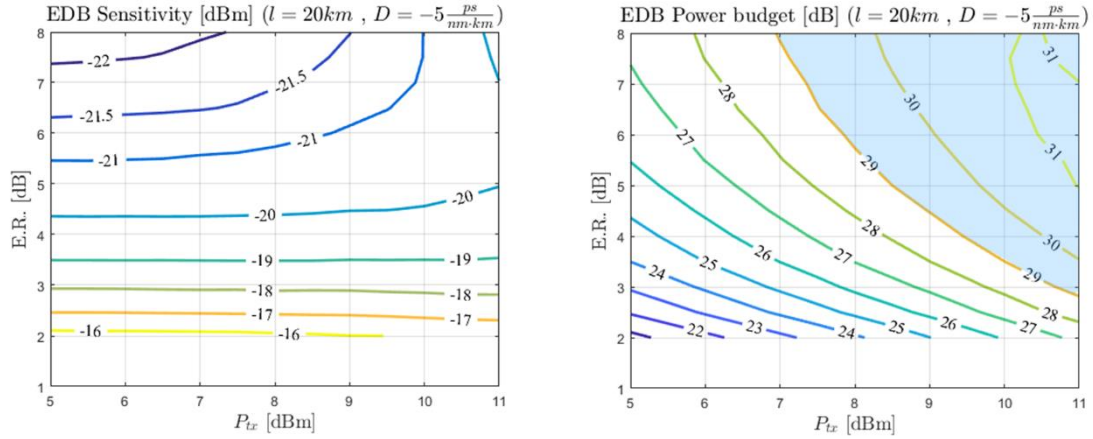


Figure 3.36. Sensitivity @ $BER = 10^{-3}$ (on the left) and power budget (on the right) contour plots for 20 km EDB DML/DD (25G-DML + 25G-APD) 50 Gbps transmission in O-band (negative D). The feasible region for 29 dB power budget is also highlighted on the right plot. The main simulation parameters are in Table 3.7.

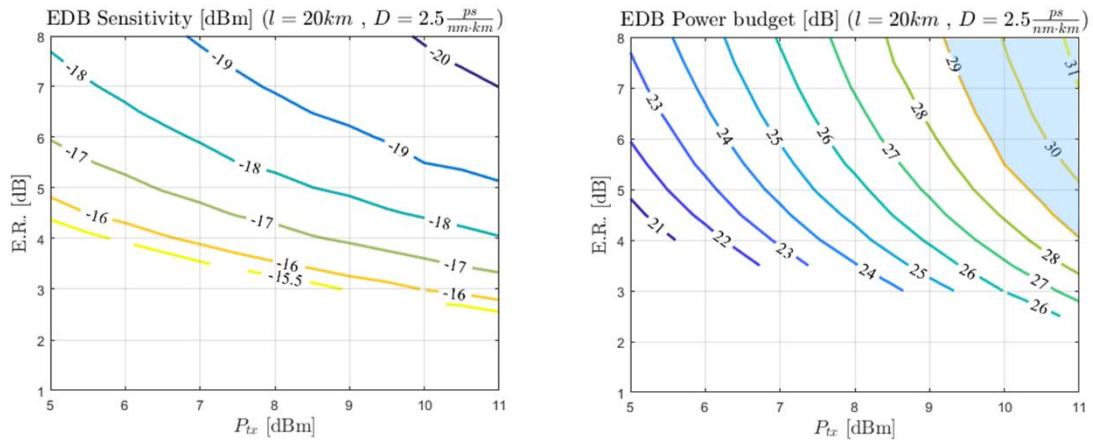


Figure 3.37. Sensitivity @ $BER = 10^{-3}$ (on the left) and power budget (on the right) contour plots for 20 km EDB DML/DD (25G-DML + 25G-APD) 50 Gbps transmission in O-band (positive D). The feasible region for 29 dB power budget is also highlighted on the right plot. The main simulation parameters are in Table 3.7.

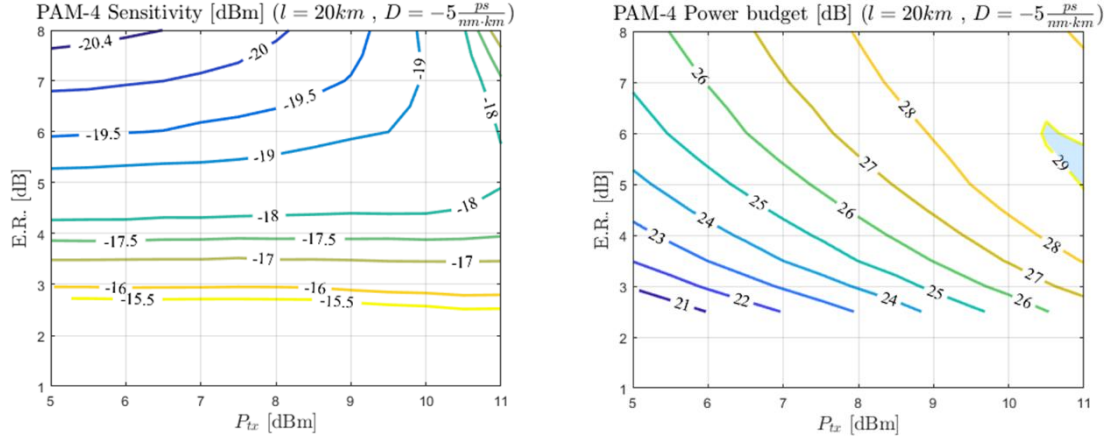


Figure 3.38. Sensitivity @ $BER = 10^{-3}$ (on the left) and power budget (on the right) contour plots for 20 km PAM-4 DML/DD (25G-DML + 25G-APD) 50 Gbps transmission in O-band (negative D). The feasible region for 29 dB power budget is also highlighted on the right plot. The main simulation parameters are in Table 3.7.

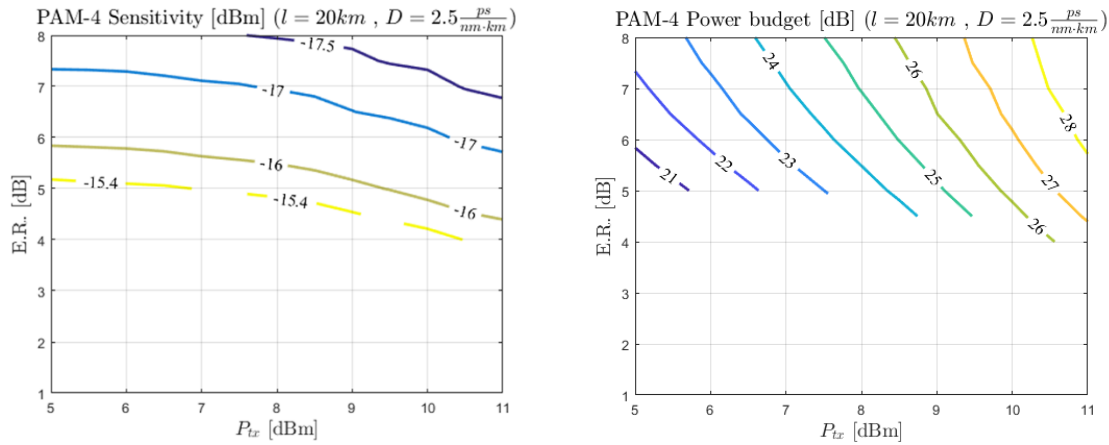


Figure 3.39. Sensitivity @ $BER = 10^{-3}$ (on the left) and power budget (on the right) contour plots for 20 km PAM-4 DML/DD (25G-DML + 25G-APD) 50 Gbps transmission in O-band (positive D). The feasible region for 29 dB power budget is also highlighted on the right plot. The main simulation parameters are in Table 3.7.

3.6.1.4 DML-based HS-PON over 20km – Summary

The results presented in Subsections 3.6.1.1-3.6.1.3 are summarized for ease of reference in Table 3.8 and Table 3.9 respectively for 25 Gbps and 50 Gbps transmission.

	25G DML / 10 G APD (C-band)	10G DML / 10G APD (C-band)
PAM-2	✓ (large feasible region)	✗ (but close to feasibility)
EDB	✓ (medium feasible region)	✗
PAM-4	✓ (small feasible region)	✗ (worst)

Table 3.8. Summary table of the simulated results of this Section for 25Gbps transmission with 20km long SSMF.

	25G DML / 25G APD (O-band)	25G DML / 25G APD (C-band)
PAM-2	✓ (large feasible region)	✗
EDB	✓ (medium feasible region)	✗
PAM-4	✗	✗

Table 3.9. Summary table of the simulated results of this Section for 50Gbps transmission with 20km long SSMF.

3.6.2 Multiple distance systems: the overall feasible region

All of the results in Section 3.6.1 were referred to a fiber length of 20 km. In general, in a real PON, the distance from the OLT typically varies from one ONU to another. For the sake of completeness, in order to assess the system operation, one should consider each possible OLT-ONU distance in the PON and intersect, if possible, all of the corresponding feasible regions. We call the overall feasible region, if it exists, the region obtained by such an intersection. It's worth noticing that the feasibility conclusions drawn in Section 3.6.1 are not wrong, but just “incomplete” when applied to a true PON. In the current Section, we fix a scenario and show this graphical intersection method to assess the feasibility of a system. In Section 3.6.2.1 we choose to focus on the case of 25 Gbps transmission in C-band with 25G DML and 10G APD, by reusing the same system parameters as Section 3.6.1.1. As for the fiber length, we consider (realistic) values in the range from 5 km to 25 km with steps of 5 km.

3.6.2.1 C-band 25 Gbps HS-PON with 25G DML/10G APD

The sensitivity contour plots for the three modulation formats under analysis in the back-to-back case are reported in Figure 3.40. The horizontal lines point out that, as expected, in absence of dispersion there's no

dependence of the performance on the output power from DML. Indeed, power dependence is a feature of adiabatic chirp, whose effects manifest in presence of a non-null accumulated dispersion. As for ER, instead, the higher it is, the better is the performance: in absence of dispersion, an increased level separation is always beneficial.

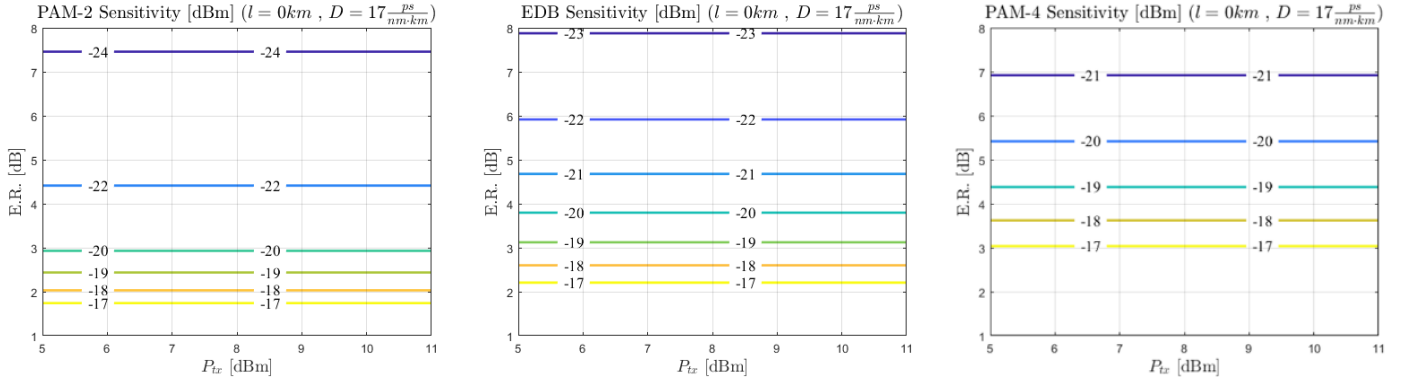


Figure 3.40. Back-to-back sensitivity contour plots for PAM-2 (on the left), EDB (in the middle) and PAM-4 (on the right) DML/DD 25Gbps transmission in C-band using 25G-DML/10G-APD. The other simulation parameters are kept as in Table 3.7.

The corresponding power budget contour plot in back-to-back is reported in Figure 3.41. The latter allow to identify the back-to-back feasible regions for a given target available power budget.

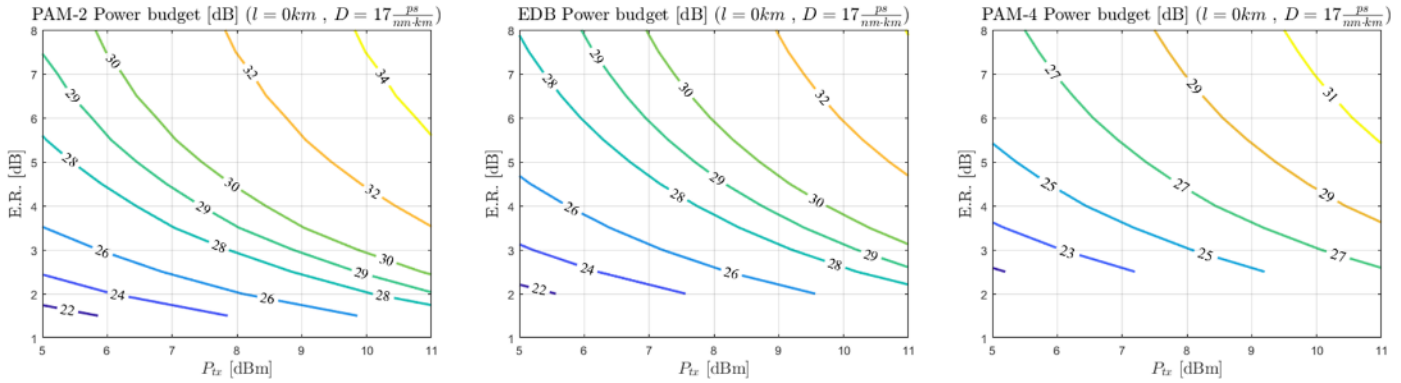


Figure 3.41. Back-to-back power budget contour plot for PAM-2 (on the left), EDB (in the middle) and PAM-4 (on the right) DML/DD 25Gbps transmission in C-band using 25G-DML/10G-APD. The other simulation parameters are kept as in Table 3.7.

As the fiber length increases, the sensitivity and power budget curves change. This evolution can be clearly visualized in the plots of Figure 3.42 and Figure 3.43. The qualitative trend is the same for all of the three modulation formats: when distance increases from 5 km to 25 km, the optimum sensitivity value moves toward

lower P_{tx} and lower ER . As for the feasible regions, they tend to narrow more and more as distance grows. The lines delimiting the 29 dB power budget regions have been extracted in order to identify, by intersection, the overall feasible region. The latter are depicted, for the three modulation formats, in Figure 3.44. From it we deduce that PAM-2 enables system operation, presenting a relatively wide overall feasible region. EDB transmission is also feasible, but with less flexibility in transmitted power compared to PAM-2. The worst performing is the PAM-4 system, which is not feasible if all of the considered OLT-ONU distances are present in the PON layout.

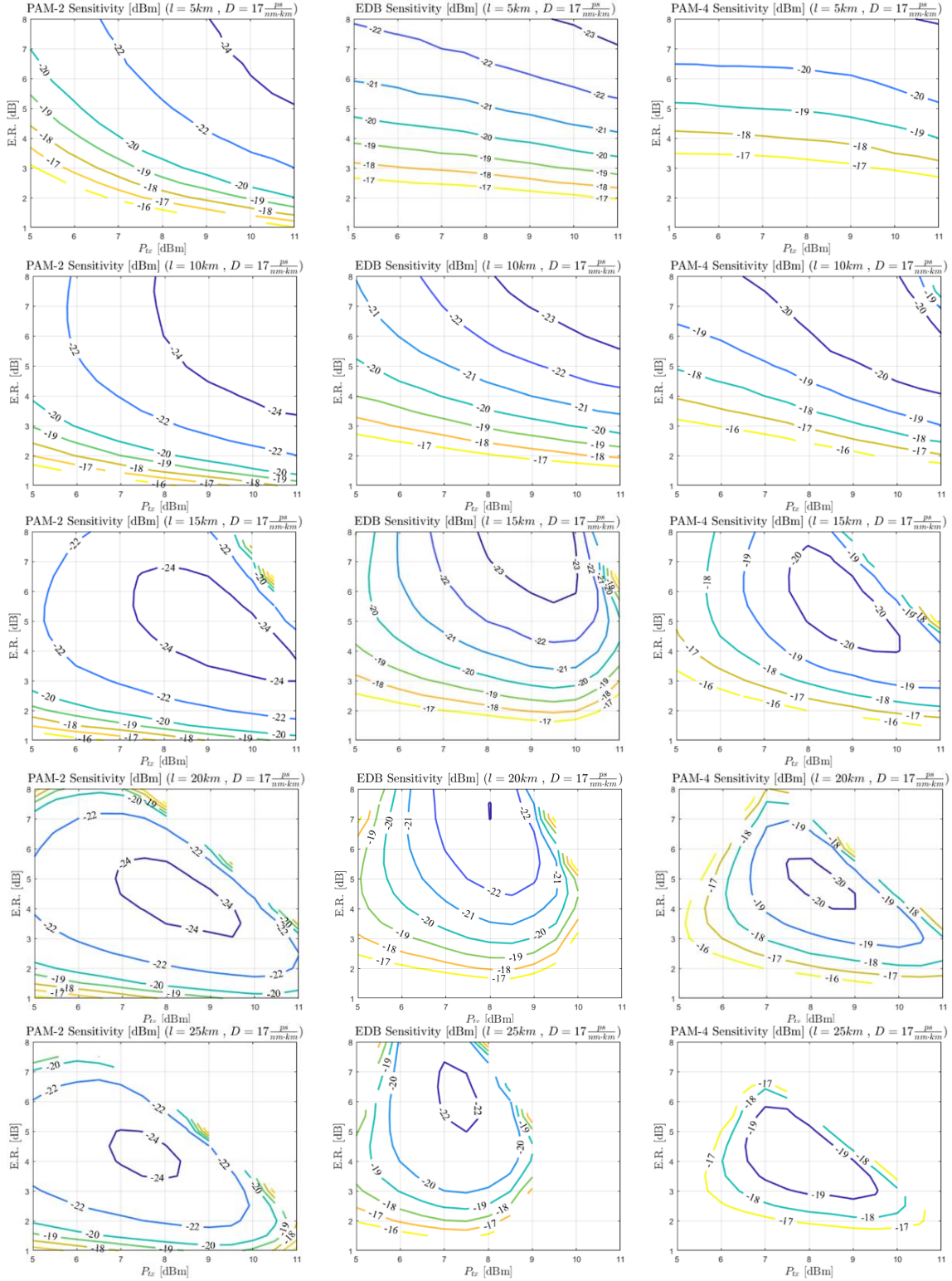


Figure 3.42. Sensitivity contour plots for different modulation formats (in the three columns) and fiber lengths (increasing length going down with the rows), for 25Gbps C-band transmission using 25G-DML/10G-APD. The other simulation parameters are kept as in Table 3.7.

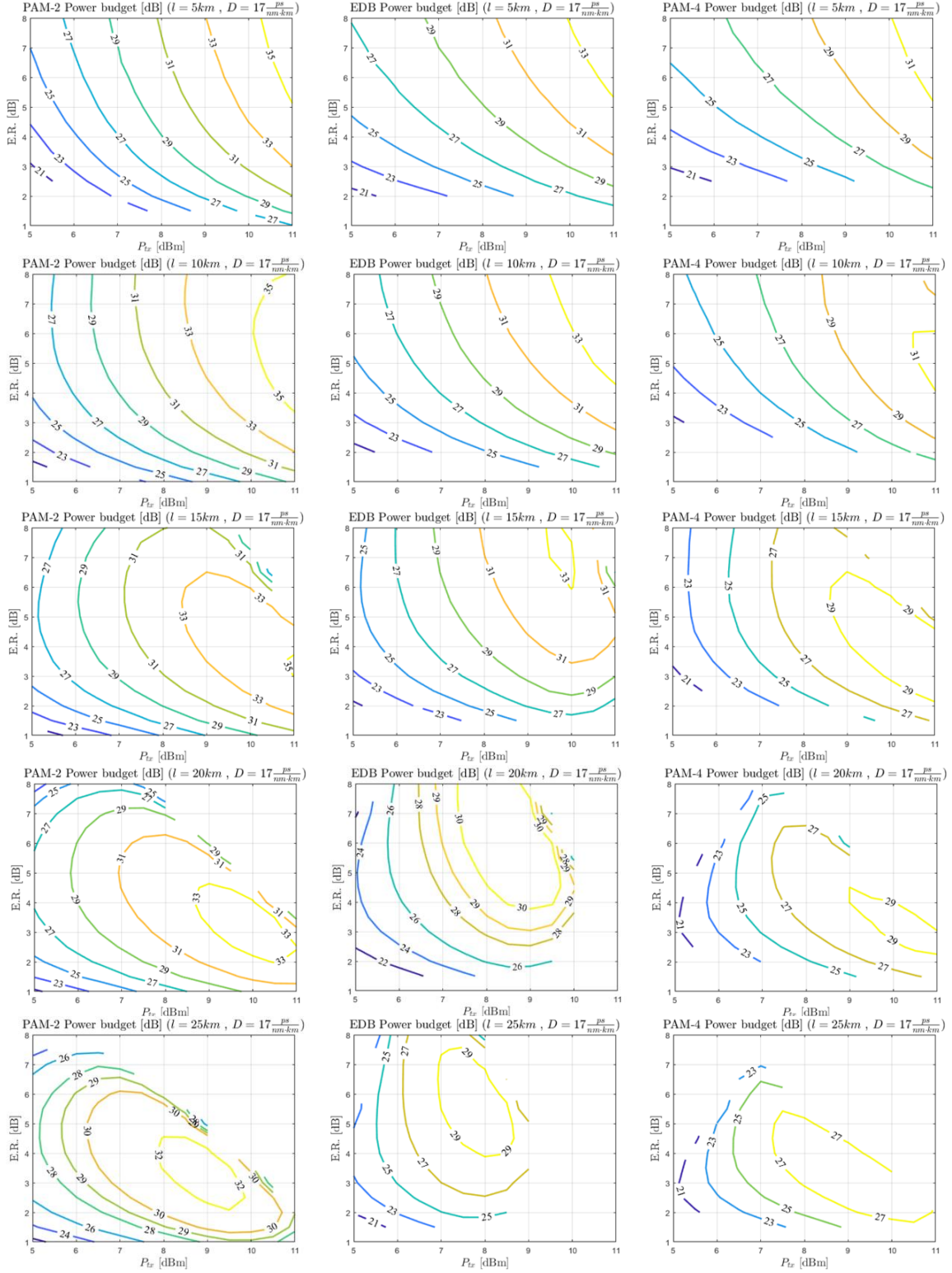


Figure 3.43. Power budget contour plots for different modulation formats (in the three columns) and fiber lengths (increasing length going down with the rows), for 25Gbps C-band transmission using 25G-DML/10G-APD. The other simulation parameters are kept as in Table 3.7.

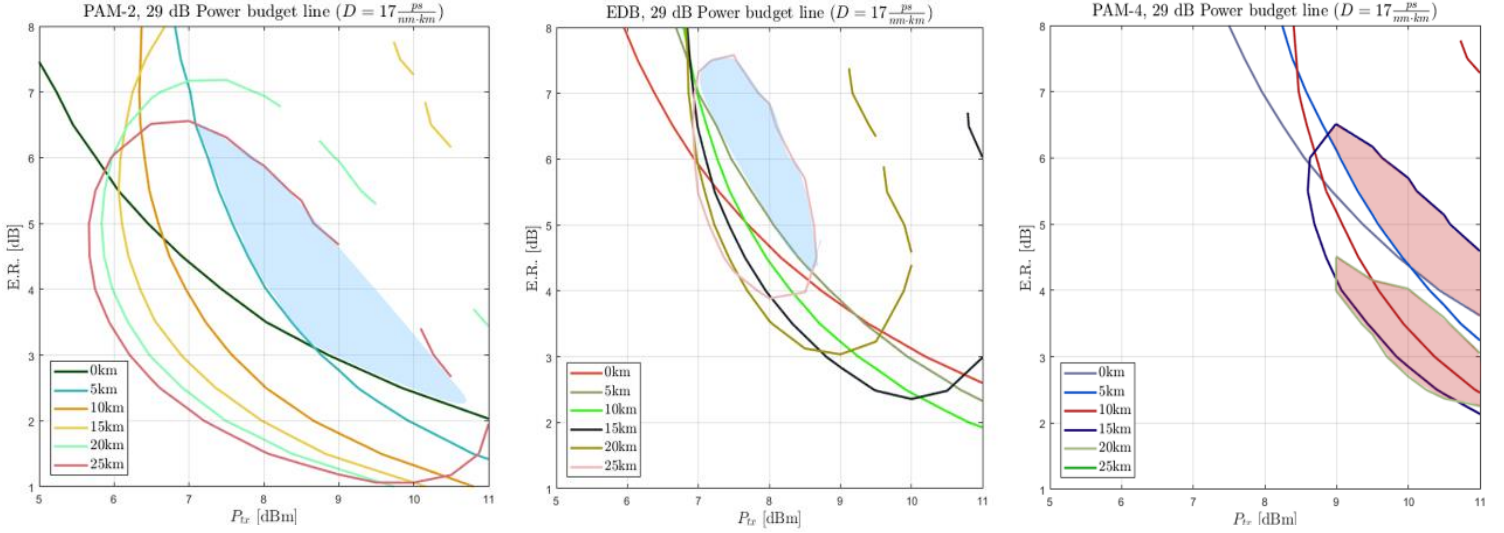


Figure 3.44. 29 dB power budget lines extracted from the power budget contour plot for 25Gbps C-band transmission using 25G-DML/10G-APD. The overall feasible region is highlighted in light blue for PAM-2 and EDB. Instead, in PAM-4, the regions for 20km feasibility and less-than-20km feasibility result to be disjointed. The other simulation parameters are kept as in Table 3.7.

3.7 Conclusions

In this Chapter we have developed and validated a simulation framework for testing DML/DD HS-PON systems. The main message is that the use of a DML, besides being advantageous from a cost point of view, can take advantage of the adiabatic component of the chirp. The latter, interacting with chromatic dispersion, can help to increase the system reach, independently on the sign of the dispersion parameter. We demonstrated by simulations the feasibility of 25Gbps transmission in C-band using 25G DML / 10G APD and of 50Gbps transmission in O-band using 25G DML / 25G APD. We also showed that a 25Gbps transmission in C-band using 10G DML / 10G APD is not too far from feasibility, at least when using PAM-2 modulation and equalization at receiver. Eventually, we gave an example of feasibility assessment in the case of a multiple-length systems, as typical PONs are. As a further work, these very promising simulation results should be verified by a proper set of experiments on a commercial laser.

Chapter 4: Equalization for burst-mode transmission

The aim of this Chapter is to focus on the implementation of adaptive equalization strategies specifically tailored for burst-mode transmission, which is a peculiarity of the US of a PON. An introduction to the problem is provided (Section 4.1), along with some theoretical hints about adaptive feed-forward equalization and LMS algorithm (Section 4.2). The approach is simulative: the adopted simulation setup is introduced in Section 4.3, then, in Sections 4.4-4.7, some relevant results are exposed concerning the optimization of the main equalization parameters. Conclusions are drawn in Section 4.8. We point out that a paper on this topic, including some of the results from this Chapter (and from Chapter 5), was submitted in October 2018 to the main Conference of the field (OFC2019).

4.1 The need for a burst-mode equalization algorithm

If cost was not an issue, the simplest way to increase the line rate in a TDM-based PON would be the use of premium optical components (provided that they allow to satisfy the required power budget): e.g. the use of transceivers which are not band-limited. Anyway, this is not the case, and indeed many options have been proposed in the literature which enable a cost-effective rate increase for HS-PONs [11]. Among them, we find the use of band-limited transceivers in conjunction with high spectral efficiency modulation formats (such as PAM-4 and duobinary detection, either electrical or optical). We've already analyzed this possibility in previous Chapters. Besides, to overcome the bandwidth limitations and the lower chromatic dispersion tolerance deriving from the use of higher bitrates, a valid aid is represented by digital signal processing techniques such as equalization. Nevertheless, the choice of the particular equalization technique to be used and of its main parameters is non-trivial and the equalizer itself requires different approaches depending upon whether we're considering a continuous-mode transmission or a burst-mode one.

A continuous-mode receiver has, as its input, an uninterrupted stream of bits of similar peak-to-peak amplitude, phase and frequency [34]. This is the case of the downstream channel of a PON, in which the only transmitter is the OLT settled in the central office. In this case, a DSP placed in the ONU could implement in a straightforward way one of the many available equalization techniques available in the literature (MLSE, FFE, FFE/DFE ...), the "only" (actually non-trivial) limitation being computational complexity (and power consumption). Thanks to this approach, as an example, demonstrations of 25Gbps downstream transmission

with 10G components were made possible [35]. This is also the kind of approach to equalization we had in the previous Chapters simulations, which thus were mainly targeting a downstream analysis.

Contrarily, a burst-mode receiver presents an additional issue: the signal stream on the channel results from the aggregation of different bursts (potentially of different durations) coming from different transmitters (the ONUs), each of which can be placed at a different distance L from the unique receiver (the OLT). Consequently, each burst will have different amplitude (due to different attenuations) and clock phase and will experience different impairments caused by chromatic dispersion (due to different values of accumulated dispersion $D \cdot L$), laser chirp (e.g. some ONUs lasers may be adiabatic-dominated, some other may be transient-dominated) and transmitter non-linearities [36, 37, 38]. The burst-mode receiver at the OLT will have to deal with different bursts alternated each other with guard times in between. The overall received signal is characterized by a given dynamic range (DR), specified as the ratio, typically expressed in dB units, between the highest average power of a burst (obtained for a “loud burst”) and the lowest one (obtained for a “soft burst”) [38, 39]. The structure of a stream of this kind is illustrated in the Figure 4.1.

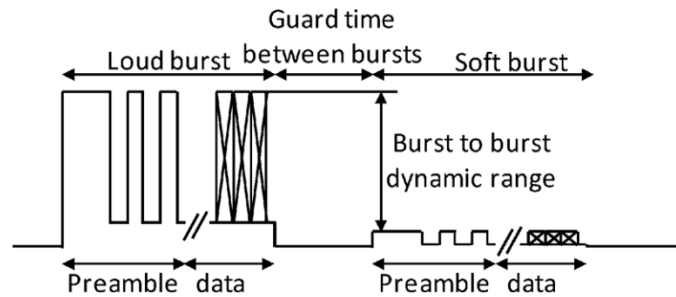


Figure 4.1 Pictorial representation of a burst mode bit stream. From [34].

To further complicate things, it’s worth to notice that, in an even more complex scenario, bursts from different ONUs could make use of different modulation formats with different spectral efficiency. In the resulting signal, different formats are interleaved. An experimental verification of a dual-rate burst mode receiver can be found in [40]. Figure 4.2 clearly shows the idea.

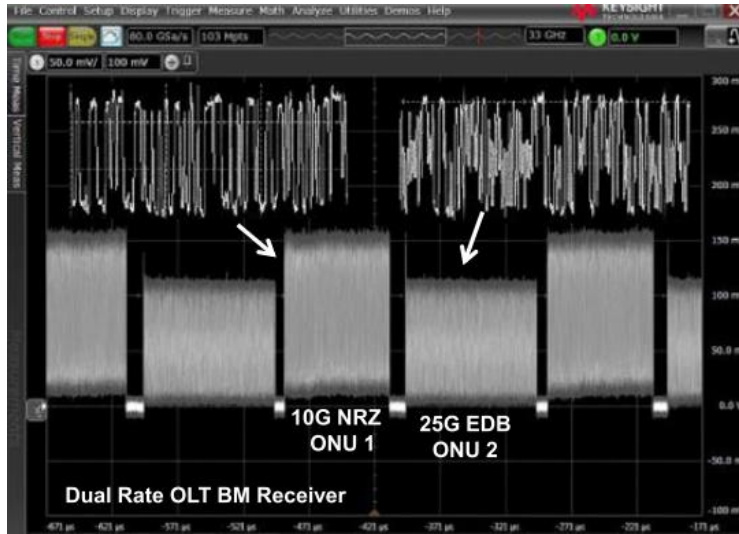


Figure 4.2 Upstream 10G PAM-2 bursts interleaved with 25G EDB burst detected with 10G APD receiver. Picture from [41].

In this very complex scenario, an adaptive equalization algorithm is required, able to properly adjust the taps from one burst to another. Each burst will thus require a structure made up by a preamble and a data section (payload). The preamble includes a training sequence which is exploited in reception for taps adaptation in the equalizer (according to a certain algorithm). Moreover, it's important to point out that, in order for an equalizer to work, typically it is required that the amplitude of its input signal remains constant with time [39]. This task is generally accomplished in a linear burst mode receiver (LBMRx) by exploiting the training sequence (the same used for taps adjustment) also for gain setting.

Still, careful considerations need to be done in order to properly choose the most suitable equalization algorithm and the tuning of its parameters. Moreover, the minimum required length of the training sequence (which represent an overhead for the transmission) will depend on the particular configuration of the equalizer at the OLT. All of these choices, as we will see in the following pages, present a trade-off between performance and complexity.

4.2 Adaptive equalization: the LMS algorithm

In this Section we review the fundamental concepts about adaptive feed-forward equalization exploiting the LSM algorithm., in order to study (in next Sections) its application to the case of burst-mode reception.

We consider adaptive channel equalization in the form of a finite impulse response (FIR) filter whose tap coefficients $h(k)$ are dynamic (not static), i.e. they adjust in time according to a certain algorithm. The latter, in general, must define a certain performance metric (e.g. a measure of distortion or similarity) to be optimized and a procedure to update the filter coefficients accordingly. The general structure of an adaptive equalizer is depicted in Figure 4.3.

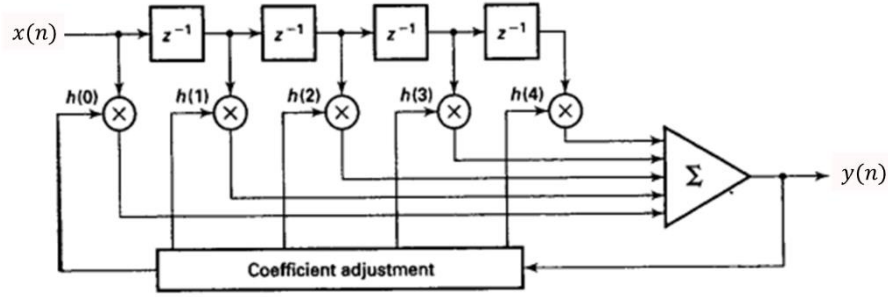


Figure 4.3. Adaptive equalizer with a generic coefficient adjustment algorithm. From [42].

Typically, the coefficients are initialized arbitrarily, then a proper algorithm (which also determines the filter stability [42]) is supposed to make them converge to the optimum set in a given amount of time. Several coefficient-updating algorithms have been proposed in the literature [21]. One among the most commonly employed ones uses, as a distortion measure to be minimized, the sum of the squared errors between its output sequence $y(n)$ and a desired sequence $d(n)$, i.e. the mean square error \mathcal{E} (MSE), which is a quadratic function of the tap coefficients [42]:

$$\mathcal{E} = \sum_{n=0}^M e^2(n) = \sum_{n=0}^M (d(n) - y(n))^2 = \sum_{n=0}^M \left[d(n) - \sum_{k=0}^{N-1} h(k)x(n-k) \right]^2 \quad (4.1)$$

This approach goes under the name of Least Mean Square (LMS) criterion. Being \mathcal{E} a convex function with a single minimum, the optimization of the filter coefficients can be obtained through an approximation of the gradient algorithm. In particular, whenever a new sample enters the FIR filter, the filter coefficients are updated according to the LMS update equation:

$$h_n(k) = h_{n-1}(k) - \mu \cdot e(n) \cdot x(n-k) \quad 0 \leq k \leq N-1, \quad n = 0, 1, \dots \quad (4.2)$$

in which N denotes the number of taps (filter length), n is the discrete time index and μ is the step size parameter (or “adaptation rate coefficient”). The choice of the latter is of fundamental importance and represents a trade-off between convergence rate (i.e. the time required to reach the optimum) and algorithm stability. A fast convergence can be forced by increasing the step size value. Nevertheless, when μ is too large, the algorithm becomes unstable and the steady state error becomes large, leading to performance degradation. As a rule of thumb, it was demonstrated that stability is ensured whenever μ is chosen such that [42]:

$$0 < \mu < \frac{1}{10NP_x} \quad (4.3)$$

in which P_x denotes the input signal power. In the following (Section 4.4), we’ll study the influence of μ on the system performance using a simulative approach.

As for the desired sequence $d(n)$ which appears in the error expression $e(n) = d(n) - y(n)$ used in the update equation, it’s worth to highlight that it can assume two different meanings. Indeed:

- $d(n)$ is an a-priori known (at receiver) training sequence, which just serves to make the FIR coefficients adjust as close as possible to convergence. In this case, the equalizer is said to operate in “training mode”. Typically, this is needed at the beginning of a “new” transmission;
- $d(n)$ is derived from the decoder output. This is like assuming that the decision is correct. This operation mode is called “tracking” (or “decision directed”), since it allows the receiver to still update the tap coefficients to track small variations in the channel frequency response. Anyway, this requires the taps to be already sufficiently close to the optimum value, with a certain degree of confidence. For this reason, the “tracking phase” should follow a sufficiently long “training phase”. It is evident that a “good” receiver should almost always work in tracking mode, since the bits used for training mode do not carry useful digital information. We’ll investigate further this aspect through simulations in next Sections.

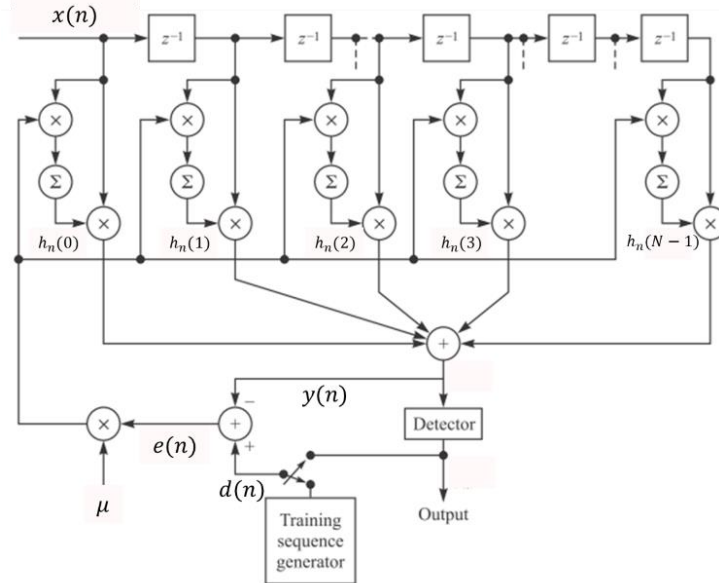


Figure 4.4. Adaptive equalizer based on LMS algorithm. The training and tracking operation modes are highlighted. From [21].

The two operation modes of the LMS adaptive equalizer are graphically represented in the bottom part of Figure 4.4, in which a switch turns from the training sequence generator (used in the training phase) to the detector (used in tracking phase).

Finally, we point out that the LMS algorithm is a general procedure which must be applied in the very first phase of a continuous transmission. Anyway, we're here interested in adapting it to the burst-mode scenario which characterizes the upstream of a PON.

4.3 Simulation setup

In order to assess the performance of the above introduced FFE equalizer, we choose to operate our simulated PON system in a scenario in which equalization is a must (i.e. the received eye diagram is completely destroyed by distortion). In particular, we adopt the same simulation setup with 25G DML and 10G APD as seen at the end of Chapter 3 together with an operational point (in terms of ER and output DML power) which was proven to be in the middle of the overall feasible region for PAM-2. The block scheme (with an explicit identification of ONU and OLT for the upstream case) is depicted in Figure 4.5.

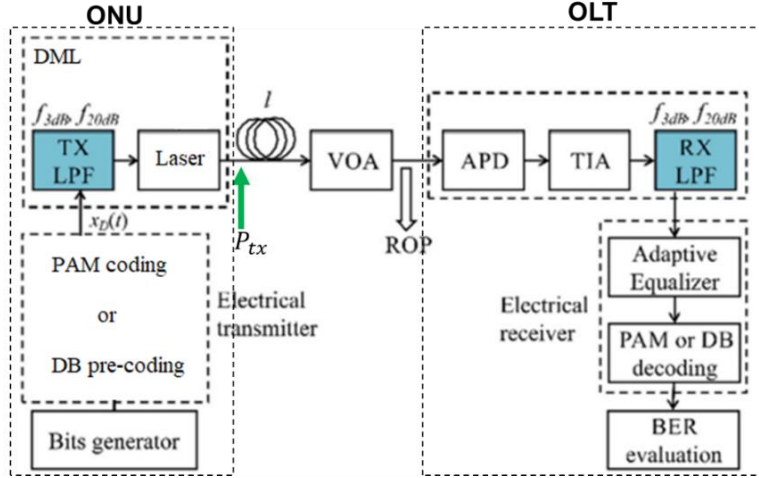


Figure 4.5. Block scheme of the simulation setup used for upstream equalization analysis.

The main simulation parameters are reported in Table 4.1. The employed adaptive equalizer is a 20 taps FFE working at 2 samples per symbol (i.e. the FIR filter keeps memory of 10 symbols) and using the LMS algorithm for tap adjustment. The initial taps state is, for now, arbitrarily assumed to be “all-zeros”, i.e., using the same notation as Section 4.2:

$$h_0(k) = 0 \quad 0 \leq k \leq N - 1 \quad (4.4)$$

Figure 4.6 depicts an example of an eye diagram of the received unequalized signal along with the corresponding one after equalization in the same simulation setup, albeit for a different wavelength (which is anyway in C-band).

R_b	25 Gbps	ER [dB]	4*
λ [nm]	1550	R [A/W]	0.85
D [ps/nm/km]	17	G (gain of APD)	12
α	3.2	F [dB]	6.8 (i.e. $k=0.35$, for InP)
k [Hz/W]	$13 \cdot 10^{12}$	$f_{3dB,APD}$ [GHz]	7.5
$f_{3dB,DML}$ [GHz]	24.2	$f_{20dB,APD}$ [GHz]	14
$f_{20dB,DML}$ [GHz]	38	$IRND$ [pA/ \sqrt{Hz}]	$32 \cdot 10^{-12}$
$P_{tx,DML}$ [dBm]	8.8*		

*The values of P_{tx} and ER are optimized for PAM-2

Table 4.1. Main simulation parameters used for upstream equalization analysis.

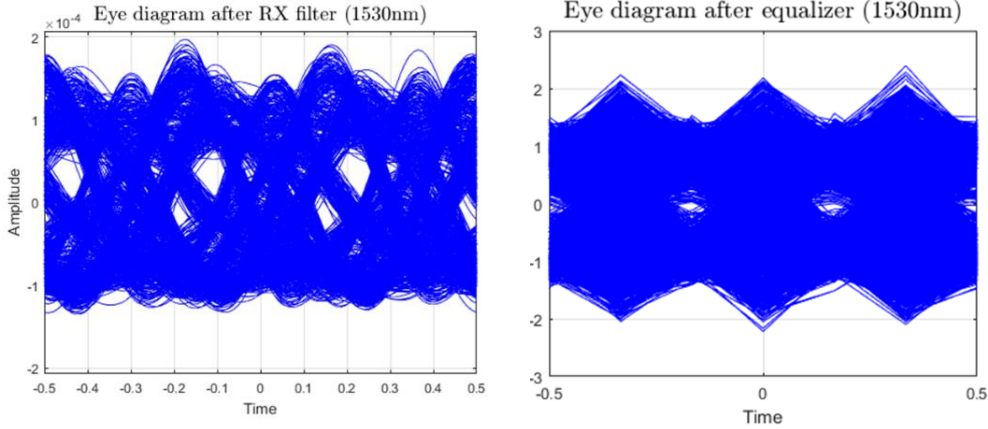


Figure 4.6. Eye diagram comparison before (on the left) and after (on the right) the equalization block for 25Gbps PAM-2 transmission in C-band. After equalization it turns out that $BER \approx 10^{-5}$.

4.3.1 Single-ONU Single-Burst assumption

Our very first analysis of burst-mode equalization uses a pretty simplified approach. A single ONU is considered, from which we only simulate one burst of length N_{TOT} bits. This choice is due to the fact that we want to only focus, for the moment, on the initial transient. The latter, as represented in Figure 4.7, is made up by:

- a training sequence (known a priori) of length N_{TM} bits which is used at receiver side (i.e. at the OLT) for the training phase of the equalizer. At the end of the latter, a tap coefficients set is obtained, whose goodness mainly depends on the training sequence length and on the adaptation rate μ . In a burst-mode situation, N_{TM} should be as low as possible, to reduce the bitrate “waste” in the training phase.
- a very long payload of length N_{DD} bits, used for the decision directed mode of the equalizer, during which the coefficients adjustment keeps going on. For performance evaluation, average MSE and BER are evaluated only over these bits, which in a real system would correspond to the actual user data (i.e. the actual payload).

Denoting y_i as the i -th output sample from the equalizer and x_i as the corresponding transmitted symbol, average MSE is defined as:

$$MSE = \frac{1}{N_{DD}} \sum_{i=1}^{N_{DD}} (y_i - x_i)^2 \quad (4.5)$$

Moreover, in all of the following simulations we use $N_{DD} = 2^{17}$ bits, enough to estimate reliably an average BER of 10^{-3} .

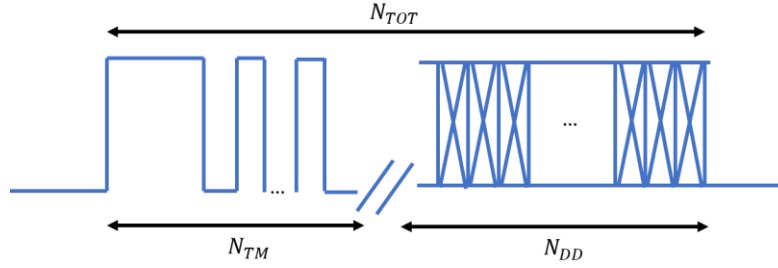


Figure 4.7. Pictorial representation of a N_{TOT} bits long simulated burst: the initial N_{TM} bits are entirely devoted to the training phase of the equalizer, while the last N_{DD} bits (the payload) are used for the tracking phase.

In our first approximation we're basically neglecting all the issues deriving from the presence of different ONUs with different ODN loss and different distance. In other words, we assume to work under the hypothesis of perfect automatic gain control (AGC). Nevertheless, this highly simplified approach will allow us to test the equalizer performance versus some of its main parameters.

4.3.2 Relation between BER and MSE

We should highlight that BER and MSE are relevant performance metrics, but they are not independent. Their relation can be easily derived by starting from the approximated formula for BER computation for a PAM-M modulated signal transmission in AWGN noise:

$$BER \approx \frac{1}{2} \operatorname{erfc} \left(\frac{d_{min}}{2 \cdot \sqrt{2} \cdot \sigma_n} \right) \quad (4.6)$$

in which d_{min} is the minimum distance among adjacent signal levels and σ_n is the noise standard deviation. In particular, we force $d_{min} = 2$ (which is verified on purpose in our simulations¹³) and recall, from Statistical Signal Processing notions, that the noise variance can be estimated as (biased estimator of the variance)¹⁴:

$$\sigma_n^2 = \frac{1}{M} \sum_{i=1}^M (y_i - \bar{y}_i)^2 = \frac{1}{N} \sum_{i=1}^M (y_i - x_i)^2 \quad (4.7)$$

where the last expression is exactly the metric that we denoted as MSE, in which y_i represents the i -th received sample (at the equalizer output), x_i is the corresponding i -th transmitted symbol and M is the number of symbols over which MSE is averaged. By substitution in Eq. 4.6 we obtain the simple approximated expression relating MSE and BER:

$$BER \approx \frac{1}{2} \operatorname{erfc} \left(\sqrt{\frac{1}{2 \cdot MSE}} \right) \quad (4.8)$$

We can easily verify that $BER = 10^{-3}$ translates into an $MSE \approx 0.1$. This equivalence will be useful in the presentation of the following results.

In order to give an idea about the goodness of the approximation, Figure 4.8 reports, in the case of PAM-2 transmission (all of the simulation parameters are kept as specified in Table 4.1), the BER versus ROP curves computed by bit error counting along with the predicted BER values through Eq. 4.8, based on the MSE computed at the equalizer output.

¹³ In fact, in our simulations we assume the transmitted symbol x_i to be in: $\{\pm 1\}$ for PAM-2, $\{\pm 1, \pm 3\}$ for PAM-4 and $\{0, \pm 2\}$ for EDB. As a consequence, for all of the considered formats, it holds $d_{min} = 2$.

¹⁴ We use the zero mean property of the noise which adds up on top of useful signal.

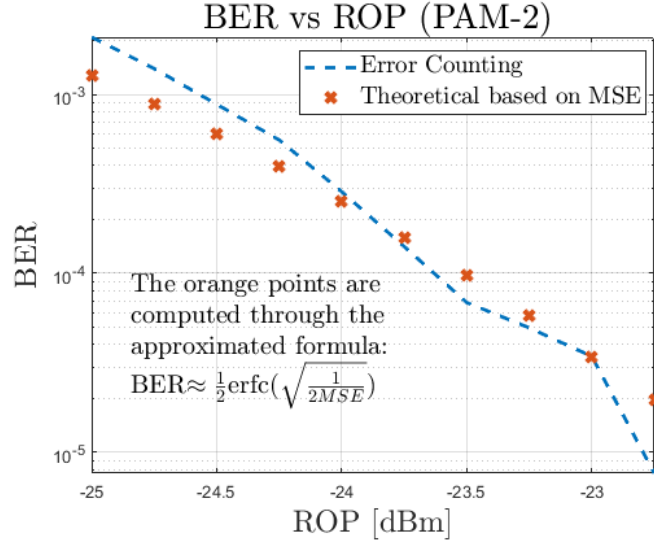


Figure 4.8. BER versus ROP curves for 25Gbps transmission using PAM-2 (all simulation parameters are as specified in Table 4.1). BER is computed both via bit error counting (dashed curve) and by using the approximated formula (Eq. 4.8) based on MSE (orange crosses).

4.4 Step size optimization

As a first task, we investigate how to choose the step size μ for obtaining the best equalization performance. With this purpose in mind, we study the behavior of average BER and average MSE, both computed only over the large payload section of the single simulated burst (see Figure 4.7), as a function of μ and ROP. The training sequence length is firstly fixed to $N_{TM} = 2^{10}$ bits (in Sections 4.4.1 and 4.4.2), then it's varied to verify its impact on step size optimization (Section 4.4.3).

4.4.1 PAM-2 results

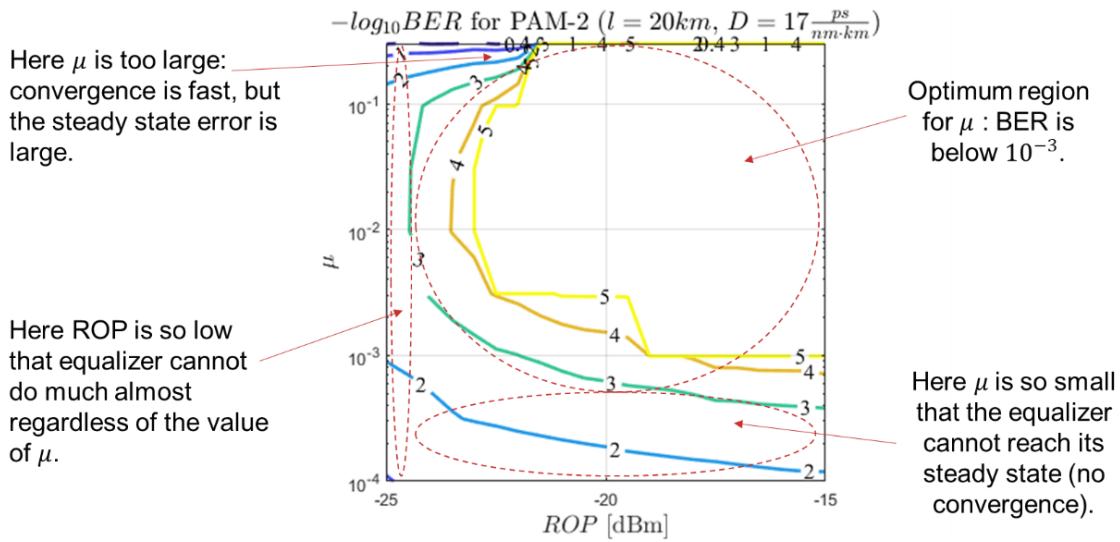


Figure 4.9. $-\log_{10}(BER)$ contour plot for PAM-2 25Gbps transmission over 20km of SSMF using 25G-DML/10G-APD. The training sequence is $N_{TM} = 2^{10}$ bits long. The other simulation parameters are those of Table 4.1. Notes highlighting the main notable areas are reported.

The BER contour plot (actually, for ease of representation, we report its negative logarithm) for PAM-2 is shown in Figure 4.9 for a fiber length of 20 km. In the (ROP, μ) plane we can identify some notable areas, whose presence confirms the observations about μ and convergence rate made above. In particular, an optimum region in which BER is below a certain threshold (e.g. $BER \leq 10^{-3}$) exists. The contour plot can be read in two ways:

- for a given ROP, it provides the optimum μ (or an optimum range for μ). Anyway, the optimum step size value should not be understood as an absolute result. On the contrary, its value strongly depends on the amplitude normalization adopted in the simulation¹⁵. We point out that the optimum range for μ is quite independent on the ROP value, provided that the latter is sufficiently high. For instance, $\mu = 10^{-2}$ seems to be a good choice for a wide range of ROP;
- for a given step size μ , the required ROP for a target BER can be derived. For instance, when $\mu = 0.01$, approximately -24.5dBm of ROP is required for an average BER of 10^{-3} . It's worth to observe that this exact value of $\mu = 0.01$ was used in all of the simulations in Chapter 3 for continuous mode equalization (and actually in “full training mode”, i.e. without tracking phase). In that case, for equal

¹⁵ In our case, the input signal to the equalizer is normalized to its maximum.

conditions (20km in C-band), Figure 3.42 showed a similar value of sensitivity ($< -24\text{dBm}$) for the point $(P_{tx}, ER) = (8.8\text{dBm}, 4\text{dB})$. This agreement proves that using a 1024 bits long training sequence allows performances that are pretty close to the “full training mode” case.

Another relevant aspect is that, for a fixed target BER, it may be that a quite large range of μ exist for which the required ROP is the same (or has very limited penalty). E.g. for $BER = 10^{-3}$, all the values of μ in the interval $[4 \cdot 10^{-3}, 10^{-1}]$ require approximately the same ROP. This offers a degree of freedom in the choice of the step size μ : if convergence rate is an issue, larger μ values in the “feasible” range can be selected.

In Figure 4.10 the same kind of contour plot, under the same conditions, is also reported for average MSE. The contour lines follow quite closely the same behavior as seen for BER: the same considerations as above can be made.

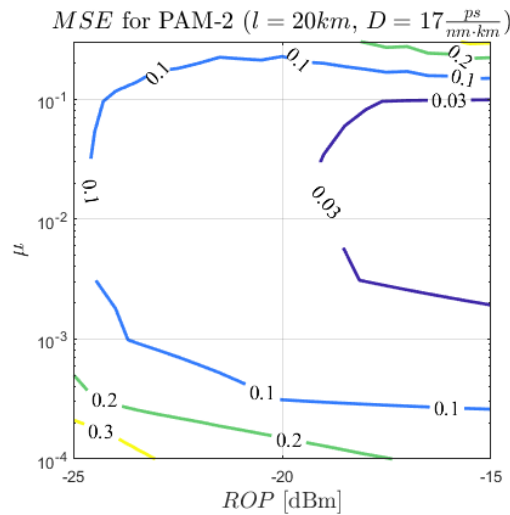


Figure 4.10. MSE contour plot for PAM-2 25Gbps transmission over 20km of SSMF using 25G-DML/10G-APD. The training sequence is $N_{TM} = 2^{10}$ bits long. The other simulation parameters are those of Table 4.1.

In particular, the curve for $MSE=0.1$ in Figure 4.10 approximately delimits the same area as the curve for $BER=10^{-3}$ of Figure 4.9, in agreement with the mathematical relation derived in Section 4.3.2.

We finally point out that the shape of the previously shown contour plots may change with fiber length, due to the different signal distortion caused by different accumulated dispersion and its interaction with chirp (see Chapter 3). Figure 4.11 and Figure 4.12 report, respectively, the BER/MSE contour plots obtained for back-to-

back ($L=0\text{km}$) and 20 km fiber cases. Once again, if we focus on the horizontal line $\mu = 0.01$ in the BER contour plots, the sensitivity values approximately match the ones obtained in Figure 3.42 for “full training mode”.

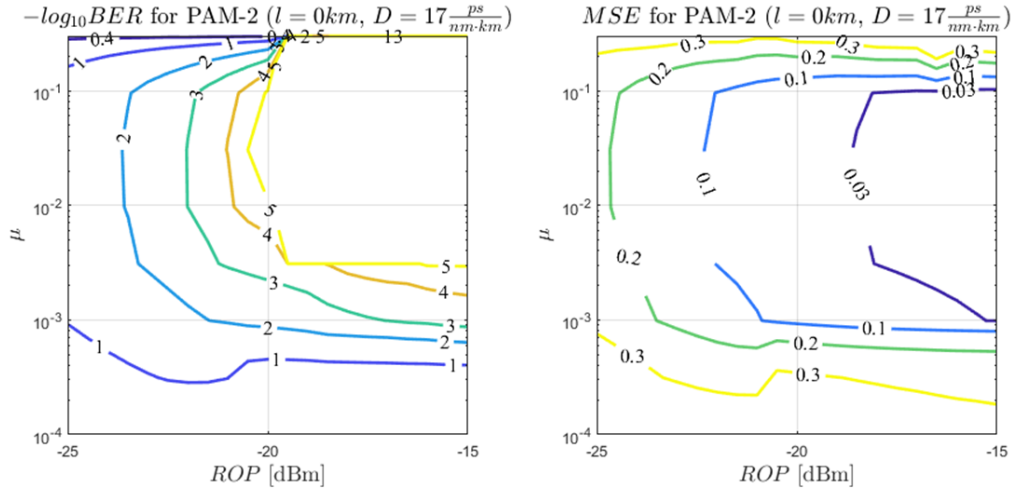


Figure 4.11. BER (on the left) and MSE (on the right) contour plots for PAM-2 25Gbps transmission in back-to-back using 25G-DML/10G-APD. The training sequence is $N_{TM} = 2^{10}$ bits long. The other simulation parameters are those of Table 4.1.

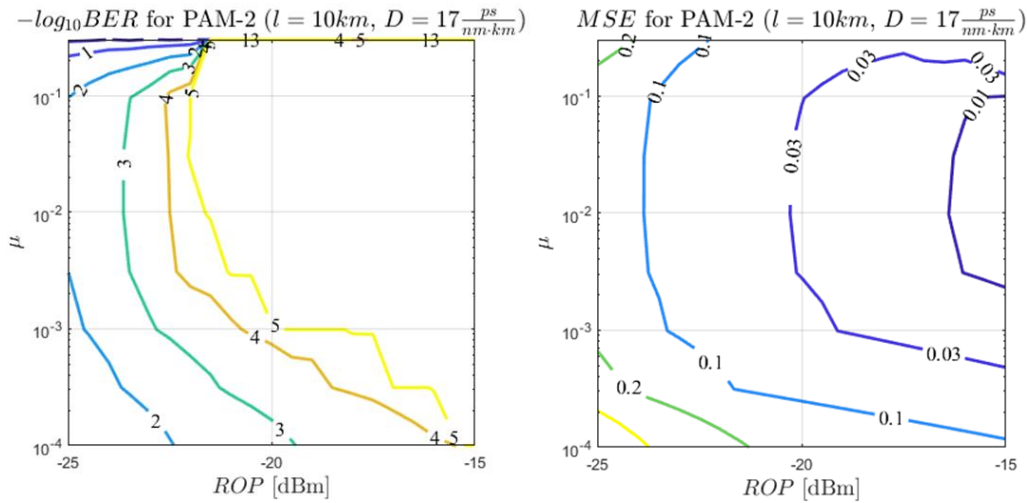


Figure 4.12. BER (on the left) and MSE (on the right) contour plots for PAM-2 25Gbps transmission over 10km of SSMF using 25G-DML/10G-APD. The training sequence is $N_{TM} = 2^{10}$ bits long. The other simulation parameters are those of Table 4.1.

4.4.2 PAM-4 and EDB results

The same analysis as described above has also been performed in the cases of PAM-4 and EDB modulated signals. Figure 4.13 and Figure 4.14 report the BER contour plots for different fiber lengths respectively for PAM-4 and EDB. The MSE curves are omitted for simplicity, indeed we've seen that they have a clear relation with the BER ones.

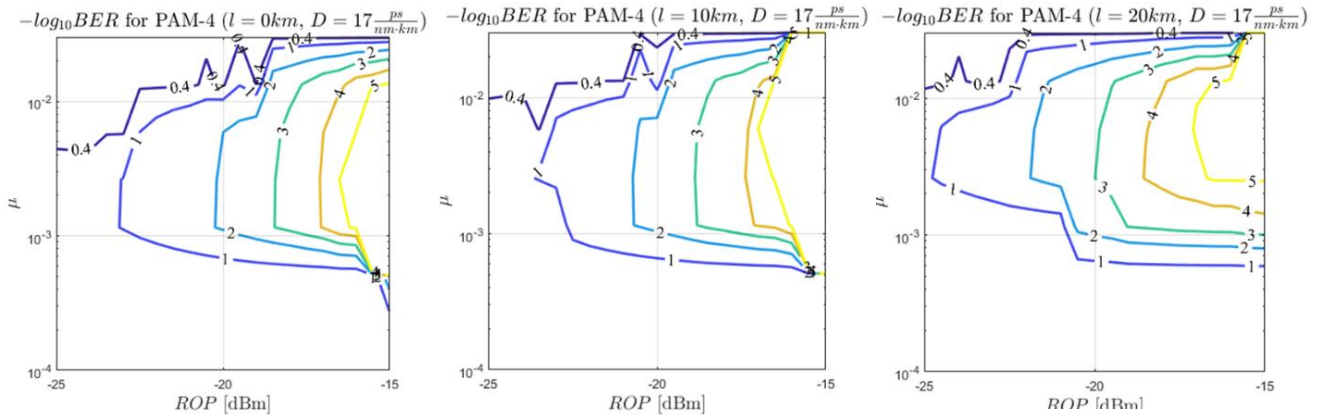


Figure 4.13. BER contour plots for PAM-4 25Gbps transmission in back-to-back (on the left), for 10km (in the middle) and 20km (on the right) fiber lengths using 25G-DML/10G-APD. The training sequence is $N_{TM} = 2^{10}$ bits long. The other simulation parameters are those of Table 4.1.

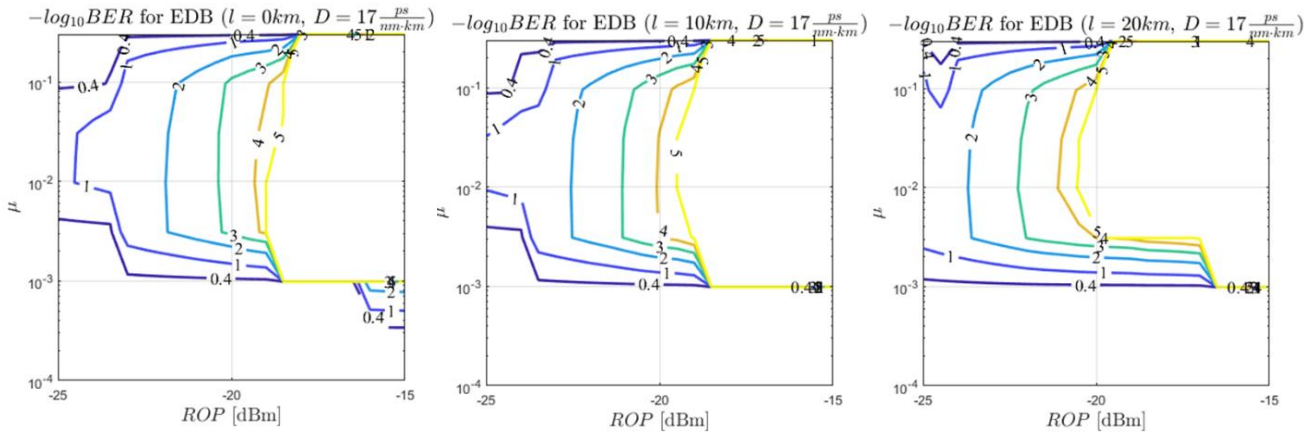


Figure 4.14. BER contour plots for EDB 25Gbps transmission in back-to-back (on the left), for 10km (in the middle) and 20km (on the right) fiber lengths using 25G-DML/10G-APD. The training sequence is $N_{TM} = 2^{10}$ bits long. The other simulation parameters are those of Table 4.1.

We can observe that for all modulation formats, the qualitative behavior of the curves is very similar. The difference lies in the different optimal ranges for μ . For instance, when PAM-4 is used, the step size values

leading to best (smallest) sensitivity values are inside the range of $[10^{-3}, 10^{-2}]$. On the contrary, for both PAM-2 and EDB, best values are in the larger interval $[4 \cdot 10^{-3}, 10^{-1}]$.

4.4.3 The influence of training sequence length

We now begin to study the influence of training sequence length on the choice of the step size μ . Basically, we repeat the simulations of Sections 4.4.1 and 4.4.2 (only for the 20km long SSMF case) for different values of training sequence length. In particular, we choose $N_{TM} = 2^8$ bits and $N_{TM} = 2^9$ bits. We expect that, as the training sequence shortens, the only way to make the equalizer get as close as possible to steady state at the end of its training phase (so as to guarantee a smaller average BER on the payload section) is to choose larger step sizes μ . This is the trend which also emerges from the BER contour plots for PAM-2 reported in Figure 4.15, which can also be compared to the plot in Figure 4.9, which instead used $N_{TM} = 2^{10}$ bits. It happens that the shorter is the training sequence, the smaller becomes the optimum region, concentrated around bigger values of μ .

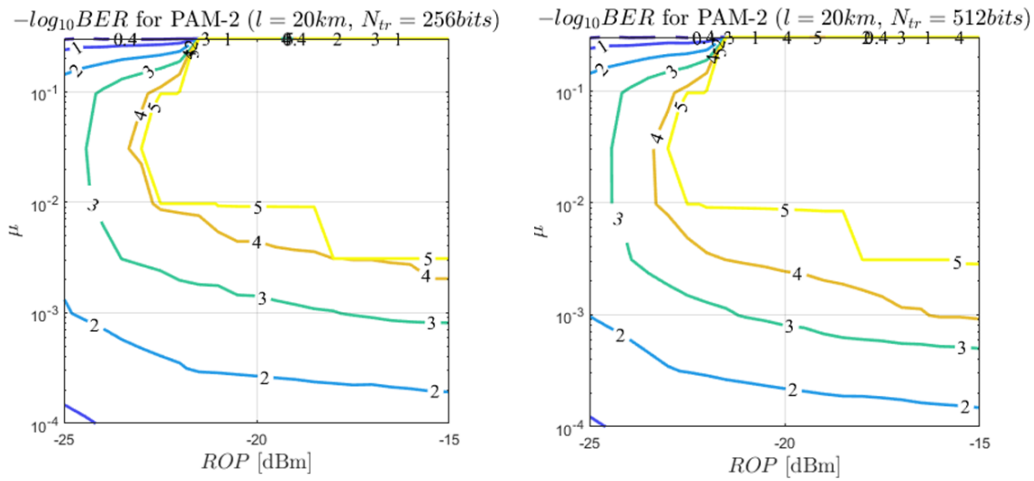


Figure 4.15. BER contour plots for PAM-2 25Gbps transmission (25G-DML/10G-APD) over 20km of SSMF, when a training sequence is used whose length is 256 bits (on the left) and 512 bits (on the right). The other simulation parameters are those of Table 4.1.

The same behavior can be observed in case of PAM-4 (in Figure 4.16) and EDB (Figure 4.17).

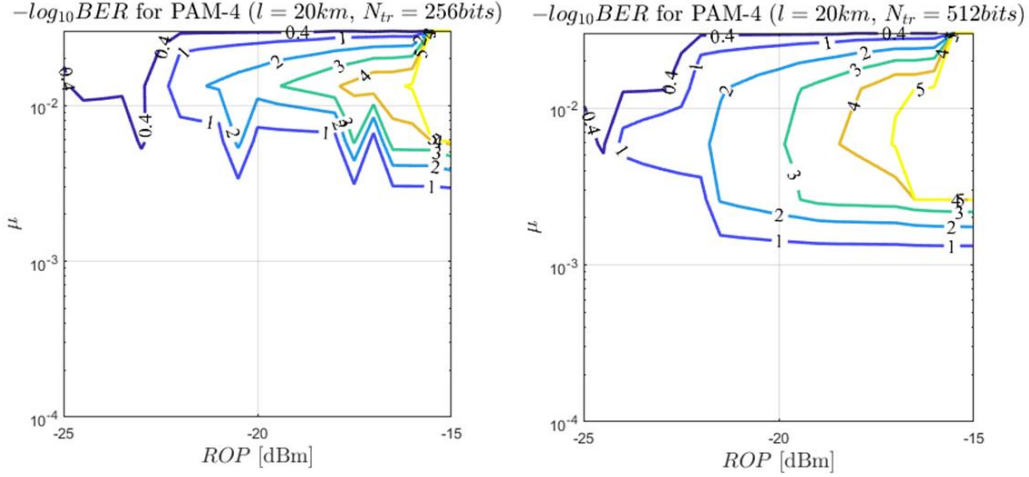


Figure 4.16. BER contour plots for PAM-4 25Gbps transmission (25G-DML/10G-APD) over 20km of SSMF, when a training sequence is used whose length is 256 bits (on the left) and 512 bits (on the right). The other simulation parameters are those of Table 4.1.

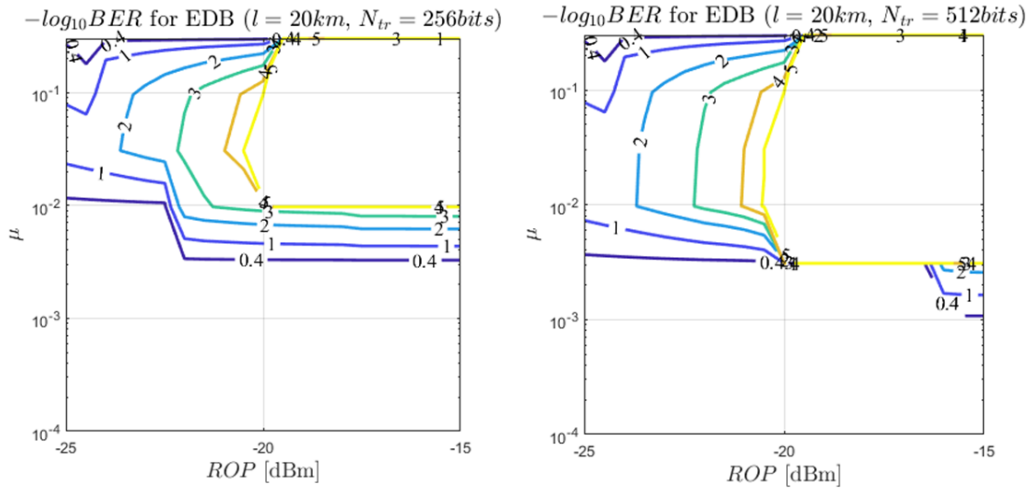


Figure 4.17. BER contour plots for EDB 25Gbps transmission (25G-DML/10G-APD) over 20km of SSMF, when a training sequence is used whose length is 256 bits (on the left) and 512 bits (on the right). The other simulation parameters are those of Table 4.1.

4.5 Initial coefficients optimization

All of the previous simulations in this Chapter were assuming an “all-zeros” initial state for the equalizer coefficients, as introduced previously in Eq. 4.4. We know from theory that the initial state is utterly arbitrary and thus it represents another degree of freedom for performance optimization. In particular, we wonder if a particular tap coefficients state exists for which the equalizer convergence is reached earlier, i.e. with less required training bits. An improved convergence rate is for sure a desirable feature, since it would reduce the overhead

and increase the data transmission efficiency in an actual deployment. Several attempts in this direction have also been presented in the literature: for instance, in [36] a triangular initial state is proposed.

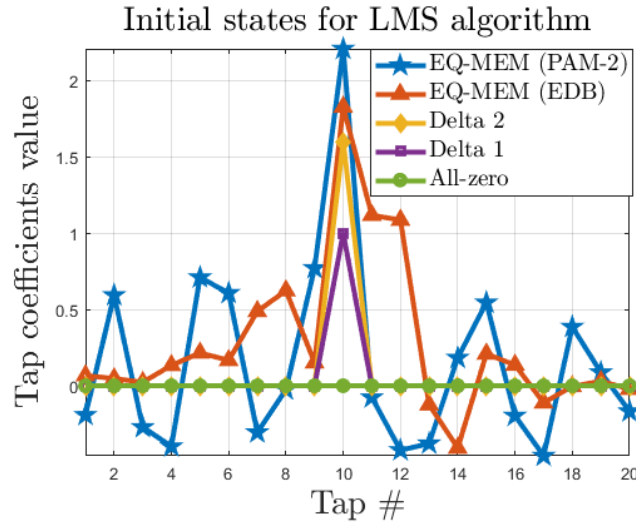


Figure 4.18. Graphical representation of the considered initial tap coefficient states.

In order to tackle this issue, we study the behavior of average MSE and average BER (averaged on the full 2^{17} bits long payload) versus training sequence lengths for several different initial tap states (Figure 4.18) that we denote as:

- “all-zero” state, as defined in Eq. 4.4;
- “delta 1” case, consisting in all coefficients set to zero, except for the middle tap, which is instead set to 1. The reason for such a heuristic criterion is based on the fact that it is very likely that the sample on the FIR middle tap is the one which is going to impact more on the correct current decision, being it related to current received symbol;
- “delta 2” case, consisting in all null coefficients, except for the middle one, which is instead set to an optimized (obtained via preliminary simulations) value (in our case and with our normalizations, we use 1.6);
- “memory” case (denoted as EQ-MEM strategy in the following), consisting in the adoption of a memorized (stored in a memory) set of coefficients inherited from the previous burst from the same

ONU or simply pre-computed during a preliminary phase (e.g. a full-training burst sent during the ranging operations of a PON). This approach has been recently proposed in the literature [43] and will be one of the key points in our following discussion.

For PAM-2 we fixed fiber length $L=20$ km, $\mu=0.01$ and $ROP=-22$ dBm. In these conditions, we already know from Figure 4.15 that, for more than 256 training bits, an average BER below 10^{-4} is ensured, at least when the “all-zero” initial taps state is forced. The results for PAM-2 reported in Figure 4.19 agree with expectations. Moreover, they clearly show that, from a convergence rate point of view, the best coefficient initialization strategy is by far the EQ-MEM, followed by the “delta-2”, the “delta-1” and, finally, by the “all-zero” state. In the curves of Figure 4.19 the EQ-MEM case is the only one yielding minimum MSE and BER even with a reduced (or even null) amount of bits, at the cost of storing in a memory a set of coefficients for each ONU in the PON. The “delta” cases, instead, seem particularly interesting since the improvement in convergence rate they introduce w.r.t. the “all-zero” case comes for free: setting the middle coefficient to a non-null value is absolutely a costless operation. In particular, the “delta-2” case leads to $BER = 10^{-5}$ with less than 100 bits, versus the about 300 bits required by a “delta-1” and the more than 400 bits required by an “all-zero” approach. Definitely, if convergence speed is an issue, “all-zero” is not the most valid option to be considered.

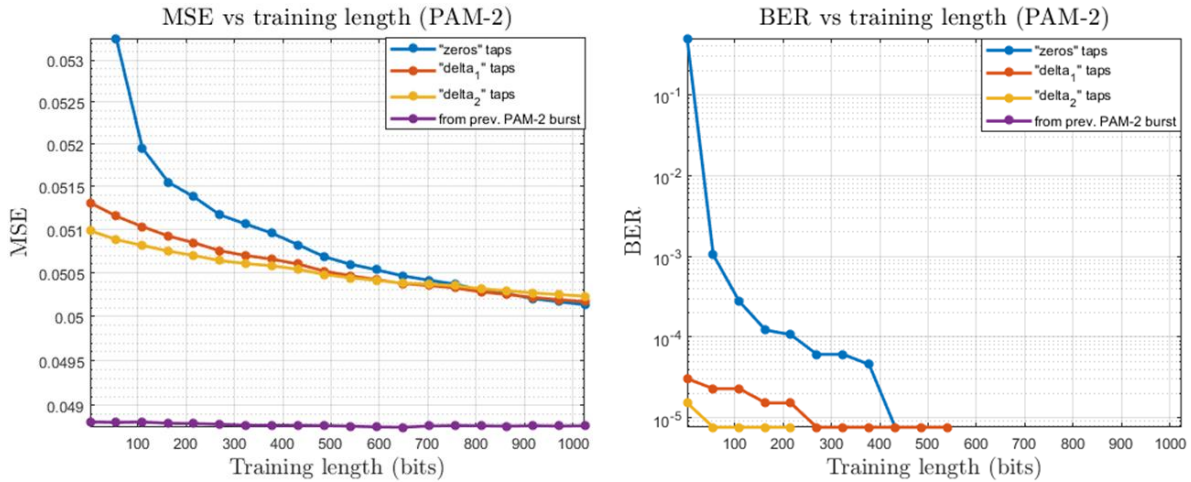


Figure 4.19. Average (on the payload) MSE (on the left) and BER (on the right) versus training sequence length for PAM-2 25Gbps transmission (25G-DML/10G-APD). In the plot on the right, the BER curve (in purple) corresponding to the EQ-MEM equalization strategy is not visible due to the adopted logarithmic scale: actually, for any value of training sequence length, no errors are counted.

For EDB we fixed fiber length $L=20$ km, $\mu=0.01$ and $ROP=-20$ dBm. For the EDB results in Figure 4.20 the same considerations as above hold. Among memory-less approaches, the “delta-2” case is again the fastest one. Once again, instead, the “memory” approach seems to show that it’s possible to get rid of a training phase.

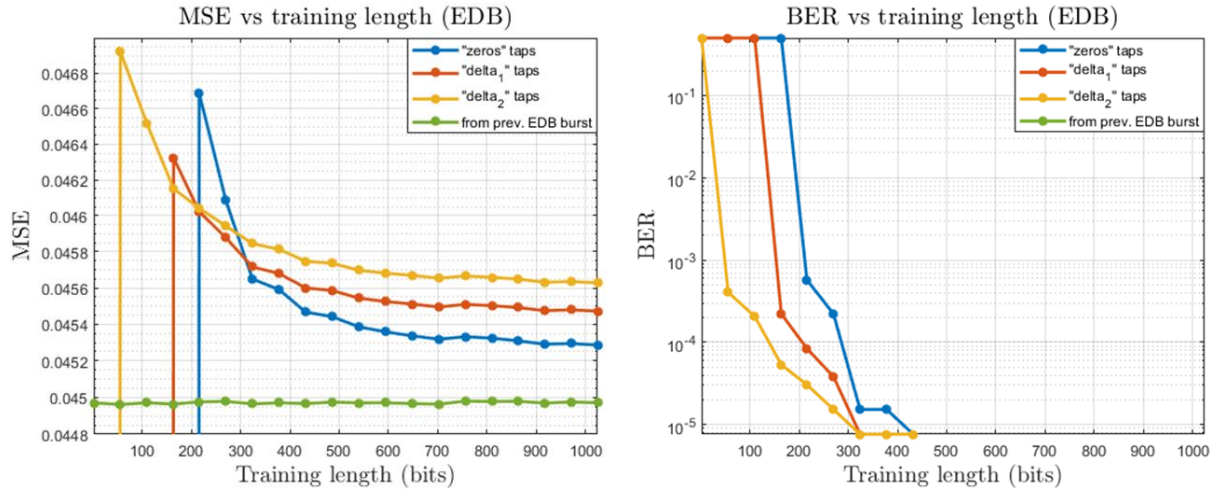


Figure 4.20. Average (on the payload) MSE (on the left) and BER (on the right) versus training sequence length for EDB 25Gbps transmission (25G-DML/10G-APD). The initial outlier values in the MSE plot (on orange, red and blue curve) are fictitious. In the plot on the right, the BER curve (in green) corresponding to the EQ-MEM equalization strategy is not visible due to the adopted logarithmic scale: actually, for any value of training sequence length, no errors are counted.

Nevertheless, we should be very careful in interpreting these kinds of results. The performance metrics (BER and MSE) used above are averaged on a very large payload (2^{17} bits long). From a performance analysis point of view, they are actually misleading, since they do not take into account the temporal evolution of the error rate. For instance, in the considered cases, during the payload reception, it is likely that most of the errors are concentrated at the beginning (right after the training phase of the equalizer). Indeed, during the tracking phase, the tap coefficients keep evolving, leading, hopefully, to a decreased amount of errors (smaller “instantaneous error rate”) toward the end of the payload. If we chose a particular value of training sequence length simply based on the results of Figure 4.19 and Figure 4.20 we could fall into a situation in which the training phase is not able to provide a sufficiently¹⁶ small instantaneous error rate since the very beginning of the payload. In addition, the fact that, in a PON, frames may be of very small size further accentuates the problem. In the following of this Chapter we will try to follow the evolution of the “instantaneous error rate” and “instantaneous

¹⁶ An error rate under a certain threshold is required, in order to make the FEC algorithm works.

MSE” over time, in order to draw meaningful conclusions about the best choices for training sequence length and initial taps state.

4.6 Evolution of local MSE over time

We define a “Local MSE” as a moving average of the squared error e^2 (with e defined as in Section 4.2) over a sliding window of size $N_{win} = 100$ bits¹⁷. It’s worth noticing that a relatively small temporal window corresponding to 100 bits would not be statistically enough for estimating reliably a BER. Indeed, as a rule of thumb, a reliable BER estimation for a target BER_t would require a bit error counting over a number of bits N_{bits} satisfying the relation:

$$N_{bits} \geq \frac{10}{BER_t}, \quad (4.9)$$

which is not verified, if we choose $N_{bits} = N_{win} = 100$ and $BER_t = 10^{-3}$. For this reason, in this Section, we’re only aiming at tracking the evolution over time of what we called “instantaneous” (or “local”) MSE.

The results for PAM-2 (all simulation parameters are kept as in Section 4.5) are reported in the plots of Figure 4.21 (for “all zero” case) and Figure 4.22 (for “delta” cases): for each of the three memory-less taps initialization strategies we represent the temporal evolution of the above defined local MSE for 3 different values of training sequence length (32, 64 and 256 bits). A first important observation is that, in all cases, the local MSE (which is related to the instantaneous error rate) keeps decreasing even during the tracking mode operation of the equalizer. This proves our concerns about the incompleteness of an approach which is only based on average MSE/BER (see Section 4.5). Moreover, for a non-optimized taps initialization strategy such as the “all-zero”, it happens that the rate of convergence to a low local MSE may quite strongly depend on the training sequence length adopted (Figure 4.21). On the contrary, the “delta” initialization approaches prove to be able to tolerate very small training sequence lengths (curves in Figure 4.22 are superimposed). Nevertheless, operating with fewer training bits would expose the payload, at least in its initial part, to very frequent errors which may unavoidably lead to unwanted packet drops. The choice of the most suitable training length is thus a trade-off:

¹⁷ The choice of a suitable value for N_{win} is actually a trade-off between the ability to track MSE variations over time (from this point of view, the smaller N_{win} the better) and the variance of the sliding window estimator (the bigger N_{win} , the smaller is the variance of the Local MSE, which will show smaller fluctuations).

- the training phase must be sufficiently long to lead the instantaneous MSE below a given threshold (determined by the adopted FEC technique), where it will lie for the whole subsequent tracking phase;
- at the same time, the shorter is the training sequence, the smaller the introduced overhead. Optimized coefficient initialization strategies help us to move in this direction: the “delta-2” approach in the right part of Figure 4.22 proves to get local MSE<0.1 earlier than other approaches.

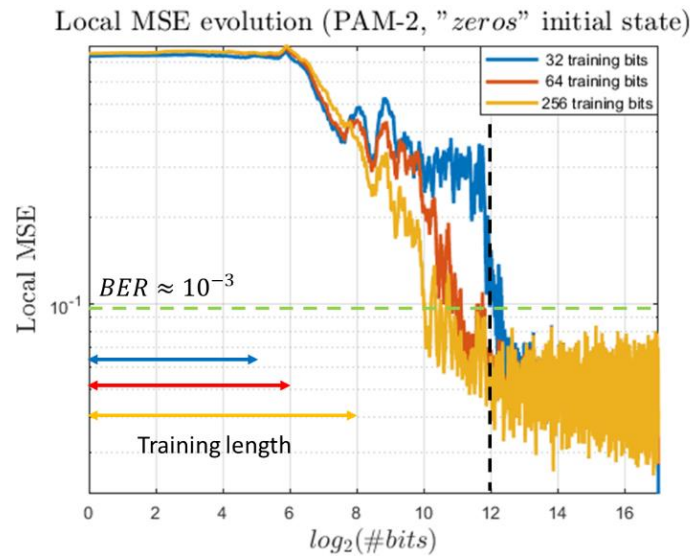


Figure 4.21. Local MSE temporal evolution (PAM-2, ROP=-22dBm) for different training sequence lengths. Initial state is “all-zero”. The simulation parameters are those of Table 4.1.

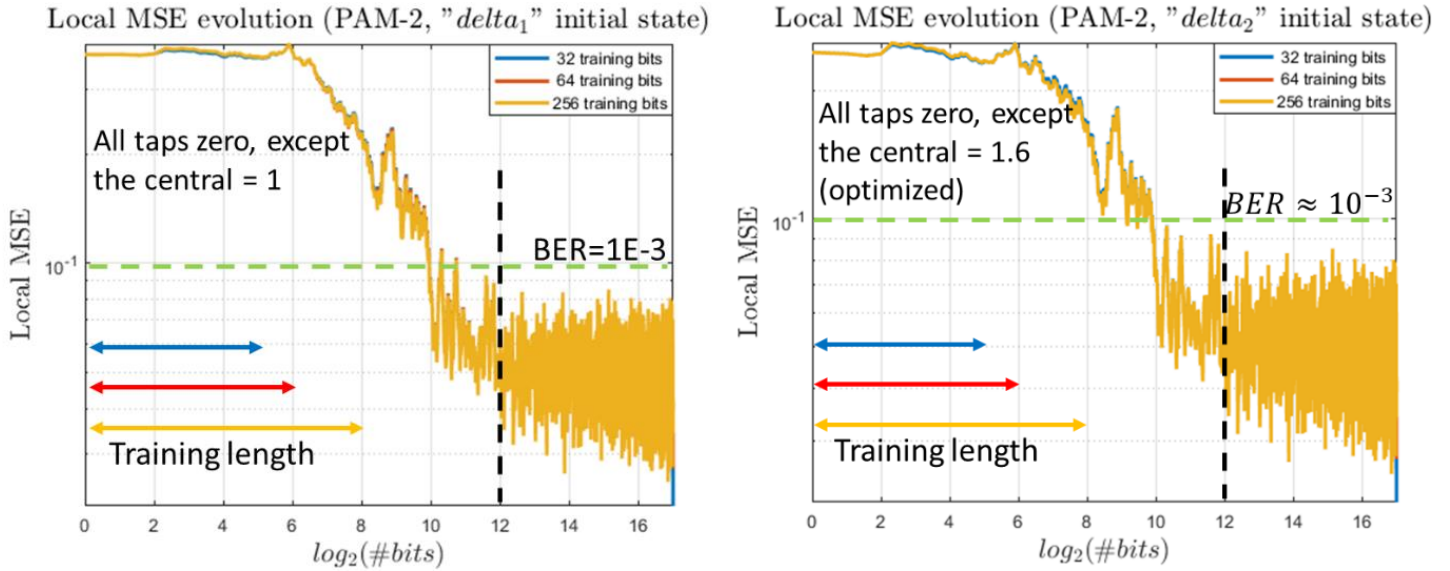


Figure 4.22. Local MSE temporal evolution (PAM-2, ROP=-22dBm) for different training sequence lengths. Initial states are “delta_1” (on the left) and “delta_2” (on the right). The simulation parameters are those of Table 4.1.

Another way to show these results is reported in Figure 4.23, in which, for a fixed training sequence length, the performances of all of the 4 considered taps initialization strategies are compared on the same plot. The clear winner is the EQ-MEM: the transient phase is completely removed¹⁸. The same kind of plots are also reported for a smaller ROP in Figure 4.24. In particular, we set ROP=-24.5dBm so that, according to Figure 4.15, we expect a steady state BER around 10^{-3} . The results agree with intuition and, indeed, we can notice a steady state MSE oscillating around 0.1, which roughly corresponds to $BER = 10^{-3}$. Besides the different steady state value, basically, all of the previous considerations hold. Moreover, Figure 4.24 also shows the performance of a “memory” approach that makes use of taps coefficients from the end of the training phase of previous burst. This is intuitively worse than an approach using coefficients from the very end of previous burst (i.e. after training + tracking), since it does not exploit the further taps adjustment occurred during the tracking phase (see Figure 4.25).

¹⁸ Anyway, we should further investigate in order to understand whether the training phase can be completely removed, too. We'll do it in next sections, by keeping into account the instantaneous BER.

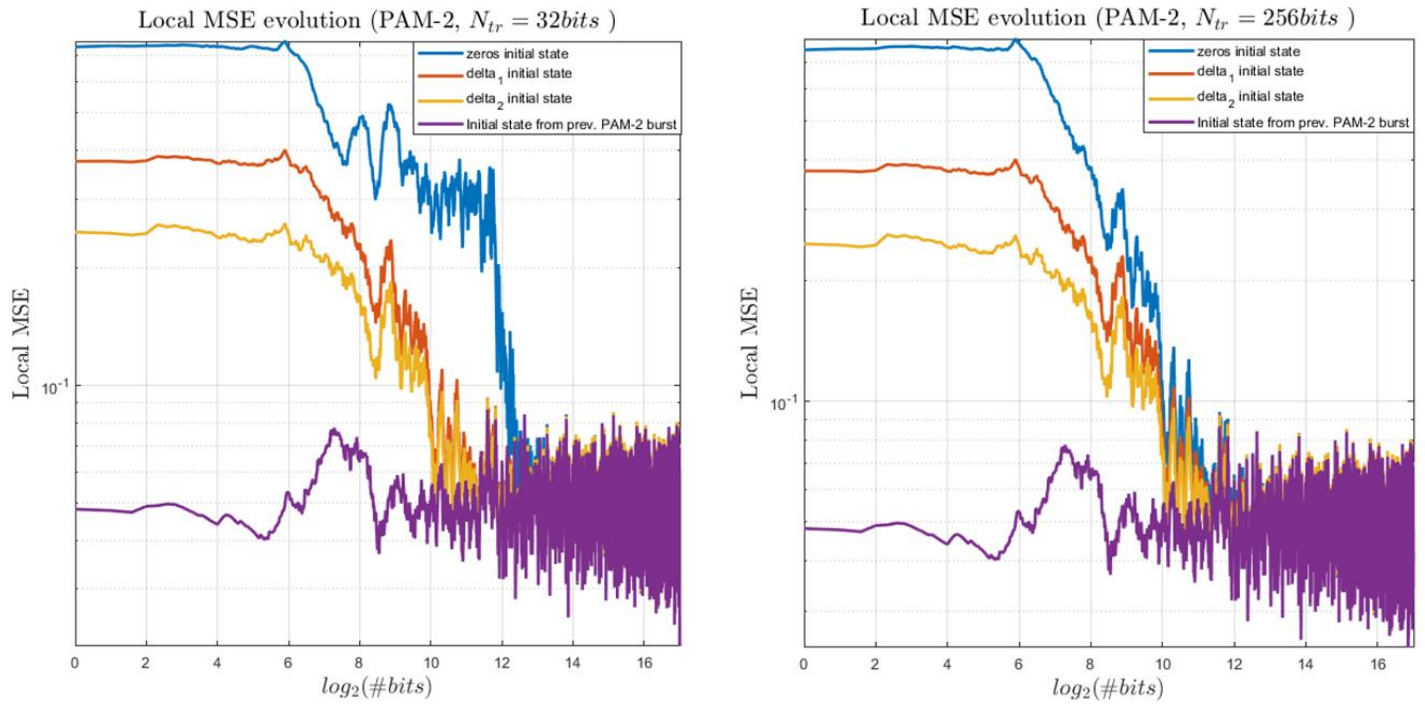


Figure 4.23. Local MSE temporal evolution (PAM-2, ROP=-22dBm) for different taps initialization approaches. Training sequence lengths are 32 bits (on the left) and 256 bits (on the right). The simulation parameters are those of Table 4.1.

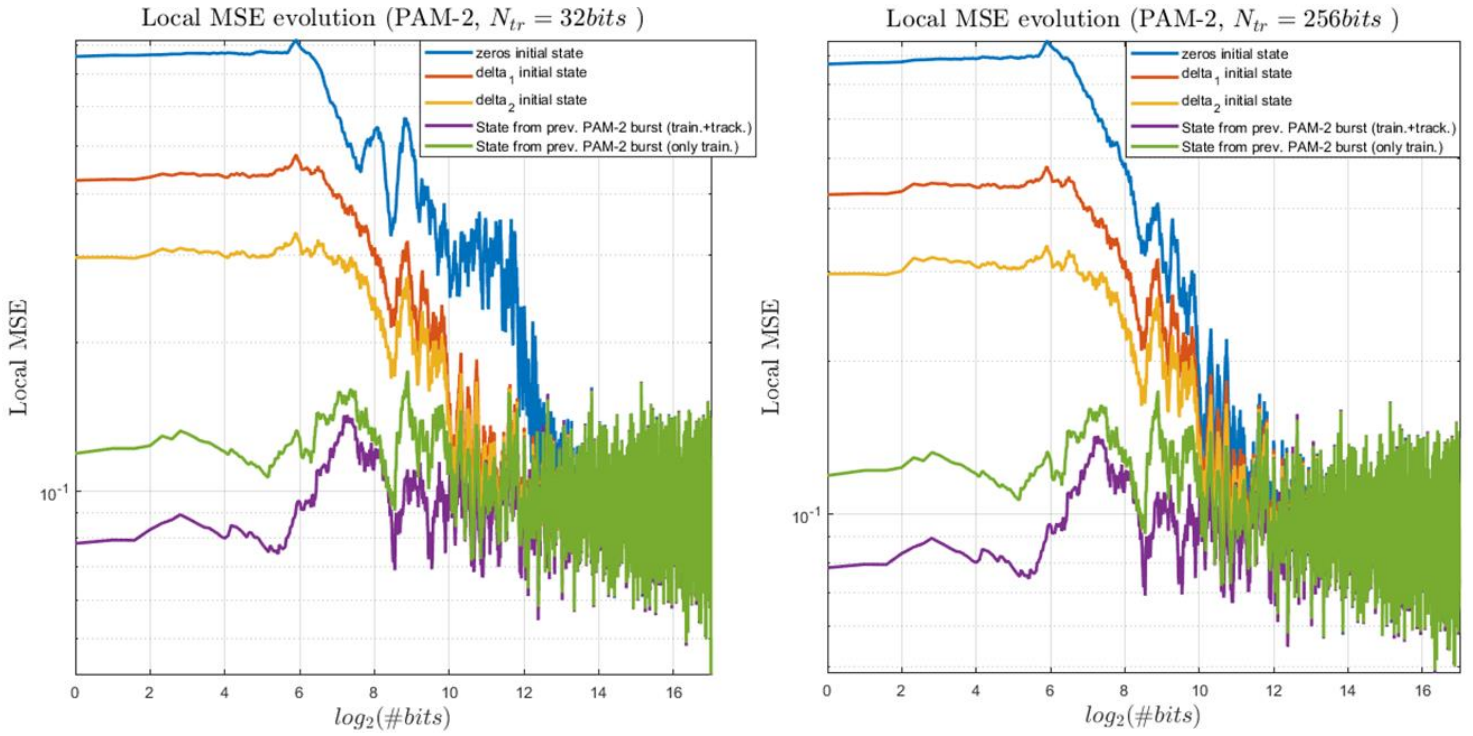


Figure 4.24. Local MSE temporal evolution (PAM-2, ROP=-24.5dBm) for different taps initialization approaches. Training sequence lengths are 32 bits (on the left) and 256 bits (on the right). The simulation parameters are those of Table 4.1.

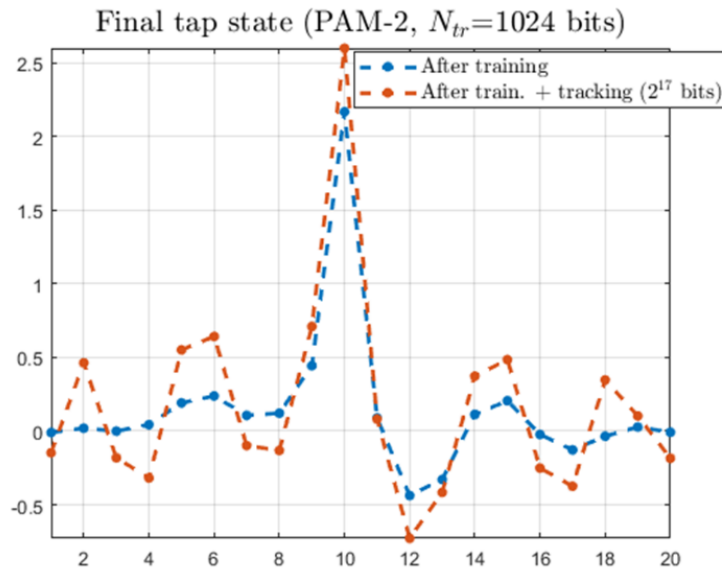


Figure 4.25. Taps state comparison for PAM-2 after training phase (orange curve) and after training + tracking (blue curve). The simulation parameters are those of Table 4.1.

The analysis has also been extended to EDB format. The local MSE curves for different tap initialization strategies are reported for the 256 training bits case (all simulation parameters are kept as in Section 4.5 for EDB) in Figure 4.26. The EQ-MEM case is still the best performing one, provided that the memorized coefficients come from a previous burst adopting the same modulation format. It turns out, indeed, that the final coefficients at the end of a burst (training + tracking) have a different shape depending on the modulation format adopted (see Figure 4.27). Nevertheless, it emerges that the convergence rate performances of the different equalization strategies are independent on the particular modulation format used. For this reason, in the rest of the work, we will only choose one format (specifically, EDB) to make further considerations about burst-mode equalization.

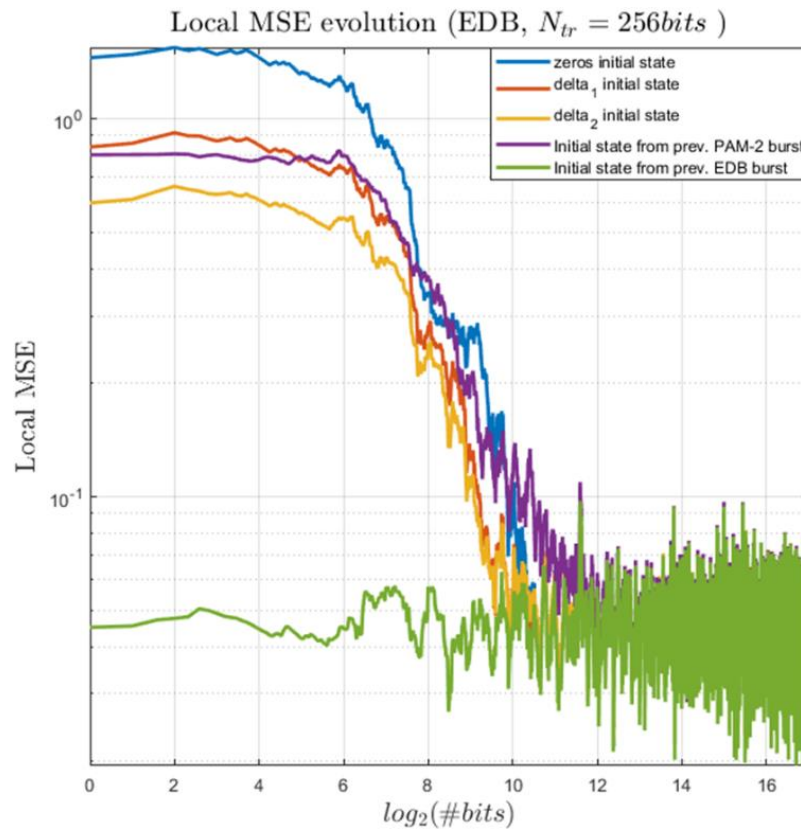


Figure 4.26. Local MSE temporal evolution (EDB, ROP=-20dBm) for different taps initialization approaches. Training sequence length is 256 bits. The simulation parameters are those of Table 4.1.

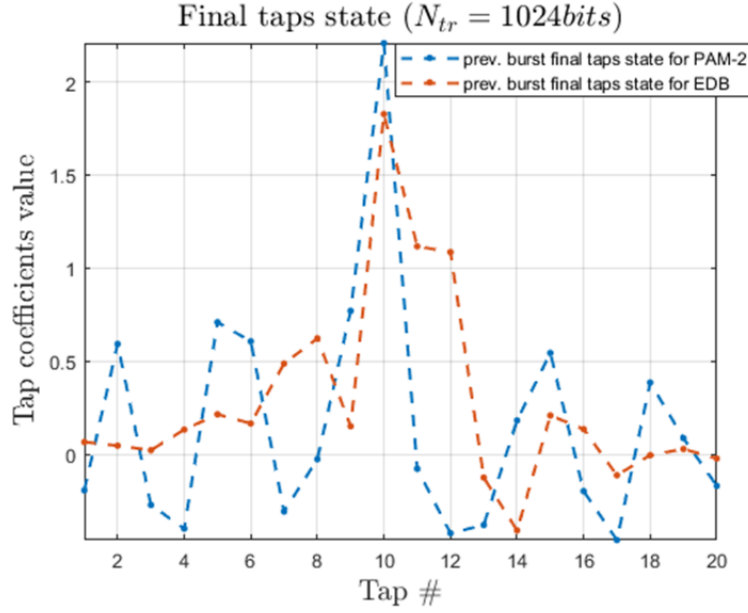


Figure 4.27. Taps state comparison for PAM-2 (blue curve) and EDB (orange curve) after training + tracking. The simulation parameters are those of Table 4.1.

4.7 Evolution of local BER over time

The same considerations as obtained in Section 4.6 for local MSE could be repeated in terms of BER. Anyway, in order to track the evolution of BER along the payload we need to define a way to measure a local BER (or “fine time-resolved BER”) with sufficient accuracy. We proceed as follows:

- We simulate the transmission of B bursts of equal length (precisely, each with a payload of 2^{17} bits) from the same ONU;
- We split each burst into T time slots (or “time windows”) of 256 bits each;
- We perform bit error counting over each time window. Within the same time window, local BER is computed by accumulating the errors over B different bursts. In this way, by properly setting the number of bursts B (and/or the number of bits in a time window), the local BER can be easily estimated with any desired degree of accuracy.

The pictorial representation of the latter procedure is reported in Figure 4.28.

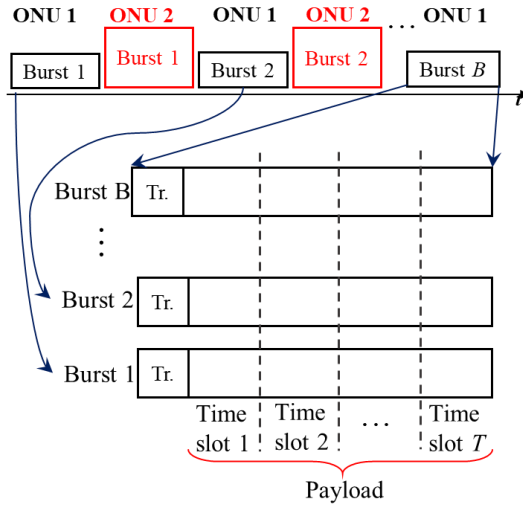


Figure 4.28. Procedure for local BER evaluation.

In this multiple-bursts scenario, the difference between a memory-less (e.g. the “all-zeros” and the 2 “delta” approaches) and a memory-aided (e.g. the EQ-MEM) taps initialization strategy is exemplified in Figure 4.29.

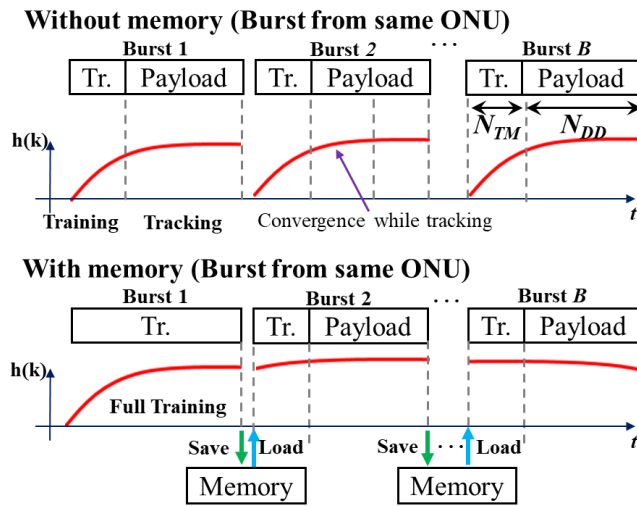


Figure 4.29. Exemplified taps evolution in memory-less (on the top) and memory-aided (on the bottom) multiple bursts equalization strategies.

We choose, as a point of operation for the simulated DML/DD system, a point in the middle of the overall feasible region from 0-20 km for EDB, according to Figure 3.44. In particular, we choose $ER = 6dB$ and $P_{tx} = 8.5dBm$. Moreover, we select $ROP = -23dBm$ (corresponding to a power budget of $31.5dB$), which would

approximately result into a $BER = 10^{-3}$ in continuous mode transmission. The above explained procedure is applied (using $B = 400$ bursts): local BER evaluation over the first 20 time slots is reported (for different values of training sequence length N_{TM}) in Figure 4.30 for the EQ-MEM case (plot on the left) and the “delta 2” case, chosen as representative of the memory-less equalization approaches (on the right). Figure 4.30 shows that, if the number of bits devoted to training is less than 2600, a memory-less approach is not able to provide $BER < 10^{-3}$ since the very beginning of the payload. On the contrary, a memory-aided equalization approach such as EQ-MEM, is able to get rid of the training phase, at the cost of pre-calculating the correct taps coefficient (e.g. by spending a full-training initial burst at the beginning of operation) for each ONU and storing them in a memory. These results are pretty relevant and will be further corroborated by experiments in Chapter 5. In particular, Figure 4.30 shows that our previous “doubts” on the use of an averaged BER on the full payload are well-founded: the right plot clearly shows that a very important transient in the time-resolved BER is still happening in the first part of the payload.

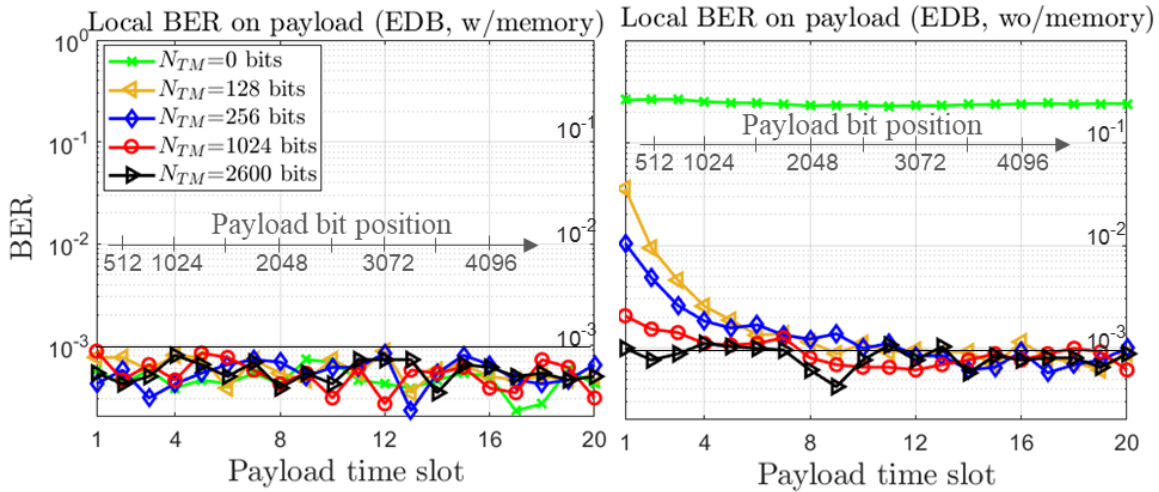


Figure 4.30. Local BER temporal evolution (EDB) for different training sequence lengths N_{TM} and different taps initialization approaches: EQ-MEM (on the left) and memory-less “delta 2” (on the right). The simulation parameters are those of Table 4.1.

4.8 Conclusions

In this Chapter we discussed the requirements for burst-mode adaptive equalization in the US channel of a PON. We focused on the LMS algorithm for tap coefficient adaptation and the optimization of its main parameters (step size μ , training sequence length N_{TM} , initial tap state...). We demonstrated that a performance analysis based on average BER (and/or average MSE) over a large payload may lead to erroneous conclusions.

We finally highlighted, based on carefully defined performance metrics (local MSE and local BER), the advantages of a memory-aided equalization approach compared to a memory-less one.

Chapter 5: Experimental results on burst-mode equalization

This Chapter aims at providing an experimental demonstration of the upstream burst-mode equalization strategies exposed and investigated by simulations in Chapter 4. In particular, the focus is on the local BER evolution over time by using the same approach adopted in Section 4.7. The experimental setup is introduced (Section 5.1), then the results are presented and discussed (Section 5.2). The conclusions are drawn in Section 5.3. We point out that a paper on this topic, including all of the results from this Chapter (and some from Chapter 4), was submitted in October 2018 to the main Conference of the field (OFC2019).

5.1 Experimental setup

The same experimental setup as described in [44] has been employed, along with the use of EDB modulation format¹⁹. Mainly due to optoelectronic components availability in the laboratory, an externally modulated laser (by a MZM) has been used, in place of the DML used in the Chapter 4 simulations. The complete setup is depicted in Figure 5.1.

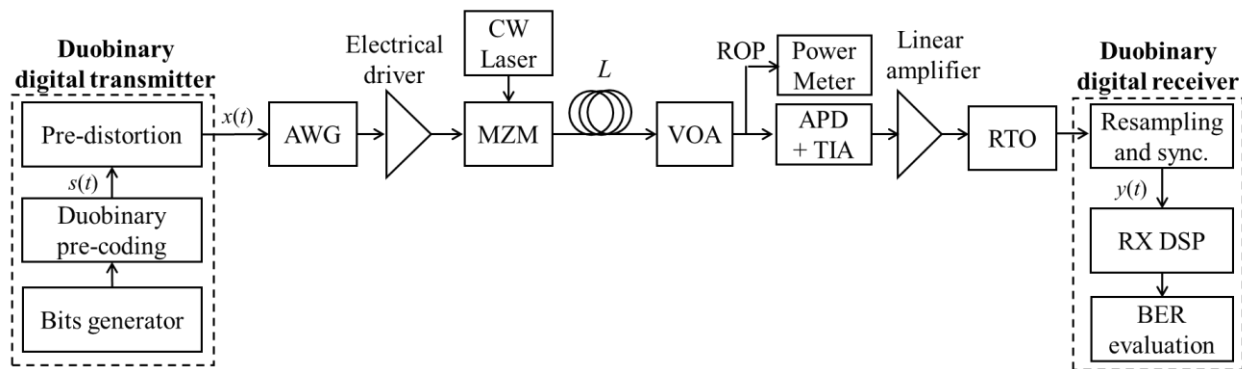


Figure 5.1. Experimental setup adopted for the experiments on burst-mode equalization.

A sequence of 2^{17} bits is generated (bitrate $R_b = 25Gbps$), pre-coded (for Duobinary signaling) and pre-distorted (to compensate for the MZM non-linear response) within the duobinary digital transmitter, implemented in MATLAB. The resulting digital signal $x(t)$ is sent to a 92 GSamples/s²⁰ Arbitrary Waveform

¹⁹ The EDB approach considered here is the one which uses a three-level signal as training sequence for equalization (denoted as EDB1 in [42]),

²⁰ The number of Samples/s is fixed by the AWG. Different bitrate values can be obtained by properly tuning the number of Samples/symbol in the duobinary digital transmitter.

Generator (AWG), which converts it into an analog signal. The latter serves as driving voltage for the MZM, which also receives the CW laser signal. The SSMF has a length of $L = 20\text{km}$ and it is operated in C-band. A Variable Optical Attenuator (VOA) is then used in order to set the ROP at receiver input to the desired level: in particular, we select $ROP = -19.3\text{dBm}$, which was proven to result in $BER = 10^{-3}$ for a continuous-mode transmission, as indicated in [44]. The receiver is made up by a commercial 10Gbps APD followed by a trans-impedance amplifier. After the amplification stage, the electrical signal is input into a Real Time Oscilloscope (RTO) working at a sampling rate of 100 GSamples/s. Then, the received samples are stored and processed offline by using the duobinary digital receiver implemented in MATLAB. In the offline processing, the received signal undergoes a resampling to 2 Samples/symbol and a correlation-based synchronization to the pilot sequence, before being sent to a 20 taps FFE operating at 2 Samples/symbol and using LMS algorithm for tap coefficients updating. Finally, the BER is evaluated by error counting over the received payload bits.

5.2 Results

In the following experimental results we're going to show that the received signal can be either interpreted as a single long burst or as the concatenation of many different short bursts from the same ONU²¹. The two different approaches may lead to different conclusions. A careful analysis is required to understand how to properly interpret the results.

5.2.1 Single burst analysis

We here use a single burst analysis to make convergence rate considerations. We already showed by simulations (Chapter 4) that this approach is actually misleading, but now we try to replicate it experimentally. Basically, we consider a relatively long single burst with training sequence length N_{TM} (variable) and a fixed payload size $N_{DD} = 2^{15}$ bits. The received signal is processed several times, using different training sequence lengths N_{TM} in the training phase of the equalizer. At each iteration, the BER is computed over the whole payload. The experimental curves of BER versus training length are reported in Figure 5.2 for 3 different coefficient-initialization strategies: the "all-zeros", the "delta" with optimized central value (the one that we called "delta 2" in Chapter 4) and the approach using memory from previous bursts (EQ-MEM). It can be noticed that the only strategy allowing to get rid of the training sequence is the EQ-MEM. Anyway, by just looking at Figure 5.2, we would be tempted to conclude that the memory-less approaches would also guarantee equalizer convergence

²¹ As done in Chapter 4, still the AGC is assumed to be perfect. Moreover, in the multiple burst approach we assume all bursts to come from the same ONU and thus have the same amplitude.

provided that $N_{TM} > 500 \text{ bits}$ (actually, for the delta case, $N_{TM} \sim 200 \text{ bits}$ is enough to provide a BER below 10^{-3}).

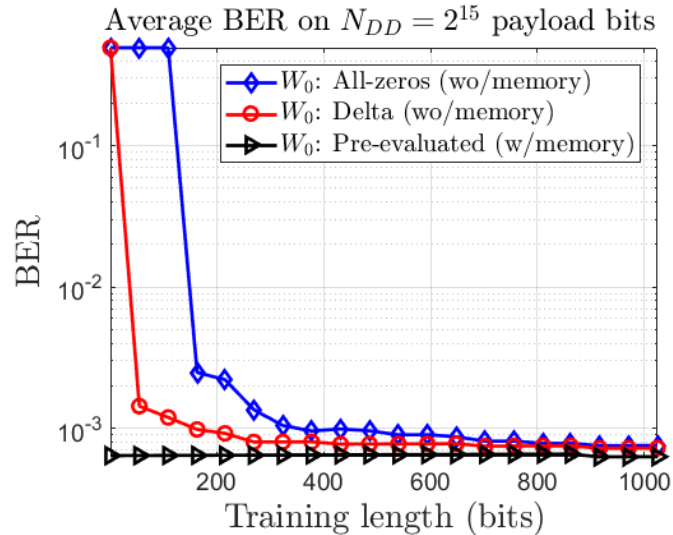


Figure 5.2. Average BER (computed over $N_{DD} = 2^{15}$ payload bits) versus training sequence length N_{TM} .

5.2.2 Multi-bursts processing

If the received signal is used to experimentally emulate 100 bursts from the same ONU, each having $N_{TOT} = N_{TM} + N_{DD} = 5120 \text{ bits}$, we can evaluate the local BER over T non-overlapping time slots (each of which is 256 bits long) with the same procedure as explained in Section 4.7. The resulting local BER curves versus payload time slots are shown in Figure 5.3 for the 3 different coefficient-initialization strategies (all-zeros, delta and EQ-MEM) and for different training sequence lengths N_{TM} . It is clear that, using memory-less approaches, if $N_{TM} < 2560 \text{ bits}$, the convergence to the steady-state BER value (i.e. to $BER < 10^{-3}$) has not happened yet at the end of the training phase. Indeed, during the tracking phase, the initial time slots of the payload are still spent to make the local BER decrease further (the FIR tap coefficients keep evolving). This may be critical, since a high number of errors ($BER > 10^{-3}$) at the beginning of the payload (initial time slots) may induce failures in the very first FEC blocks, which may compromise the entire packet. The particular definition of the local BER (given in Section 4.7) allows us to highlight this aspect, which was instead hidden in Figure 5.2, due to the averaging over a long payload.

On the contrary, the taps initialization approach based on memory proves once again to be able to guarantee the minimum BER since the beginning, regardless of the value of N_{TM} .

We can thus conclude that these considerations, based on experimental results, fully confirm what we found by numerical simulations in Chapter 4.

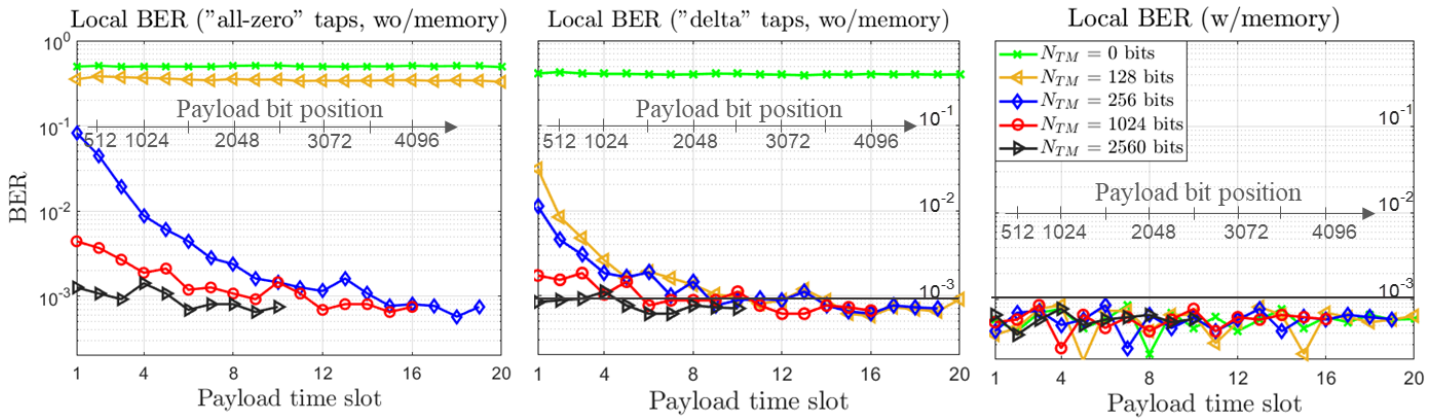


Figure 5.3. Local BER evolution for different taps initialization strategies: “all-zeros” (on the left), “delta” (in the middle) and “with memory” (on the right).

5.3 Conclusions

In this Chapter, we have experimentally demonstrated 25Gbps burst-mode US transmission in C-band using 10G-class APD and external modulation (by MZM). Despite the slightly different system setup, we were able to derive the same considerations about memory-less and memory-aided equalization strategies obtained by simulations in Chapter 4. In particular, we stressed once again that, in order to draw reliable conclusions about convergence rate, we should avoid averaging BER over a long payload. By using a properly defined Local BER, we proved that a memory-aided equalization approach can work in full-training ensuring low BER since the very beginning of the payload. This is interesting, since it enables a high data transmission efficiency. Indeed, in order to achieve the same performance, a memory-less equalization approach would require an overhead of few thousands of bits for training mode equalizer operation.

Chapter 6: Conclusions and future work

In the previous Chapters of this thesis work we've been investigating the feasibility of a cost-effective line rate increase in HS-PONs, targeting 25 Gbps and 50 Gbps per wavelength using optoelectronics originally developed for lower bitrates. Different options were analyzed in detail, featuring high spectral efficiency modulation formats (specifically, PAM-4 and duobinary signaling, in its EDB and ODB implementations) combined to bandwidth-limited transceivers, chirp-aided transmission and equalization methods. The latter were analyzed both in the downstream and upstream case, which required proper modifications related to its burst-mode peculiarity. In order to recap what we've understood until now and to what extent it could be useful for future studies and developments on the subject, we quickly review the most relevant results of our work.

The study of the impact of a realistic band-limited receiver on a PON system O-band performance, carried out in Chapter 2, provided several useful graphs (contour plots of penalty versus the receiver filtering characteristics B_{3dB} and B_{20dB} , for different modulation formats in US and DS), which could serve as guidelines for transceiver and systems designers. Also, optimistically, graphs of that kind (together with those in [2], which represented the starting point for Chapter 2) could help in making choices during the standardization process of future PON systems in FSAN and/or EFM working groups. Furthermore, the proposed three different schemes for receiver modeling could worth further research.

The extensive simulative analysis on DML/DD PON, carried out in Chapter 3, demonstrated the feasibility of 25Gbps transmission (with the help of adaptive equalization) in C-band using 25G-DML / 10G-APD and of 50Gbps transmission in O-band using 25G-DML / 25G-APD, thanks to the (pretty unintuitive) beneficial interaction between adiabatic chirp and chromatic dispersion. It was also showed that a 25Gbps transmission in C-band using 10G-DML / 10G-APD is not too far from being possible, especially when PAM-2 modulation is used and FFE is exploited at receiver. Additionally, an example of feasibility assessment was provided in the case of multiple-length systems, as typical PONs are: the derived feasible regions contour plots could be quite relevant, in view of future HS-PONs definitions. Before that, anyway, these very promising simulation results should be proven by a proper set of experiments on a commercial laser. With this purpose, the PhotoNext center at Politecnico di Torino is currently aiming at upgrading its experimental inventory with suitable bandwidth DMLs, to be used to replicate experimentally, in the near future, results similar to those shown in Chapter 3.

The main merit of Chapters 4 and 5, both dealing with burst-mode equalization strategies based on FFE and LMS algorithm, was instead the demonstration (firstly simulative, then also corroborated by experiments) that:

- a burst-mode equalization performance analysis based on average BER (and/or average MSE) over a large payload may lead to erroneous conclusions about the convergence rate of the equalization algorithm. In order to be on the safe side, carefully defined local performance metrics (fine time-resolved BER and MSE) should be adopted;
- based on the latter performance metrics, it can be shown that a memory-aided equalization approach (using memory from previous bursts of the same ONU for initializing the equalizer tap coefficients) presents several advantages compared to a memory-less one. In particular, it was proven that a memory-aided approach such as the described EQ-MEM can work in full-training (i.e. without any training bit) ensuring low BER since the very beginning of the payload, thus enabling high data transmission efficiency. On the contrary, a memory-less taps initialization strategy would require few thousands of training bits as an overhead, which would be “wasted”.

By the way, a paper on this topic including these results was submitted in October 2018 to the main Conference of the field (OFC2019).

We can eventually claim that each Chapter of this thesis still offers many open questions and job opportunities for anyone willing to work toward 25 Gbps and 50 Gbps (and beyond!) next-generation passive optical access networks.

REFERENCES

- [1] F. Effenberger, D. Cleary, O. Haran, G. Kramer., R. D. Li, M. Oron and T. Pfeiffer, “An Introduction to PON Technologies”, *IEEE Communications Magazine*, pp. S17-S25, 2007.
- [2] P. Torres-Ferrera, V. Ferrero, M. Valvo and R. Gaudino, “Impact of the Overall Electrical Filter Shaping in Next-Generation 25G and 50G PON”, *Journal of Optical Communications and Networking*, vol. 10, no. 5, 2018.
- [3] D. Nettet, “PON Roadmap”, *Journal of Optical Communications and Networking*, vol. 9, no. 1, pp. A71-A76, 2017.
- [4] Frank Effenberger, Huawei Technologies, “Convergence in Optical Access Standards”, 2018.
- [5] IEEE P802.3ca 50G-EPON Task Force , “Physical Layer Specifications and Management Parameters for 25 Gb/s and 50 Gb/s Passive Optical Networks”, [Online]. Available: <http://www.ieee802.org/3/ca/>.
- [6] V. Houtsma, D. v. Veen and E. Harstead, “Recent Progress on Standardization of Next-Generation 25, 50 and 100G EPON”, *Journal of Lightwave Technology*, vol. 35, no. 6, pp. 1228-1234, 2017.
- [7] S. Zhou, X. Liu, F. Effenberger and J. Chao, “Low-latency high-efficiency mobile fronthaul with TDM-PON (mobile-PON)”, *Journal of Optical Communications and Networking*, vol. 10, no. 1, pp. A20 - A26, 2018.
- [8] M. Caretti, P. Cinato, U. Ferrero and R. Mercinelli, “Evoluzione dell'Accesso”, *Notiziario Tecnico TIM*, pp. 140-157, Gennaio 2016.
- [9] A. Pizzinat, P. Chanclou, F. Saliou and T. Diallo, “Things You Should Know About Fronthaul”, *Journal of Lightwave Technology*, vol. 33, no. 5, pp. 1077-1083, 2015.
- [10] B. Sklar, Digital Communications, Prentice Hall, 2001.
- [11] D. T. v. Veen and V. E. Houtsma, “Proposals for Cost-Effectively Upgrading Passive Optical Networks to a 25G Line Rate”, *Journal of Lightwave Technology*, vol. 35, no. 6, pp. 1180-1187, 2017.
- [12] F. Effenberger, “PONs: State of the Art and Standardized”, in *Optical Fiber Telecommunications VIB*, Academic Press, 2013.
- [13] J. L. Wei, K. Grobe, C. Sanchez, E. Giacomidis and H. Griesser, “Comparison of cost- and energy-efficient signal modulations for next generation passive optical networks”, *Optics Express*, vol. 23, no. 22, pp. 28271-28281, 2015.
- [14] Hari Shankar, Inphi Corporation, “Duobinary modulation for optical systems”, *Lightwave Online*, 2006.
- [15] D. T. v. Veen, V. E. Houtsma, A. H. Gnauck and P. Iannone, “Demonstration of 40-Gb/s TDM-PON Over 42-km With 31 dB Optical Power Budget Using an APD-Based Receiver”, *Journal of Lightwave Technology*, vol. 33, no. 8, pp. 1675 - 1680, 2015.
- [16] V. Houtsma, D. v. Veen and E. Harstead, “PAM-4 vs. duobinary modulation @25 Gb/s”, 2014.
- [17] A. Price and N. L. Mercier, “Reduced bandwidth optical digital intensity modulation with improved chromatic dispersion tolerance”, *Electronics Letters*, vol. 31, no. 1, pp. 58 - 59, 1995.
- [18] W. Kaiser, T. Wuth, M. Wichers and W. Rosenkranz, “Reduced complexity optical duobinary 10-Gb/s transmitter setup resulting in an increased transmission distance”, *IEEE Photonics Technology Letters*, vol. 13, no. 8, pp. 884 - 886, 2001.

- [19] ITU-T G.989.2, “40-Gigabit-capable passive optical networks 2 (NG-PON2): Physical media dependent (PMD) layer specification”, 2014.
- [20] Excelitas Technologies, “Avalanche photodiode - A User Guide”, 2011.
- [21] J. G. Proakis and M. Salehi, Digital Communications (Fifth Edition), McGraw-Hill, 2008.
- [22] D. A. Ackerman et al., Agere Systems, “Telecommunication Lasers”, in *Optical Fiber Telecommunications, volume IV A*, Elsevier, 2002, pp. 613-625.
- [23] K. H. Chang, L. Grüner-Nielsen and D. W. Peckham, “Coarse Wavelength Division Multiplexing: Technologies and Applications”, in *Optical Fibers to Support CWDM*, CRC Press, 2007, pp. 19-55.
- [24] G. Agrawal, “Dispersion-induced limitations”, in *Fiber-Optic Communication Systems (Third Edition)*, Wiley, 2002, pp. 45-55.
- [25] P. R. Horche and C. d. R. Campos, “Influence of Current Pulse Shape on Directly Modulated Systems Using Positive and Negative Dispersion Fibers”, in *Selected Topics on Optical Fiber Technology*, InTech, 2012, pp. 509-532.
- [26] K. Zhang, Q. Zhuge, H. Xin, M. Morsy-Osman, E. El-fiky, L. Yi, W. Hu and D. V. Plant, “Intensity directed equalizer for the mitigation of DML chirp induced distortion in dispersion-unmanaged C-band PAM transmission”, *Optics Express*, vol. 25, no. 23, 2017.
- [27] S. H. Bae, H. Kim and Y. C. Chung, “Transmission of 51.56-Gb/s OOK signal using 1.55- μm directly modulated laser and duobinary electrical equalizer”, *Optics Express*, vol. 24, no. 20, 2016.
- [28] A. Sevian, P. Dupriez, D. Culverhouse, Corning Inc., “Negative dispersion fibers increase signal distances up to 300 km”, *Lightwave Online*, 2000.
- [29] P. J. Corvin and T. L. Koch, “Computer Simulation of High-Bit-Rate Optical Fiber Transmission Using Single-Frequency Lasers”, *Journal Of Lightwave Technology*, Vols. LT-5, no. 11, 1987.
- [30] I. Tomkos, I. Roudas, R. Hesse, N. Antoniadis, A. Boskovic and R. Vodhanel, “Extraction of laser rate equations parameters for representative simulations of metropolitan-area transmission systems and networks”, *Optics Communications*, no. 194, pp. 109-129, 2001.
- [31] C. Sun, S. H. Bae and H. Kim, “Transmission of 28-Gb/s Duobinary and PAM-4”, *IEEE Photonics Technology Letters*, vol. 29, no. 1, pp. 130-133, 2017.
- [32] S. Yin, V. Houtsma, D. v. Veen and P. Vetter, “Optical Amplified 40-Gbps Symmetrical TDM-PON Using 10-Gbps Optics and DSP”, *Journal of Lightwave Technology*, vol. 35, no. 4, 2017.
- [33] M. Nada, Y. Muramoto, H. Yokoyama, T. Ishibashi and S. Kodama, “High-sensitivity 25 Gbit/s avalanche photodiode receiver optical sub-assembly for 40 km transmission”, *Electronics Letters*, vol. 48, no. 13, 2012.
- [34] P. Ossieur, N. A. Quadir, S. Porto, C. Antony, W. Han, M. Rensing, P. O’Brien and P. D. Townsend, “A 10 Gb/s Linear Burst-Mode Receiver in 0.25 μm SiGe: C BiCMOS”, *Journal of Solid-state Circuits*, vol. 48, no. 2, pp. 381-390, 2013.
- [35] J. Man, S. Fu, H. Zhang, J. Gao, L. Zeng and X. Liu, “Downstream transmission of pre-distorted 25-Gb/s Faster-than-Nyquist PON with 10G-class optics achieving over 31 dB link budget without optical amplification”, in *Optical Fiber Communications Conference and Exhibition (OFC)*, Anaheim, CA, USA, 2016.
- [36] J. Chen, A. Tan, Z. Li, Y. Guo, Y. Yin, Q. Zhang, Y. Song, Y. Li and M. Wang, “Adaptive Equalization Enabled 25Gb/s NRZ Modulation Based on 10-G Class Optics for Upstream Burst-Mode Transmission”, in *Optical Fiber Communications Conference and Exposition (OFC)*, San Diego, CA, USA, 2018.

- [37] M. D. Santa, C. Antony, G. Talli and P. D. Townsend, “25Gb/s PAM4 Adaptive Receiver Equalisation Requirements for Burst-Mode Transmission Systems”, in *42nd European Conference on Optical Communication*, Dusseldorf, Germany, 2016.
- [38] M. D. Santa, C. Antony, M. Power, A. Jain, P. Ossieur, G. Talli and P. D. Townsend, “25Gb/s PAM4 burst-mode system for upstream transmission in passive optical networks”, in *Optical Fiber Communications Conference and Exhibition (OFC)*, Los Angeles, CA, USA, 2017.
- [39] S. Porto, C. Antony, G. Talli, D. Carey, P. Ossieur and P. Townsend, “Demonstration of 10Gb/s burst-mode transmission using a linear burst-mode receiver and burst-mode electronic equalization”, in *OFC 2014*, San Francisco, CA, USA, 2014.
- [40] V. Houtsma, D. v. Veen and E. Harstead, “Unified Evolution-Ready 25 Gbps NG-PON Architecture”, in *42nd European Conference on Optical Communication*, Dusseldorf, Germany, 2016.
- [41] D. T. v. Veen and V. E. Houtsma, “Proposals for Cost-Effectively Upgrading Passive Optical Networks to a 25G Line Rate”, *Journal of Lightwave Technology*, vol. 35, no. 6, pp. 1180-1187, 2017.
- [42] V. Ingle and J. G. Proakis, *Digital Signal Processing Using Matlab V.4*, Pws Publishing Company, 1996.
- [43] R. Koma, M. Fujiwara, J.-I. Kani, K.-I. Suzuki and A. Otaka, “Burst-mode digital signal processing that pre-calculates FIR filter coefficients for digital coherent PON upstream”, *Journal of Optical Communications and Networking*, vol. 10, no. 5, pp. 461-470, 2018.
- [44] P. Torres-Ferrera, V. Ferrero, R. Mercinelli and R. Gaudino, “Experimental demonstration of DSP-assisted Electrical Duobinary Optimization for High Speed PON 25+Gbps using 10 Gbps APD receiver”, in *ECOC*, Rome, 2018.